THE 2003 OUTBURST OF THE X-RAY TRANSIENT H1743–322: COMPARISONS WITH THE BLACK HOLE MICROQUASAR XTE J1550–564

Citation: McClintock, Jeffrey E., Ronald A. Remillard, Michael P. Rupen, M. A. P. Torres, D. Steeghs, Alan M. Levine, and Jerome A. Orosz. "THE 2003 OUTBURST OF THE X-RAY TRANSIENT H1743–322: COMPARISONS WITH THE BLACK HOLE MICROQUASAR XTE J1550–564." The Astrophysical Journal 698, no. 2 (June 1, 2009): 1398–1421. © 2009 The American Astronomical Society

As Published: http://dx.doi.org/10.1088/0004-637x/698/2/1398

Publisher: IOP Publishing

Persistent URL: http://hdl.handle.net/1721.1/96031

Version: Final published version: final published article, as it appeared in a journal, conference proceedings, or other formally published context

The Astrophysical Journal, 698:1398–1421, 2009 June 20 doi:10.1088/0004-637X/698/2/1398

THE 2003 OUTBURST OF THE X-RAY TRANSIENT H1743−322: COMPARISONS WITH THE BLACK HOLE MICROQUASAR XTE J1550−564*

Jeffrey E. McClintock[1], Ronald A. Remillard[2], Michael P. Rupen[3], M. A. P. Torres[1], D. Steeghs[1], Alan M. Levine[2], and Jerome A. Orosz[4]

[1] Harvard-Smithsonian Center for Astrophysics, 60 Garden Street, Cambridge, MA 02138, USA
[2] MIT Kavli Center for Astrophysics and Space Research, Massachusetts Institute of Technology, Cambridge, MA 02139, USA
[3] National Radio Astronomy Observatory, New Mexico Array Operations Center (VLA, VLBA), Socorro, NM 87801, USA
[4] Department of Astronomy, San Diego State University, 5500 Campanile Drive, San Diego, CA 92182, USA
Received 2007 May 1; accepted 2009 March 31; published 2009 June 1

ABSTRACT

The bright X-ray transient H1743−322 was observed daily by the *Rossi X-ray Timing Explorer* during most of its eight-month outburst in 2003. We present a detailed spectral analysis and a supporting timing analysis of all of these data, and we discuss the behavior and evolution of the source in terms of the three principal X-ray states defined by Remillard and McClintock. These X-ray results are complemented by Very Large Array data obtained at six frequencies that provide quite complete coverage of the entire outburst cycle at 4.860 GHz and 8.460 GHz. We also present photometric data and finding charts for the optical counterpart in both outburst and quiescence. We closely compare H1743−322 to the well-studied black hole X-ray transient XTE J1550−564 and find the behaviors of these systems to be very similar. As reported elsewhere, both H1743−322 and XTE J1550−564 are relativistic jet sources and exhibit a pair of high-frequency quasi-periodic oscillations with a 3:2 frequency ratio. The many striking similarities between these two sources argue strongly that H1743−322 is a black hole binary, although presently no dynamical data exist to support this conclusion.

Key words: accretion, accretion disks – binaries: close – black hole physics – stars: individual (H1743−322, XTE J1550−564) – X-rays: stars

Online-only material: color figure

1. INTRODUCTION

Twenty-two X-ray binaries contain a dynamically confirmed black hole (Remillard & McClintock 2006; Orosz et al. 2007; Silverman & Filippenko 2008). Spin estimates have been obtained for five of these black holes (Shafee et al. 2006; McClintock et al. 2006; Liu et al. 2008; Miller et al. 2008; Reis et al. 2008). These black hole binaries are important to physics as potential sites for tests of strong-field general relativity (Remillard & McClintock 2006; hereafter RM06). Seventeen of these systems are transient X-ray sources. In this paper, we discuss one such transient system, H1743−342 (hereafter H1743). The mass of its black hole primary has yet to be measured, and therefore H1743 is not a dynamically confirmed black hole binary. However, as we show in this paper, the overall behavior of this transient X-ray source and its strong similarities to the dynamically established black hole transient XTE J1550−564 make a strong case that H1743 does contain a black hole primary.

The transient H1743 displayed major outbursts in 1977, 2003, and 2008. In this paper, we present results only for the 2003 outburst cycle. The source was initially discovered with the *Ariel V* All-Sky Monitor by Kaluzienski & Holt (1977), who provided a $\sim 1^\circ$ position. Further definitive X-ray studies were carried out using the instruments aboard *HEAO 1*. The modulation collimator pinpointed the source location to one of the two equally probable X-ray positions (Doxsey et al. 1977; Gursky et al. 1978). The high-energy LED detectors observed the spectrum upward to $\approx$100 keV (Cooke et al. 1984), and the A-2 detectors (1.5–30 keV) were used to measure the medium-energy spectrum. An analysis of these latter data led White & Marshall (1984) to classify the source as a black hole candidate based on its very soft spectrum. During its 1977–1978 outburst, the source reached at least 70% of the intensity of the Crab (1–10 keV; Doxsey et al. 1977; Kaluzienski & Holt 1977), and the duration of the outburst was at least seven months (Kaluzienski & Holt 1977; Cooke et al. 1984).

The 2003 outburst was discovered by Revnivtsev et al. (2003) on March 21 using *INTEGRAL* and rediscovered a few days later by Markwardt & Swank (2003a, 2003b), who initiated the first pointed *Rossi X-ray Timing Explorer* (*RXTE*) observations of the source on March 28. Following some early confusion over the identity of the source (initially dubbed IGR/XTE J17464−3213), the X-ray transient was correctly identified with the earlier *HEAO 1* source based on its X-ray position (Markwardt & Swank 2003a, 2003b). Shortly thereafter, a radio counterpart was discovered. The precise position of the radio source agreed with the *HEAO 1* X-ray position to 8″ (Rupen et al. 2003a, 2003b), which left no doubt that the new transient and H1743 are one and the same. Shortly thereafter, a variable optical counterpart was identified, which is coincident with the radio counterpart (Steeghs et al. 2003a, 2003b; Section 3.6). The source has been closely monitored at radio wavelengths (e.g., Rupen et al. 2003a, 2003b; Section 3.5).

The discovery of a pair of high-frequency quasi-periodic oscillations (QPOs) at 240 Hz and 165 Hz is an especially important result, which was obtained using *RXTE* timing data (Homan et al. 2005; Remillard et al. 2006). Very similar pairs of high-frequency QPOs with a commensurate frequency ratio of 3:2 are seen for three other dynamical black holes: XTE J1550−564, GRO J1655−40, and GRS 1915+105 (McClintock & Remillard 2006). Thus, the presence of this distinctive harmonic pair of frequencies for H1743 opens wider the possibility of obtaining fundamental information about black holes (e.g., Abramowicz &

* This paper includes data gathered with the 6.5 m Magellan Telescopes located at Las Campanas Observatory, Chile.

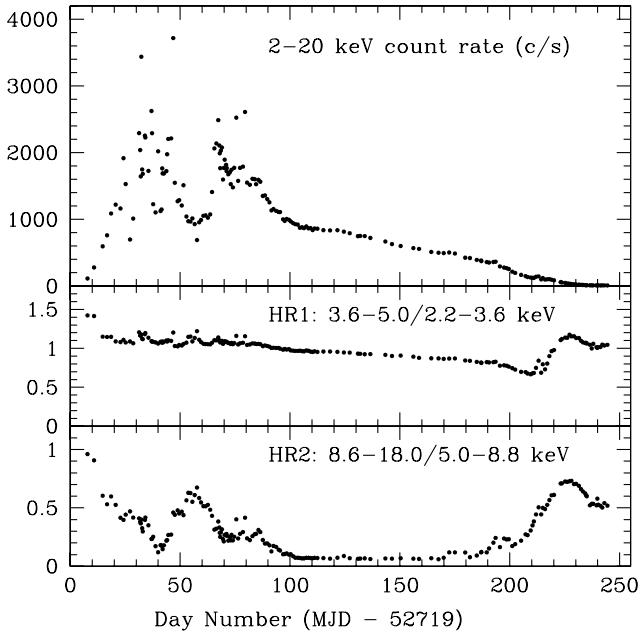

Figure 1. *RXTE* PCA count rates and hardness ratios for the energy intervals indicated. These data, from which the background rates have been subtracted (Section 2.2), were obtained using PCU-2. The Day Number is the time in days since the discovery of the outburst on 2003 March 21 (=MJD 52719).

Kluzniak 2001; Remillard et al. 2002a; Wagoner 1999). A comparably important discovery is that of the large-scale relativistic X-ray jets observed for both H1743 (Corbel et al. 2005) and XTE J1550−564 (Corbel et al. 2002). The jets are observed as plasma blobs, which were presumably ejected during the 2003 outburst of H1743 and the 1998 outburst of XTE J1550−564 (Section 4.4). The broadband spectrum for both sources is consistent with synchrotron emission from very high energy particles (∼10 TeV).

Other work on the 2003 outburst of H1743 includes a report on three high-energy *INTEGRAL* observations (Parmar et al. 2003), an investigation of the low-frequency QPOs (Homan et al. 2005), and a simultaneous *Chandra* and *RXTE* spectroscopic study (Miller et al. 2006). Several additional studies of the 2003 outburst cycle of H1743 have been published. They are not as comprehensive as the present work; however, they provide complementary and very valuable information on such topics as the high-energy spectrum, timing behavior, and accretion-disk winds. For a thorough and independent spectral/temporal analysis of the *RXTE* data obtained during the last several weeks of the outburst, with an emphasis on state transitions, see Kalemci et al. (2006). For a further analysis of state transitions for selected *INTEGRAL*/*RXTE* observations, see Joinet et al. (2005). For additional analyses of *INTEGRAL*/*RXTE* spectra made at a number of epochs, see Capitanio et al. (2005, 2006) and Lutovinov et al. (2005).

Herein, we present spectral and timing results for 170 pointed X-ray observations, as well as extensive Very Large Array (VLA) radio observations. These observations span almost eight months. Also presented are optical and near-infrared (NIR) data and images for both the outburst and quiescent states. This work is a continuation of our program to study the spectral and timing behavior of Galactic black holes. Some comparable studies of transient sources include, e.g., Ebisawa et al. (1994) on Nova Mus 1991, Sobczak et al. (1999) on GRO J1655−40, Sobczak et al. (2000b) and Remillard et al. (2002b) on XTE J1550−564, Park et al. (2004) on 4U 1543−47, Belloni et al. (2005) on GX 339-4, and Tomsick et al. (2005) on 4U 1630−47. To these we add the notable study of the persistent source Cygnus X-1 by Wilms et al. (2006).

This paper is organized as follows. In Section 2, we discuss the X-ray, radio, and optical/NIR observations and data reduction and analysis. In Section 3, we present our results for all three wave bands, while featuring the results of our X-ray spectral analysis. In Section 4, we highlight some of the more interesting behavior exhibited by H1743 while making close comparisons to the behavior of XTE J1550−564. Finally, we offer our conclusions in Section 5.

2. OBSERVATIONS, REDUCTIONS, AND ANALYSIS

In this section, we discuss the X-ray, radio, and optical/NIR data in turn. The X-ray data are described in Section 2.1, their reduction and spectral analysis is detailed in Section 2.2, and their timing analysis is briefly described in Section 2.3. We define and discuss X-ray states in Section 2.4. Our radio and optical/near-IR observations are described in Sections 2.5 and 2.6, respectively.

2.1. X-ray Observations

In Figure 1, we show the X-ray light curve of H1743 for the complete 2003 outburst cycle of the source. These are data obtained during 170 pointed *RXTE* observations using the Proportional Counter Array (PCA; Jahoda et al. 2006). The intensity and a pair of hardness ratios are plotted versus "Day Number" which is referenced to 2003 March 21 (modified Julian date 52719), the day of discovery of the outburst (Revnivtsev et al. 2003). We use the Day Number for plots and refer to it throughout this work. We also make extensive use of the "observation number," which is tabulated along with the Day Number, the modified Julian date (MJD), and the calendar date for all 170 observations (see the Appendix, Tables A1 and A2). As indicated in the figure, observations were performed on an essentially daily basis during the first 3.5 months when the source was most active, while during the next three months the source was relatively stable and observations were made only every 3–4 days. During the several weeks of hard-state activity that occurred near the end of the outburst cycle, the source was again monitored on an almost daily basis. The 170 observations include all of those obtained in our *RXTE* guest observer program (P80146) plus additional public observations of this source (P80138, P80144, P80135, and P80137).

2.2. X-ray Spectral Fitting

We fitted simultaneously the pulse-height spectra obtained using only the best-calibrated detector modules of each of the two large-area instruments on *RXTE*, i.e., Proportional Counter Unit 2 (PCU-2) of the PCA and the four detectors in Cluster A of the HEXTE. PCU-2 is a Xenon-filled detector with an effective area of ≈1250 cm^2, an energy range of 3–60 keV, and an energy resolution of ≈17% at 6 keV (Jahoda et al. 2006). The four NaI/CsI detectors of HEXTE-A provide an effective area of as much as 800 cm^2 over the energy range 15–250 keV (Rothschild et al. 1998).

The PCU-2 data were taken in the "standard 2" format, which consists of a series of 16 s accumulations of counts that were individually recorded in 129 pulse-height channels. The spectra were corrected for background and a systematic error of 1% was added in quadrature to the estimated statistical errors in the count rates. The latter allows for uncertainties in the detector response

and is generally required for successful spectral fitting of bright sources. In like manner, the standard HEXTE reduction software was used to extract the HEXTE archive mode data. The HEXTE modules were alternately pointed every 32 s at source and background positions, allowing good background subtraction. We jointly fitted each of the 170 pairs of PCA and HEXTE pulse-height spectra over the energy ranges 2.8–25 keV (PCU-2; PHA channels 4–53) and 24–200 keV (HEXTE-A; PHA channels 13–56), respectively. The energy range adopted for PCU-2 is the current standard choice used to insure reliable calibration. For HEXTE-A, using the final spectral model (see below), we tried several different low-energy limits before selecting 24 keV, which was the lowest value that allowed nearly all of the spectra to be well fitted. The upper limit of 200 keV allowed us in every case to capture all of the detected counts without significantly degrading the signal-to-noise ratio relative to a 100 keV limit.

All the spectra were analyzed using XSPEC version 11.2.0 (Arnaud 1996); the errors on both the spectral parameters (Table A1) and the fluxes (Table A2) are consistently given at the 1σ level of confidence. We experimented with many combinations of spectral components in order to arrive at a simple model that would give good fits to the maximum number of spectra. The basic model that we finally adopted is comprised of the following three components (McClintock & Remillard 2006; RM06): (1) a simple power law (POWERLAW); (2) a multitemperature blackbody accretion disk (DISKBB; Mitsuda et al. 1984; Makishima et al. 1986); and (3) a low-energy cutoff component (PHABS; Balucinska-Church & McCammon 1992; Yan et al. 1998) with the hydrogen column fixed at $N_{\rm H} = 2.2 \times 10^{22}$ cm^{-2} (see below). In addition, a Gaussian Fe–K emission-line component (GAUSSIAN) was added when its inclusion decreased the value of the reduced χ^2 by more than 0.3.[5] The central line energy and line width were allowed to float from 6.4–7.0 keV and 0.3–2.0 keV, respectively. Interestingly, none of the fits were improved by the inclusion of a smeared Fe absorption edge (e.g., Ebisawa et al. 1994), which has been widely used in similar studies (e.g., Sobczak et al. 2000b; Park et al. 2004), and this component was not used at all.

In order to achieve satisfactory fits to several dozen of the spectra that were obtained during the first half of the outburst cycle, it was necessary to allow for some curvature in the power-law component. We examined three approaches, namely (1) a simple power law plus an exponential cutoff; (2) a broken power law without an exponential cutoff; and (3) a broken power law with an exponential cutoff. Approach (2) gave globally better fit results than approach (1), but compounding the model further by adding an exponential cutoff did not improve the fits, and therefore no cutoff was used for the results reported here. In short, we substituted a broken power-law component (BKNPOWER) for the simple power-law component whenever χ^2_ν was thereby decreased by more than 0.3, which was the case for 48 of the 170 spectra.

The parameters of the broken power-law component are a pair of photon indices (Γ and $\Gamma_{\rm HI}$), a break energy ($E_{\rm break}$), and the normalization (photon flux at 1 keV), all of which were free to vary with a single constraint, $E_{\rm break} > 12.0$ keV. The photon index of the power-law component for energies above $E_{\rm break}$ was allowed to vary independently for the PCU-2 and HEXTE-A detectors, although the normalization was fitted in common. As indicated in Figure 2, the photon indices, Γ and $\Gamma_{\rm HI}$, generally tracked each other very well over the course of the observations. The high-energy photon index $\Gamma_{\rm HI}$ that we report in Section 3 and Table A1 is an inverse-variance-weighted average of the indices determined independently by the PCU-2 and HEXTE-A detectors.

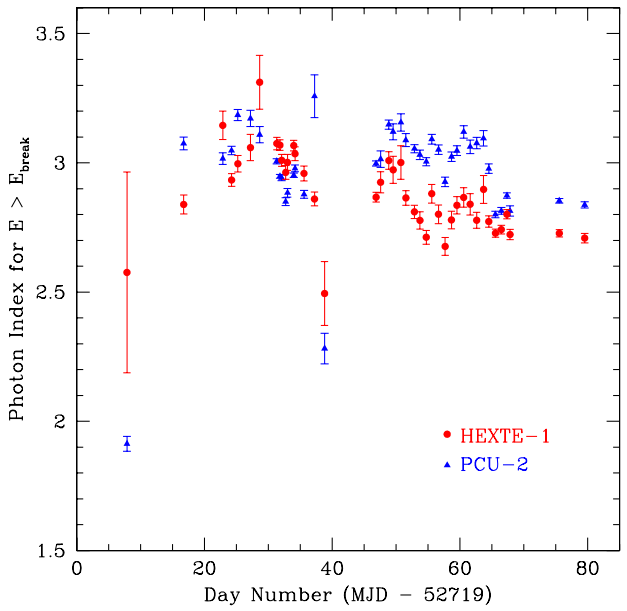

Figure 2. High-energy photon index ($E > E_{\rm break}$) was fitted independently for the PCU-2 and the HEXTE-A detectors, and the results are compared here. For each observation, an inverse-variance-weighted average of the two indices was computed to give the single photon index, $\Gamma_{\rm HI}$ (see Figure 4(d) and Table A1).
(A color version of this figure is available in the online journal.)

In earlier studies of black hole binaries, we and others have found that the normalizations of the PCA and HEXTE detectors did not agree. For example, in our spectral study of GRO J1655−40, the systematic offset between the two instruments based on observations of the Crab nebula was ∼20%, and we therefore allowed the HEXTE normalization to float independent of the PCA normalization with our reported fluxes based solely on the PCA data (Sobczak et al. 1999). In the present study, using contemporary response file, we were pleased to find that the normalizations of the two detectors were in good agreement. That is, we fitted all of the spectra using the pairs of detector response files as generated; i.e., no relative adjustment of the normalizations was made via a multiplicative constant.

In the case of 16 spectra, which were obtained at the beginning and end of the outburst cycle, plus several additional spectra near Day 55, the accretion disk component was excluded from the model because it did not improve the fit significantly; i.e., $\Delta\chi^2_\nu$ improved by < 0.3. For these spectra, the disk is either too cool to be detected by the PCA or is not present.

Table A1 lists for each spectrum the fitted values of the spectral parameters for the three model components: accretion disk (two parameters in columns 4–5), power law (either two or four parameters in columns 6–9), and Fe line (three parameters in columns 10–12). A set of blanks for a particular component indicates that this component was excluded from the fit (see above). The value of the reduced χ^2 and the number of degrees of freedom are given in column 13. As an inspection of Table A1

[5] Here and elsewhere in this paper, we use the threshold criterion $\Delta\chi^2_\nu = 0.3$, which corresponds to a change in the total χ^2 of ≈25 for 86–90 degrees of freedom (dof; Table A1, column 13). The statistical importance of including the component in question (here the Gaussian line) cannot be ascribed a definite statistical significance because our uncertainties are dominated by the 1% systematic errors in the detector response. If we ignore this problem and use the Akaike Information Criterion (Akaike 1974) to compare the model with and without the additional component, we estimate that the statistical significance of the added component (here the Gaussian line) is $\sim 4\sigma$–5σ.

shows, seven spectra (obs. no. 37, 41, 44, and 48–51) required the use of all nine parameters in order to achieve an acceptable fit. At the other extreme, two spectra (obs. nos. 165 and 168) were well fitted using only the two parameters of the simple power-law component. Remarkably, with only two exceptions, the 79 spectra corresponding to obs. nos. 58–136 were well fitted using just the four parameters that define the disk and simple power-law components; that is, these pristine spectra required no line/edge components or spectral break. Using the models considered here, as well as alternative models, we were unable to obtain satisfactory fits (i.e., $\chi^2_\nu \lesssim 2$) to three of the 170 spectra (obs. nos. 15, 21, and 127).

The value of $N_{\rm H}$ was determined in a preliminary analysis of a number of thermal-state spectra (obs. nos. 101–134) using the disk and simple power-law components indicated in Table A1 and by allowing the low-energy cutoff parameter $N_{\rm H}$ (see above) to vary. In this way, we determined an inverse-variance-weighted average value of $N_{\rm H} = 2.2 \times 10^{22}$ cm^{-2}, which we fixed in computing all of the results reported in Table A1 and elsewhere in this paper. This value is very similar to the values reported by others for this source (Doxsey et al. 1977; Parmar et al. 2003; Markwardt & Swank 2003a, 2003b; Miller et al. 2006), and it agrees with the value determined from optical/NIR observations, $N_{\rm H} = 2.1 \times 10^{22}$ cm^{-2} (Section 3.6). Furthermore, the precise value of $N_{\rm H}$ is unimportant here because for this column depth the absorption at the 2.8 keV threshold energy of the PCA is only ≈35%.

2.3. X-ray Timing Analysis

In this paper, our focus is on the analysis and presentation of the spectral data, and we do not present a full timing analysis of the data (for examples of such studies, see Remillard et al. 2002a on XTE J1550−564 and Belloni et al. 2005 on GX 339-4). The timing results reported here are intended only to supplement our featured spectral results. Our search methods for QPOs have been described previously in Remillard et al. (2002a, 2002b), and we refer the reader to these papers for background on how the power density spectrum (PDS) is computed, normalized, corrected for dead time, binned and averaged, and how our error estimates are determined. The method of detecting QPOs is likewise described in these references. Briefly, we use a sliding frequency window, which typically spans $0.2\nu_{\rm trial}$ to $5.0\nu_{\rm trial}$. Within this window, the power continuum ($P_{\rm cont}$) is modeled with a second-order polynomial in log P_ν versus log ν, since the local power continuum usually resembles a power-law function with a slight amount of curvature. The QPO profiles are presumed to be Lorentzian functions, and they are generally distinguished from broad peaks in the power continuum by a coherence parameter, $Q = \nu/{\rm FWHM} \gtrsim 2$. We use χ^2 minimization to obtain the best fit for the QPO profile and the local power continuum. When QPO detections are significant, we use the best-fit values for the Lorentzian peak and FWHM to compute the total integrated power (P) in the PDS feature; the rms amplitude of the QPO is then $a = P^{0.5}$.

All of the low-frequency QPO results reported in this paper pertain to power density spectra computed for the full bandwidth of the PCA instrument (effectively 2–40 keV) in the frequency range 4 mHz to 4 kHz. Sometimes low-frequency QPOs can appear with harmonic features, e.g., with frequencies in the ratio 1:2 and sometimes 0.5:1:2 (i.e., with a very weak subharmonic; see Remillard et al. 2002a). In such cases we force the harmonic ratios to be exact and vary only the central frequency, while allowing the widths of each feature to vary independently.

Because the timing analysis is secondary and supplementary to the spectral analysis, we average the QPO properties over the same 170 time intervals used for the spectral analyses; i.e., we do not examine in detail those few cases for which the timing properties of the source varied during the course of a single observation. Low-frequency QPOs were detected in a total of 87 of these data sets, and the QPO parameters (central frequency ν, amplitude a, and quality factor Q) are reported in Table A2. Also given in Table A2, in this case for all 170 observations, is the total rms power (r) integrated over 0.1–10 Hz (2–30 keV).

2.4. X-ray States of Black Hole Binaries

Extensive observations with *RXTE* have shown that each of the commonly identified states of black hole binaries may characterize the spectral and timing characteristics of at least some of the systems over a range of two or more decades in X-ray luminosity. Therefore, luminosity is a poor criterion to use in defining the outburst states. We thus use the state names introduced by McClintock & Remillard (2006) for the three principal states: namely, thermal dominant (TD; compared to the old state name, high soft), hard (H; compared to low hard), and steep power law (SPL; compared to very high). Note that herein and in RM06, we generally refer to the TD state as simply the thermal state. Because these revised state names are relatively unfamiliar, we list and define them in Table 1 in terms of the specific characteristics of the energy and power density spectra. The state definitions in the table are identical to those given by RM06, and as indicated in footnotes "e" and "f", they differ slightly from the original definition given by McClintock & Remillard (2006). As noted in RM06, these minor revisions resulted from gaining additional experience in analyzing long intervals of data for many black hole binaries.

The three principal outburst states defined in Table 1 represent an attempt to empirically define limited ranges of spectral and timing characteristics that often endure for prolonged periods of time and that appear to have distinct physical origins. There are gaps in the parameter ranges used to define these states, and this gives rise to intermediate or hybrid states that lie between these three principal states. In these cases, when possible we specify the admixture of the pair of principal states that describes the intermediate state in question (e.g., H:SPL).

2.5. VLA Radio Observations

We observed H1743 a total of about 50 times throughout the course of the outburst at 8.460 GHz and 4.860 GHz and about half that many times at 1.425 GHz. The radio data were reduced using the Astronomical Image Processing System (AIPS). During the first month of the outburst, about a dozen observations were made at each of three higher frequencies: 14.94 GHz, 22.46 GHz, and 43.34 GHz. All of the radio data and the corresponding VLA-antenna configurations are summarized in Tables A3–A5. The source was observed most frequently at 8.460 GHz and was reliably detected through Day 114; thereafter, our observations yielded only upper limits on the source flux density ($S_\nu \lesssim 0.3$ mJy). The peak flux density observed at 8.640 GHz was 68 mJy on Day 18.5.

2.6. Optical and Near-infrared Observations

Optical images were obtained using the MagIC CCD camera mounted on the Magellan-Clay telescope at Las Campanas Observatory. This imager provides a 2.′35 field of view sampled at 0.″069 pixel^{-1}. On 2003 April 5.4 UT (Day 15.4 of the

Table 1
Outburst States of Black Holes: Nomenclature and Definitions

New State Name (Old State Name)	Definition of X-ray State[a]
Thermal (High/Soft)	Disk fraction[b] > 75% QPOs absent or very weak: $a^c < 0.005$ Weak power continuum: $r^d < 0.075^e$
Hard (Low/Hard)	Disk fraction[b] < 20% (i.e., Power-law fraction[b] > 80% $1.4^f < \Gamma < 2.1$ Strong power continuum: $r^d > 0.1$
Steep Power Law (SPL) (Very high)	Presence of power-law component with $\Gamma > 2.4$ Power continuum: $r^d < 0.15$ Either disk fraction[b] < 80% and 0.1-30 Hz QPOs present with $a^c > 0.01$ or disk fraction[b] < 50% with no QPOs present

Notes.
[a] 2–20 keV band.
[b] Fraction of the total 2–20 keV unabsorbed flux.
[c] QPO amplitude (rms).
[d] Total rms power integrated over 0.1–10 Hz.
[e] Formerly $r < 0.06$ in McClintock & Remillard (2006).
[f] Formerly $1.5 < \Gamma$ in McClintock & Remillard (2006).

outburst), 300 s Johnson *R*- and *I*-band images were obtained under seeing conditions of 0.″48. We also secured 5 × 300 s i'-band exposures of the quiescent state on 2006 June 23.1 UT under photometric conditions and with a seeing of 0.″43. The frames were de-biased and flat-fielded and an astrometric frame in the International Celestial Reference System (ICRS) J2000.0 system was calculated using a large number of Two Micron All Sky Survey (Skrutskie et al. 2006) and UCAC2 reference stars.

Dithered K_s-band images, also of the quiescent state, were obtained during a total of 3 hr using the PANIC camera on the Magellan-Baade telescope on the nights of 2006 May 7–8 UT. Persson's Auxiliary Nasmyth Infrared Camera (PANIC; Martini et al. 2004) is an NIR camera with a pixel scale of 0.″125 pixel^{-1} that projects a 2′ field of view onto a Rockwell 1024 × 1024 HgCdTe detector. Observations consisted of a 5-point dither pattern with a 25 s exposure that was repeated three times at each dither position, yielding a total of 6.25 minutes on source. The field of H1743 is crowded, and therefore each pair of 6 minute dither sequences on the object was followed by a dithered observation of a relatively blank region of sky. These sky-blank frames were used to subtract the sky background from the target frames. We also observed the standard star S279-F (Persson et al. 1998), which we used for the absolute flux calibration. The reductions were done using PANIC/IRAF software. Seeing was typically 0.″5. In addition to these quiescent images, K_s-band images of H1743 were obtained with the PANIC camera near the end of the 2003 outburst on Day 175.1 (2003 September 12.1 UT). The same dither pattern was used with exposures of 10 s, giving 2.5 minutes on source in seeing of 0.″5.

3. RESULTS

The PCA light curve shown in Figure 1 provides a global view of the outburst. It reveals that during the first three months H1743 flared violently and exhibited a generally hard spectrum. Thereafter, the flaring subsided, and for several months the intensity of the source decayed smoothly and the spectrum was quite soft. During the final few weeks of decay, the source spectrum hardened.

We now examine the outburst in greater detail. The spectral parameters given in Table A1 and the fluxes and timing data listed in Table A2 were used in concert with the state definitions given in Table 1 to determine the state of the source during each of the 170 observations. Our state classifications are listed in the far-right column in Table A2, and they are displayed as color-coded symbols in Figure 3(a), which is a plot of the 2–20 keV model flux computed using the spectral parameters given in Table A1. The ASM light curve is shown in Figure 3(b); note the clear delineation it provides of the initial rise of the outburst.

Figure 3(a) provides a summary view of how the state of the source evolved during the course of the outburst. The source started and ended the outburst in the hard state (blue squares). Furthermore, on one other occasion during the outburst, namely Day 58, the source returned briefly to the hard state, and around this time a thermal component was not detected during five observations (Table A1). During the most intense period of flaring, the source was generally in the SPL state (green triangles), the period when high-frequency QPOs were detected (Homan et al. 2005; Remillard et al. 2006). Interestingly, in the middle of the flaring period (Days 39–43), the source entered a thermal-state lull for five days. Commencing on Day 88, the source again transitioned into the thermal state (red crosses). Thereafter it underwent a gradual and steady four-month decay before subsiding into the hard state via the H:SPL intermediate state. The occurrence of intermediate states (magenta circles), which were common during the flaring phase and again near the end of the outburst, are all hybrids of the hard and SPL states (H:SPL) with three exceptions: on Days 44, 64, and 95, the source was found in a state intermediate between the thermal and SPL states (TD:SPL; see Table A2). We note that the first observation on Day 7.8 with its hot ($kT_{in} = 1.78$ keV), tiny ($R^*_{in} = 1.2$ km) thermal component cannot be accommodated within our state classification scheme, as indicated in the last column of Table A2.

This section is organized as follows. In Section 3.1, we present and discuss a pair of figures that illustrate the principal spectral and timing data contained in Tables A1 and A2. In Section 3.2, we show representative energy spectra for several of the observations. The thermal state is the subject of Section 3.3. In Section 3.4, we examine correlative relationships between the spectral and temporal data and also discuss an impulsive power-law flare observed on Day 47. In Section 3.5, we present the radio data and discuss their connections with the X-ray data,

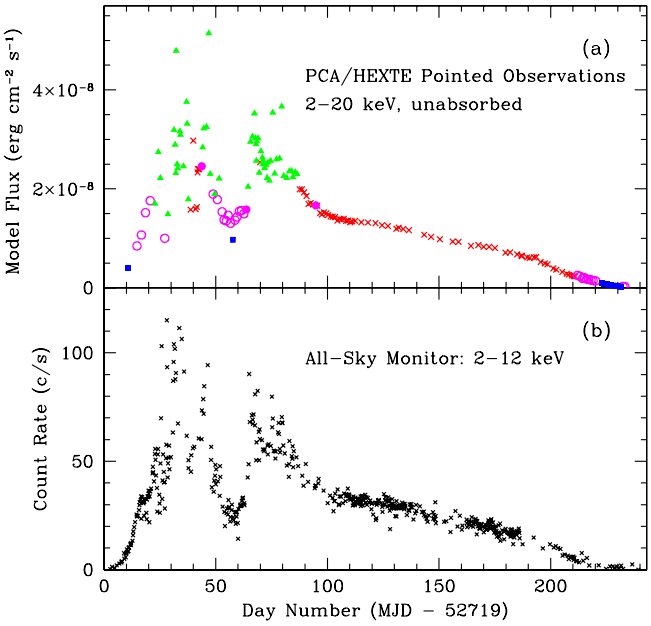

Figure 3. Evolution of H1743 during its 2003 outburst. (a) The total 2–20 keV unabsorbed model flux given in the fifth column of Table A2. The symbol type denotes the X-ray state (see the text): thermal (red cross); hard (blue square); SPL (green triangle); H:SPL intermediate state (magenta open circle); and TD:SPL intermediate state (magenta filled circle). (b) The ASM light curve; the data for individual dwells, up to several per day, are plotted.

and finally, in Section 3.6, we present the optical/NIR results for both the outburst and quiescent states.

3.1. Spectral and Temporal Evolution of the Outburst

Figure 4, which displays most of the data contained in Tables A1 and A2, offers a detailed look at the full spectral evolution of the source. Panel (a) indicates the state of the source (Section 2.4). The spectral parameters are presented in panels (b)–(d): the disk blackbody temperature (b), the inner disk radius (c), and the low- and high-energy photon indices (d). Flux data are shown in the five panels in the lower portion of the figure: the Fe–K emission-line flux (e); the disk, power law, and total fluxes in the 2–20 keV band ((f)–(h)); and the flux in the 20–100 keV band (i). The complex behavior of the source during the first few months and its stable nature thereafter is as apparent in this record as it is in the light curves shown in Figure 3.

Figure 5 presents a companion view of the outburst cycle that reveals its temporal evolution. Shown are (a) the X-ray state, (b) the rms power, r, integrated over 0.1–10 Hz in the 2–30 keV band, (c) the central frequency of the dominant QPO, (d) its amplitude, and (e) its quality factor $Q = \nu/\Delta\nu$. For comparison, the Fe–K line and disk fluxes are repeated from Figure 3 in (f) and (g), respectively. In this record, low-frequency QPOs and a strong power continuum are much in evidence throughout most of the first few months. They disappear for the next few months, while the source remains fixed in its thermal state, and they then reappear near the end of the outburst as the spectrum hardens.

The outburst cycle can be divided into three main intervals. The first of these is the initial 87 days, which is marked by strong flaring activity and a generally dominant power-law component. During the second interval, the source remained locked in the thermal state for 125 days (through Day 211) as its intensity gradually and monotonically decayed. During the last interval of 22 days, the spectrum hardened as the source made its return

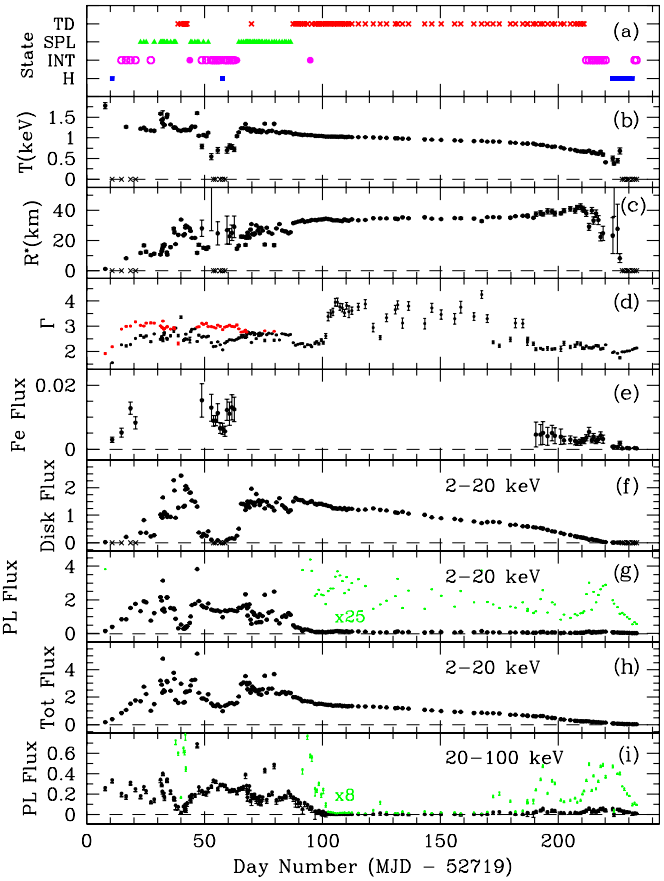

Figure 4. Spectral parameters and fluxes for 170 observations vs. Day Number. All the data presented here are contained in Tables A1 and A2. The state of the source is indicated in (a). The spectral parameters are (b) the color temperature of the accretion disk $T_{\rm in}$ in keV; (c) the inner disk radius R^* (km) $\equiv R_{\rm in}(\cos i)^{1/2}/(D/10\,{\rm kpc})$, where i is the inclination angle and D is the distance to the source in kpc; and (d) the power-law photon indices, where the black data points are for Γ ($E < E_{\rm break}$) and the red points are for $\Gamma_{\rm HI}$ ($E > E_{\rm break}$); see columns 6 and 7 in Table A1. Note the exceptional observation on Day 38.8 for which the power-law component hardens at high energies, i.e., $\Gamma > \Gamma_{\rm HI}$. The unabsorbed fluxes shown in units of 10^{-8} erg cm^{-2} s^{-1} are for (e) the Fe–K line; (f) the disk (2–20 keV); (g) the power law (2–20 keV); (h) the total (2–20 keV); and (i) the high-energy power law (20–100 keV). All the data are plotted with error bars, although they are usually too small to be apparent. In order to better display the power-law fluxes in panels (g) and (i) when they are faint, these quantities have been multiplied by the factor indicated in their respective panels and re-plotted as small, green symbols.

to the quiescent state. We now discuss these time intervals in turn in relation to Figures 4 and 5.

Flaring Period—the first 87 days: As indicated in Figure 4, during Days 8–23, the source transitioned from the hard state through an intermediate H:SPL state to the SPL state. During this period the disk flux is very low, the power-law flux rises steadily, the Fe line flux is solidly detected in four observations, there is a large difference between the two spectral indices, and QPOs are present throughout (Figure 5). Days 24–38 mark a period of intense and sustained flaring (see also Figure 3(b)). During this period the source is predominantly in the SPL state, the disk flux and temperature is high, the power-law indices become less discordant, and the Fe line is undetected; the QPO frequency is high and the amplitude is generally low. Throughout Days 39–43, the source remains in a thermal-state lull. Then, during Days 44–64, the disk flux plummets and remains low. The source initially alternates between the SPL and the hard:SPL states, later establishes itself in the SPL state and briefly visits the hard state on Day 57.7. An intense, impulsive flare is seen on

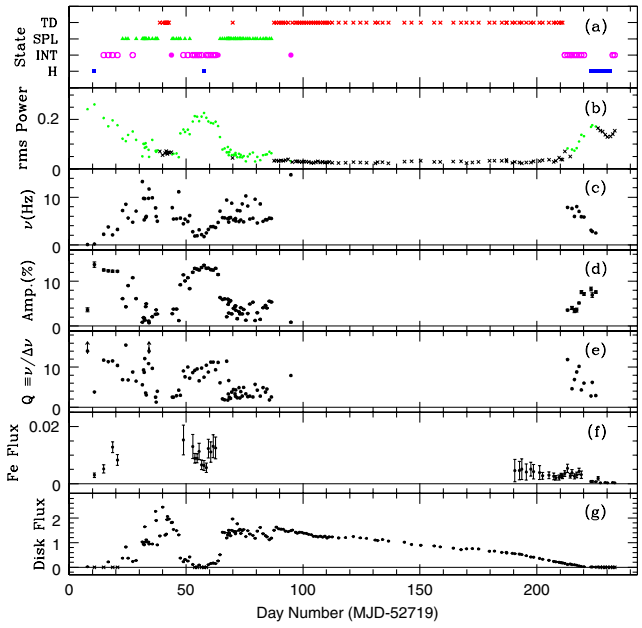

Figure 5. Timing data based on a PDS analysis plotted vs. Day Number. The state classification is shown in (a), and the 0.1–10 Hz rms continuum power in the PDS is shown in (b). For the dominant low-frequency QPO, the following three quantities are plotted: (c) central QPO frequency; (d) amplitude (% rms); and (e) quality factor Q. The gaps in these plots correspond to the nondetection of QPOs. For reference, the Fe–K line and accretion-disk fluxes are shown re-plotted from Figure 4.

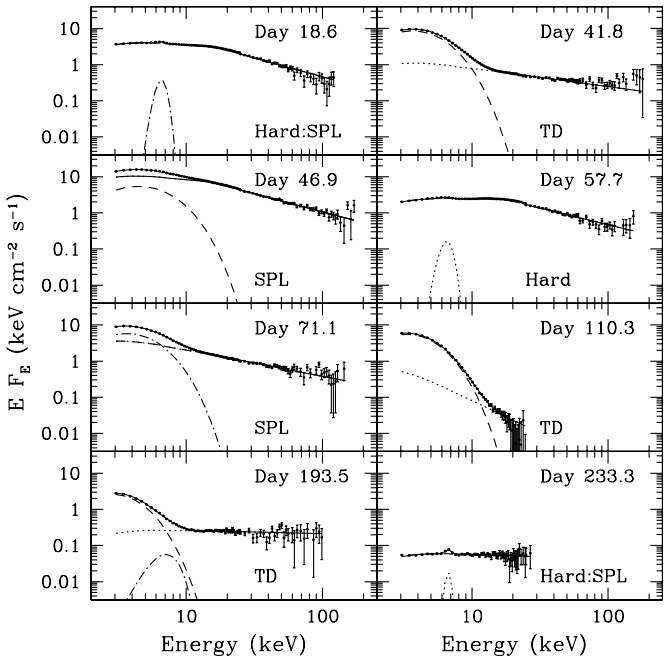

Figure 6. Sample unabsorbed and unfolded energy spectra identified by Day Number and typed by X-ray state. For each panel, the solid line, which is largely obscured by the data, is the best-fit model spectrum. The power-law, disk, and Fe line components are shown as dotted, dashed, and dot-dashed lines, respectively. Day 18.6: spectrum from the rising phase dominated by the power law; note break near 15 keV. Day 41.8: an interlude of thermal-state behavior during the flaring state. Day 46.9: spectrum of the strongest power-law flare; the power law is dominant, but note the hot ($kT = 1.60$ keV) and luminous disk component. Day 57.7: this brief excursion to the hard state during the course of an outburst cycle is unusual behavior for an X-ray transient. Day 110.3: representative spectrum obtained well into the thermal-state decay of the disk; note the faint, SPL component. Day 193.5: representative spectrum during the later stage of the thermal-state decay of the disk; note the hard, prominent power-law component during this period. Day 233.3: the final spectrum with $\Gamma = 2.14 \pm 0.02$ (Table A1) is essentially a hard-state spectrum (see footnote "g" in Table A2).

Day 46.9 during which the power-law flux triples (Figures 4(g) and (i); Section 3.4.3). The power-law flux remains high, the two photon indices diverge strongly, the Fe line is in evidence, and the QPO amplitude is high. Days 65–87 mark the second flaring phase, which is dominated by the SPL state. Three additional power-law flares are seen on Days 67.3, 75.6, and 79.5 (Figures 4(g) and (i)), the disk temperature declines, and the inner disk radius increases. QPOs of high frequency and low amplitude are present, and the power continuum plummets to a low value (Figure 5).

Thermal period—Days 88–211: With the exception of Day 94.8, the source remains in its thermal state, QPOs are absent, and the power continuum is at its rock bottom level. During the entire interval, the disk temperature falls gradually and monotonically, and the inner disk radius is fairly constant, increasing smoothly by only ≈25%. The Fe line flux is undetectable for most of this four-month period, making an appearance only during the last few weeks. The 2–20 keV power-law flux undergoes an initial rapid decay and then remains consistently low (Figure 4(g)). For an extended interval prior to Day 170, the 20–100 keV power-law flux is extremely low, contributing only an average of 0.3% of the total flux (Table A2; Figure 4(i)). Around Day 170, however, the intensity of the hard flux increases suddenly by an order of magnitude and remains at this level of intensity on average through to the end of the thermal period. Prior to Day 102, the power-law index is relatively hard: $\Gamma \approx 2.3$. However, on Day 102, the index steepens dramatically from 2.6 to 3.5 in a single day (Figure 5; Table A1). This SPL slope is maintained for about two weeks, and then a period of erratic variability sets in for almost ten weeks, during which the index varies from ≈2.3 to 3.8. In the final few weeks, the index again achieves a stable value, although it has now again become quite hard: $\Gamma \approx 2.2$.

Transition to the Hard State—Days 212–233: During the first week of this period, the source is in the H:SPL intermediate state. During this time, QPOs reappear and the power continuum climbs steadily. Shortly thereafter, the source arrives at the hard state and the power continuum reaches a local maximum of $r = 0.18$ on Day 224 (Figure 5(b)). During this same period, the QPO frequency declines steadily from an initial maximum of 7.9 Hz to a minimum of 2.5 Hz, and the amplitude increases to a maximum of 7.6% (Table A2). The power-law flux, which reemerged at the end of the thermal period, strengthens further, reaching a maximum around Day 220. During the final 10 days of this period, the source settles into the hard state and its intensity declines steadily, falling to a level of ≈7 mCrab on the final day (2–20 keV; Table A2). The QPOs shift to lower frequencies, becoming undetectable by Day 226. During the final two weeks, the Fe line flux declines and, during the final week, the disk component becomes undetectable.

3.2. Representative Energy Spectra

Eight energy spectra that illustrate the range of spectra observed for H1743 are shown in Figure 6. Initially, on Day 18.6, a strong power-law component dominates the spectrum and a significant and narrow Fe line component is present. On Day 41.8, the thermal component is ascendent for $E < 10$ keV, although a hard and intense power-law tail is also present. The SPL spectrum for Day 46.9 shows the dominant power-law component that corresponds to the intense flare observed on

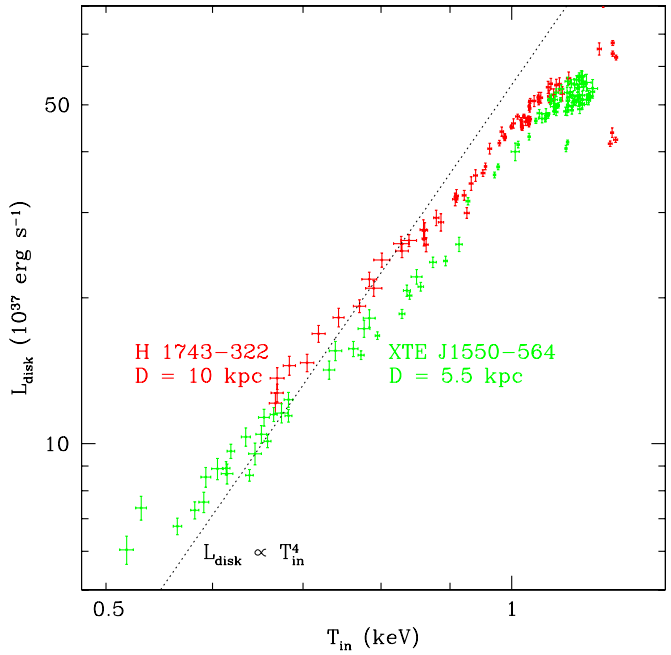

Figure 7. Bolometric luminosities vs. disk temperature for observations made in the thermal state. For H1743, the eight data points at the highest temperatures ($T_{in} \approx 1.2$ keV) were made early in the outburst cycle, near Day 42, when the flaring temporarily subsided; note that some of these thermal-state data fall well below an extrapolation of the lower-temperature data. For reference, the dotted line indicates the slope for $L_{disk} \propto T_{in}^4$.

that day (see Section 3.4.3). On Day 57.7, the disk temperature falls below the threshold for detection, and a hard-state spectrum extending to ≈170 keV is observed. The SPL spectrum observed on Day 71.1 corresponds to the second epoch of flaring activity. The thermal spectrum for Day 110.3 was obtained three weeks after the onset of the decay of the disk emission; note the faint and steep power-law component. The spectrum for Day 193.5 shows another example of thermal-state behavior that was observed late in the decay of the disk; note the similar thermal-state spectrum for Day 41.8 and the dissimilar one for Day 110.3; note also the presence of a broad Fe line component. During the last 10 days of the outburst (Day Numbers > 223), the spectrum is in the hard state. However, the final observation shown here for Day 233.3 is classified as H:SPL because the power-law index was slightly too soft ($\Gamma = 2.14 \pm 0.02$) to permit a hard-state classification (see footnote "g" in Table A2).

3.3. Thermal State: Comparison with XTE J1550−564

For many years, the thermal state of black hole X-ray binaries has been modeled successfully using a simple multitemperature accretion disk model (e.g., Shakura & Sunyaev 1973; Mitsuda et al. 1984; Makishima et al. 1986). The significant successes of this approach derive from the relative simplicity of this state for which the power-law component is weak, QPOs are absent or very weak, and the power continuum is faint (Section 2.4). An important result that illustrates the simplicity of this state is summarized in the review by Tanaka & Lewin (1995; see references therein). They show examples of the steady decay (by factors of 10–100) of the thermal flux of three sources during which R_{in} remains quite constant (see their Figure 3.14). More recently, this evidence for a constant inner radius in the thermal state has been presented for a number of sources via plots showing that the bolometric luminosity of the thermal component is approximately proportional to T_{in}^4 (Kubota et al. 2001; Kubota & Makishima 2004; Gierliński & Done 2004; Abe et al. 2005).

In Figure 7, we show such plots of the bolometric luminosity of the thermal component versus the color temperature T_{in} for the thermal-state data for H1743 and XTE J1550−564; the latter plot is based on the tabulated results in Sobczak et al. (2000b). These luminosities are averages over 4π steradians assuming that the observed thin-disk flux is $\propto \cos i$ (i.e., ignoring limb darkening), and they are based on a distance of $D = 5.5$ kpc and an inclination of $i = 70°$ for XTE J1550−564 (Orosz et al. 2002) and assumed values of $D = 10$ kpc and $i = 70°$ for H1743. (Luminosities quoted elsewhere in this paper are based solely on the observed flux.) Very similar plots for XTE J1550−564 are shown in Gierliński & Done (2004) and Kubota & Makishima (2004). For both sources, Figure 7 shows that the bolometric disk luminosity rises with temperature more slowly than T_{in}^4, or, equivalently, the color radius R_{in} decreases somewhat with increasing temperature. For example, during the four-month decay in the thermal state (Days 88–211) the radius increases by ≈25% (Figure 4(c); Table A1).

3.4. SPL, Hard, and Intermediate States

We now present results for phenomena that are absent or only weakly present in the thermal state, namely QPOs, the 0.1–10 Hz power continuum, and the power-law component. We discuss the following three topics in turn: (1) the timing data contained in Table A2; (2) for both H1743 and XTE J1550−564, we show four selected correlation plots that relate the various spectral and timing parameters; and (3) we compare the strongest of the impulsive power-law flares observed for H1743 to the unprecedented 7-Crab flare that was observed during the 1998–1999 outburst of XTE J1550−564.

3.4.1. Low-Frequency Quasi-Periodic Oscillations

QPOs were detected for 87 of the 170 observations (Figure 5; Table A2). In Table A2, in addition to presenting the central frequency, amplitude, and quality factor Q of the dominant QPO, we provide extensive footnotes describing the harmonic content, if any, of each dominant QPO, and we also note the presence of any additional QPOs. In this paper, we do not show power spectra, but illustrative examples of spectra for our comparison source XTE J1550−564 can be found in Figures 1–3 in Remillard et al. (2002b). There one will see examples of power spectra with a single dominant QPO and with harmonic components present at 0.5 and twice the central frequency, as described for H1743 in (e.g.) footnotes "h" and "j" in Table A2. One will also find in Remillard et al. an extensive discussion of phase lags, QPO types, and other properties of low-frequency QPOs, which is beyond the scope of this work.

3.4.2. Spectral/Temporal Correlations

For the 87 observations for which QPOs were detected, in Figures 8–11 we present selected correlation plots relating the QPO frequency, disk flux, 3–15 keV photon index, QPO amplitude, and continuum power density for both H1743 and XTE J1550−564. For the latter source, the spectral and QPO data were obtained from Sobczak et al. (2000b) and Remillard et al. (2002b), respectively, except for the rms continuum power data, which we computed for this work. A wider assortment of such correlation plots have been presented previously for the black hole X-ray transients XTE J1550−564 and GRO

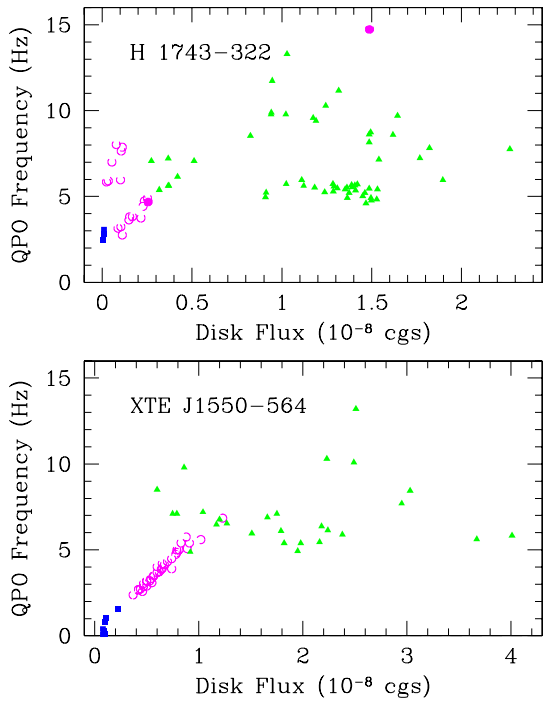

Figure 8. QPO frequency vs. disk flux for H1743 and XTE J1550−564. For the key to the plotting symbols, see Figure 3. For H1743, the strongly correlated data (see the text) were obtained in the flaring phase during the first half of the outburst; the group of seven H:SPL data points near zero disk flux and between $\nu \sim 6$–8 Hz are unrelated data obtained late in the outburst cycle (obs. nos. 152, 154–159). The error bars, which are smaller than or comparable to the size of the plotting symbols, are omitted for the sake of clarity. One extreme data point for XTE J1550−564 for MJD 51239.08 is omitted to maintain reasonable scales on the axes. The flux errors for XTE J1550−564 were overestimated by Sobczak et al. 2000b by a factor of ≈5.

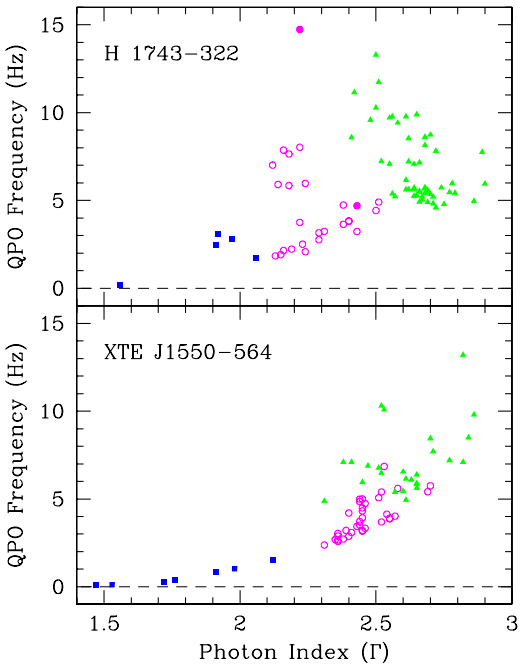

Figure 9. QPO frequency vs. the photon index Γ ($E < E_{\rm break}$). For the key to the plotting symbols, see Figure 3.

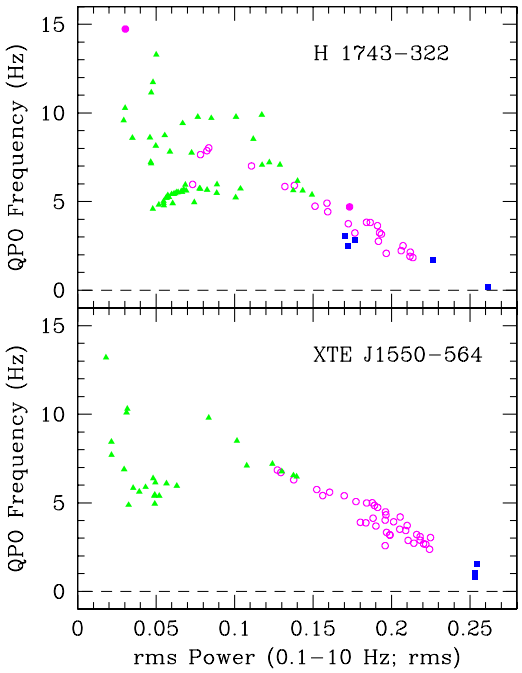

Figure 10. QPO frequency vs. the continuum power density (0.1–10 Hz). For the key to the plotting symbols, see Figure 3.

J1655−40 by Sobczak et al. (2000a) and Remillard et al. (2002b), and we refer the reader to these works for further detail. Furthermore, for the two sources in question, several additional correlation plots, including correlations that relate count rates to hardness ratios can be found in RM06 (see their Figure 7 for H1743 and their Figure 6 for XTE J1550−564).

Figure 8 shows the QPO frequency plotted versus the disk flux for H1743 and XTE J1550−564. The striking features of these plots are the very similar, tight, and approximately linear correlations that exist at relatively low values of the disk luminosity as the source transitions between the hard and SPL states via the intermediate H:SPL state. This behavior is most apparent for XTE J1550−564, where a very tight correlation exists for $\nu \lesssim 7$ Hz and disk flux $\lesssim 1.0 \times 10^{-8}$ erg cm^{-2} s^{-1}. Note that the frequency range for this correlation is about the same in the case of H1743. For both sources, one significant feature of these strongly correlated data is that the power-law flux is typically about an order of magnitude greater than the disk flux.

Figure 9 shows the QPO frequency plotted versus the photon index Γ. Figure 10 shows that the continuum power density is strongly anticorrelated with QPO frequency. Figure 11 shows a weaker anticorrelation between QPO amplitude and QPO frequency. The amplitudes are quite high at low frequencies and quite comparable for the two sources.

In all of the correlation plots shown, there are a number of quite distinct clusters of points. A detailed timing analysis would show that these groupings are associated with different types of low-frequency QPOs that can be distinguished by their coherence and their phase lag spectra. For the definitions of the various QPO types and a detailed timing analysis of the data for XTE J1550−564 that is discussed herein, see Remillard et al. (2002b).

3.4.3. Impulsive Power-Law Flares

Brief flares in the power-law flux were observed in single PCA observations on Days 32.3, 46.9, 67.3, 75.6, and 79.5 (Figures 4(g) and (i)). All of these flare events occurred in the SPL state. During the strongest of these events, which

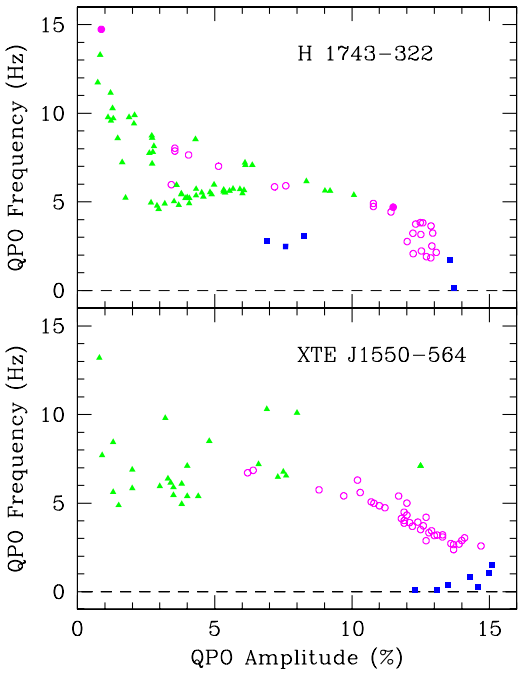

Figure 11. QPO frequency vs. QPO amplitude. For the key to the plotting symbols, see Figure 3.

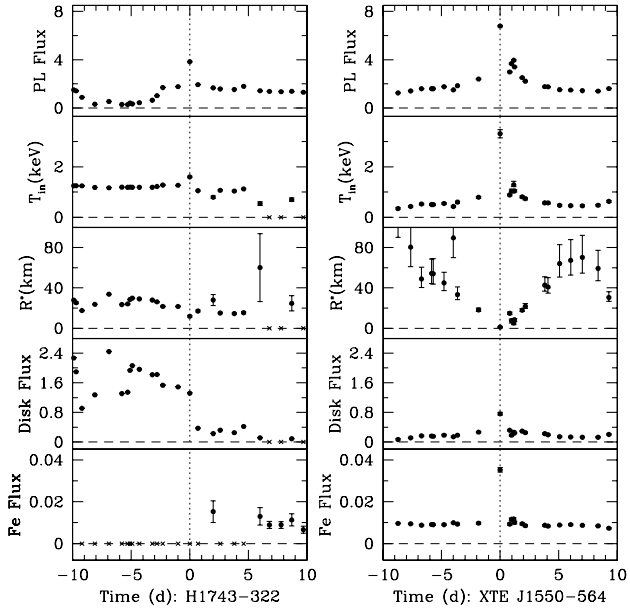

Figure 12. Detailed look at the strongest power-law flares observed for H1743 (left panel) and XTE J1550−564 (right panel). From top to bottom are plotted the power-law flux, disk temperature, inner disk radius, disk flux, and Fe–K line flux (the fluxes are in units of erg cm^{-2} s^{-1}) with the maximum of the power-law flux at time zero. To facilitate the comparison, the fluxes and radii for XTE J1550−564 have been scaled down by the factors $(5.5/10)^2$ and (5.5/10), respectively, from the values given by Sobczak et al. (2000b) to correct for the lesser distance of this source (see Section 3.3).

occurred on Day 46.9, the 2–20 keV flux increased by a factor of ≈2.5, and the 20–100 keV flux increased by a factor of ≈3 (Figures 4(g) and (i); Table A2). The increases in power-law flux are accompanied by corresponding apparent decreases in the inner disk radius (Figure 4(c)) and increases in the disk temperature (Figure 4(b)).

It is of interest to compare the giant flare observed for XTE J1550−564 on 1998 September 19–20 (Sobczak et al. 2000b) with the most intense flare observed for H1743, which occurred on Day 46.9. For both sources, the flares occurred in the SPL state (RM06). Superficially, these flares appear quite similar. For example, for both flares the power-law flux increased by the same factor of about 2.5 (Table A2; Sobczak et al. 2000b), and we note that both flares were observed only during a single, daily PCA observation.

As shown in Figure 12, in the case of XTE J1550−564 the impact of the giant flare on the spectrum of the thermal component was far greater than that observed for H1743. For example, in the former system the apparent inner radius of the disk decreased by a factor of 16 during the flare and the apparent disk temperature quadrupled, reaching $kT = 3.3$ keV. The variations in the case of H1743 are much smaller: the fitted values of the inner disk radius decreased by a factor of ≈2, and the disk temperature rose by only ≈40%. The behavior of the disk and Fe line fluxes, which are quite different for the two sources, are also compared in Figure 12.

We placed limits on the durations of these flares by examining the ASM count rate data within 10 days of the flare events. The ASM detected the giant flare of XTE J1550−564 during eight dwells, which bracket the time of the PCA observation; these data establish that the flare's duration was at least 0.87 days, but not more than 2.0 days. The H1743 flare event was not captured by the ASM, but it was recorded throughout the 3.4 ks PCA observation. We thus conclude that its duration was at least 0.04 days, but not more than 1.55 days.

3.5. VLA Radio Results: Comparisons with X-ray Data

Measurements of the radio flux densities at 1.425, 4.860, and 8.460 GHz, which span the entire outburst cycle, are shown in Figure 13(b), and the state of the X-ray source is indicated above in panel (a). Strong radio flares approaching a flux density of 100 mJy were observed during the first half of the outburst, whereas only upper limits were obtained during the second half. Observations at 14.940 GHz and two higher frequencies were made during the first 37 days of the outburst. These data, which are shown in Figure 13(c), also exhibit strong flaring behavior. The radio spectral index α is plotted in panel (d). For comparison, the 2–20 keV power-law component of the X-ray flux is shown in Figure 13(e). The radio flux density fades to ∼1 mJy on Day 80, while the X-ray source is still in the SPL state. The radio intensity further decays to the detection limit (see Table A3) by Day 117, which is ≈4 weeks after the source left the SPL state and entered the thermal state.

A closer comparison between the radio flux density (red triangles) and certain X-ray quantities (black filled circles) is displayed in Figure 14, which covers only the first 100 days of the outburst when the radio/X-ray source was most active. As usual, the state of the X-ray source is indicated in panel (a). The X-ray quantities shown are (b) the 2–20 keV power-law flux, (c) the difference between the high-energy and low-energy photon indices ($\Gamma_{\rm HI}$–Γ), and (d) the Fe–K line flux. These X-ray quantities were selected because they appear to correlate best with the behavior of the contemporaneous radio data, which are shown superimposed and arbitrarily scaled in each of the three panels (b) and (c). For clarity, only the 8.460 GHz radio data, which was the most frequently sampled band, are overplotted on the X-ray data. All of the radio data plotted in Figures 13 and 14 are given in Tables A3–A5. Further discussion of the VLA results is given in Section 4.5.

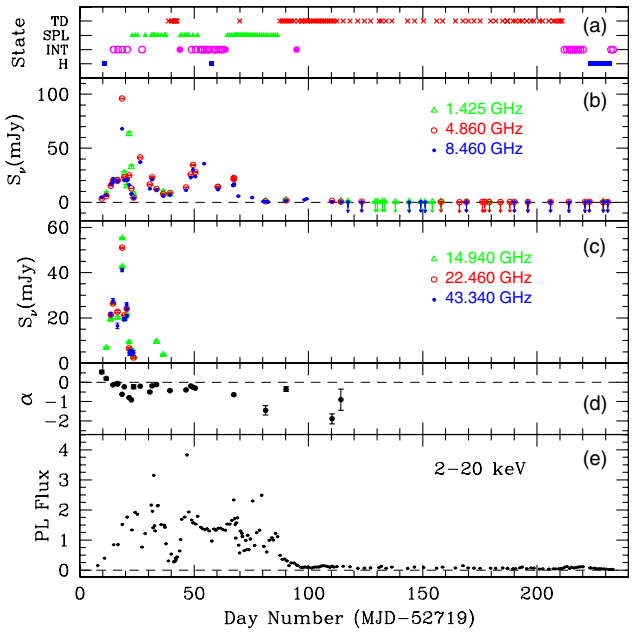

Figure 13. VLA radio data. The low-frequency data (b) extend over the entire outburst cycle (see Table A3), and the high-frequency data (c) are limited to the first 40 days (see Table A4). The radio spectral index α ($S_\nu \propto \nu^\alpha$), which is based on the 4.860 GHz and 8.460 GHz data, is shown in panel (d), and the 2–20 keV power-law flux is shown in (e) for comparison. The X-ray state is indicated in panel (a) (see Figure 3 for the key to plotting symbols).

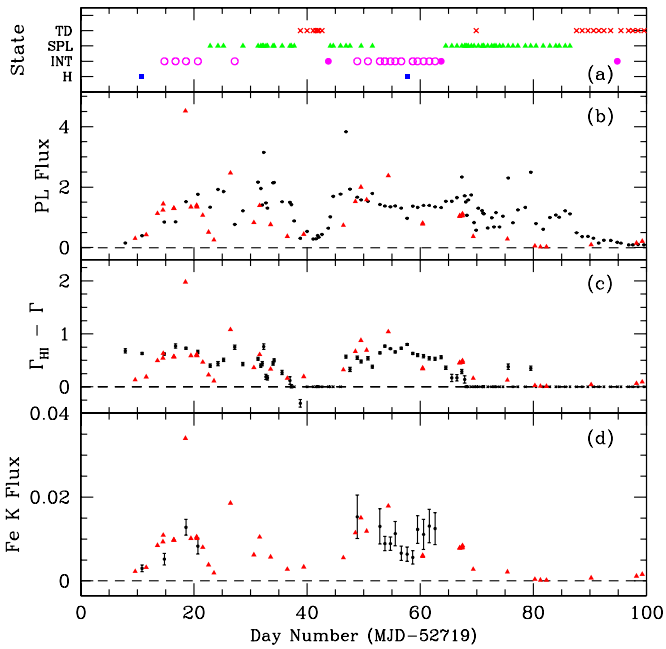

Figure 14. Superposition of radio and X-ray data are shown for the first 100 days of the outburst cycle. The same 8.460 GHz radio data are arbitrarily scaled and plotted (red triangles) in each of the three panels. The X-ray data shown are (b) the 2–20 keV power-law flux, (c) the difference in the power-law indices Γ and Γ_{HI}, and the Fe–K line flux (see Figures 4(g), (d), and (e), respectively). The X-ray state is indicated in panel (a) (see Figure 3 for the key to plotting symbols).

3.6. The Optical and Near-infrared Counterpart

In Figure 15, we compare optical observations of the field in quiescence (a) and in outburst (b). The latter observations were made early in the 2003 outburst cycle on Day 15.4 and show a counterpart consistent with the VLA radio position at a brightness level of $I = 19.3$ and $R = 21.9$ (Steeghs et al. 2003a, 2003b). These magnitudes plus the K-band magnitude of $K_s = 13.9 \pm 0.2$ obtained on the same night (Baba & Nagata 2003) suggest a reddening that is consistent with the Schlegel et al. (1998) estimate of $E_{B-V} = 3.5$ mag, which implies $N_H = 2.1 \times 10^{22}$ cm^{-2} for $A_V = 11.6$ mag (Schlegel et al. 1998; Predehl & Schmitt 1995). This is essentially the same value we obtained by analyzing the *RXTE* data: $N_H = 2.2 \times 10^{22}$ cm^{-2} (Section 2.2). Using the extinction law of Schlegel et al., this reddening estimate suggests dereddened magnitudes of $I_0 = 12.5$ and $R_0 = 12.6$ on Day 15.4 (April 5.4 UT). The position of the source in the ICRS frame is α(J2000)=17^{h}46^{m}15^s.6 and δ(J2000) = −32°14′00″.9, whose accuracy is limited by the 0″.25 rms of the astrometric solution. We were unable to detect the source in quiescence during deep i'-band exposures on 2006 June 23 (Figure 15(a)), implying a quiescent magnitude limit of $i' > 24$. This in turn implies an outburst amplitude in the optical of over 4.5 mag. At the same time, our dereddened magnitudes above, our assumed distance estimate of 10 kpc (Section 3.3), and an assumed value of $(V - R)_0 = -0.1$ imply a quite luminous counterpart with $M_V = -2.5$ (e.g., see van Paradijs & McClintock 1994).

Figure 16(a) shows the best K_S image (0″.43 seeing) that we obtained on 2006 May 7.4 UT. The location of the quiescent counterpart is consistent with the optical and radio positions (Rupen et al. 2003a, 2003b). PSF photometry (Stetson 1987) was performed to derive a quiescent magnitude of $K_s = 17.1 \pm 0.1$. The comparison K_S-band image in Figure 16(b) shows the counterpart as it appeared near the end of the outburst on Day 175.1 (2005 September 12.1 UT).

4. DISCUSSION

4.1. The Evolution of H1743 and Other X-ray Transients

The spectral and temporal evolution of H1743 (Figures 1, 3–5) is markedly similar to that observed for XTE J1550−564 in 1998–1999 (Sobczak et al. 2000b; RM06) and for GRO J1655–40 in 1996–1997 (Sobczak et al. 1999; Remillard et al. 2002b; RM06). The outburst cycles of all three sources show a double-peaked profile. During the first maximum, each source primarily exhibited strong flaring behavior and intense nonthermal emission, whereas during the second maximum the source spectrum was generally soft and thermal (RM06). H1743 deviated somewhat from this pattern because the second maximum begins in a strongly nonthermal state. Nevertheless, the outburst cycles of all three sources followed the same general sequence of events: (1) a rapid rise to maximum, (2) several months of strong flaring activity, (3) several months of slow decay in the thermal state, and (4) a final stage of rapid decay into quiescence.

An even more complex evolution was observed for the recent outburst of the recurrent X-ray transient 4U 1630−47. This source flared strongly throughout its long outburst and did not display a lengthy period of decay in the thermal state (Tomsick et al. 2005). As is well known, a significant number of other X-ray transients display simple light curves that rise rapidly, decay exponentially, and are relatively devoid of flaring behavior. These include such sources as A0620−00, Nova Mus 1991, GS2000+25, and 4U 1543−47 (Tanaka & Lewin 1995; Park et al. 2004). It has been suggested that the relative complexity of the light curves of X-ray transients may in part be caused by inclination effects (Narayan & McClintock 2005).

For a detailed discussion of physical models of the three active emission states that considers emission mechanisms, geometry, results from multiwavelength studies, etc., see Section 7 in RM06.

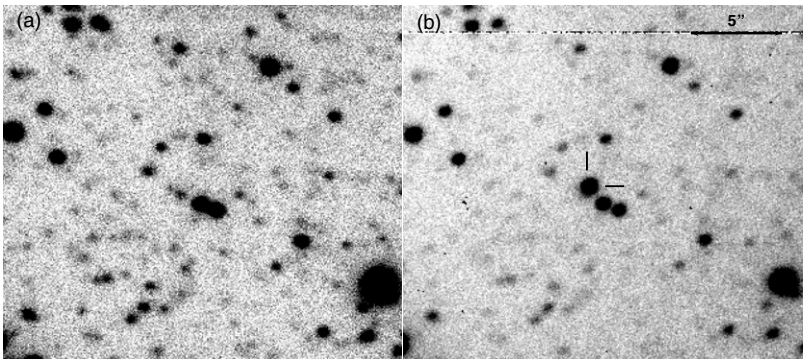

Figure 15. (a) Quiescent i'-band image obtained on 2006 June 23 UT. The image is a median of five 300 s exposures obtained under 0.″43 seeing. (b) *I*-band image obtained near the start of the 2003 outburst on Day 15.4 (2003 April 5.4 UT). Tick marks point the location of the optical counterpart. The exposure time was 330 s and the seeing was 0.″48. North is up and east is left with a 20″ field of view.

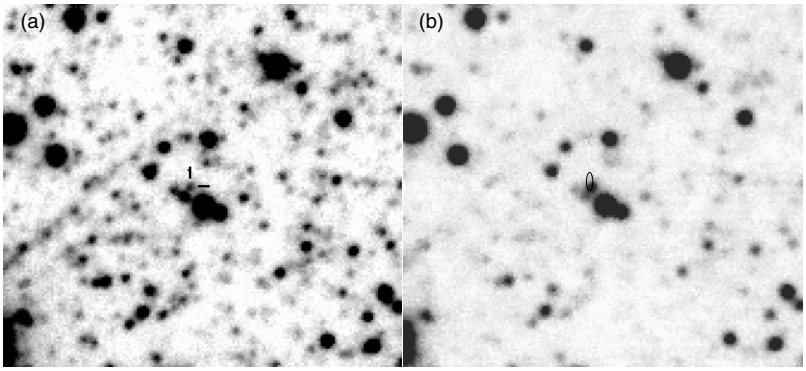

Figure 16. *K*-band images. (a) Quiescent image obtained on 2006 May 7.4 UT; the seeing was 0.″43 and the exposure time was 375 s. Tick marks indicate the location of the NIR counterpart. (b) Image obtained near the end of the outburst on Day 175.1 (2005 September 12.1 UT); the exposure time was 150 s and the seeing was 0.″55. The error ellipse marks the position of the radio counterpart to H1743; the NIR counterpart is located near the bottom of the ellipse. North is up and east is left.

4.2. The Intermediate State: Fe–K line and Spectral/Temporal Correlations

Figure 5 shows that during the first half of the outburst the H:SPL intermediate state is generally characterized by maximal values of the QPO amplitude (≈12%) and Fe line intensity. The widely accepted view is that the Fe line is fluoresced in the cold accretion disk by the hard power-law flux. It is then interesting to note that although the intensity of the power-law component is generally higher in the SPL state, particularly during the power-law flares (Section 3.4.3), than in the H:SPL state, nevertheless the Fe line is not detected in the SPL state (see Tables A1 and A2). Perhaps the higher efficiency of the intermediate state for producing the Fe line is due to a favorable geometry or is related in some way to the large amplitude of the QPOs.

At frequencies in the PDS below ≈7 Hz, H1743 and XTE J1550−564 exhibit very similar and nearly linear correlations between the QPO frequency and disk flux (Figure 8) that extend over more than a decade in both frequency and flux. Similar quasi-linear relations between these two quantities have been observed for other sources, such as for the 1–15 Hz QPOs in GRS 1915+105 (Markwardt et al. 1999; Muno et al. 1999) and the 20–30 Hz QPOs in XTE J1748−288 (Revnivtsev et al. 2000). In addition, correlations between the photon index and QPO frequency (Figure 9) have been extensively studied by Vignarca et al. (2003), Titarchuk & Fiorito (2004), and Titarchuk & Shaposhnikov (2005). The ubiquity of such correlations for black hole binaries and the striking similarities in the behaviors of H1743 and XTE J1550−564 (Figures 8–11) motivate us to examine more closely these strongly correlated data.

As stressed by Sobczak et al. (2000a) and others, the tight correlation between QPO frequency and disk flux suggests that the accretion disk regulates the frequency of the QPO oscillations and that the QPO frequency is slaved to the rate of mass accretion through the inner disk. However, as Sobczak et al. and others also stress, the QPO phenomenon is closely related to the presence of the power-law component, which must reach a threshold of ∼20% of the total (2–20 keV) flux in order to trigger the variable low-frequency QPOs. For H1743 we find a similar but higher threshold of ∼40% (Table A2). However, the power-law component is more than simply a trigger: it must also participate directly in the oscillations because when the QPO amplitude is large (∼10%–15%), the rms amplitude often exceeds the fraction of the total flux supplied by the disk alone (Table A2). Also, the energy spectrum of the QPOs is generally hard, indicating that the bulk of the flux is derived from the power-law component (Muno et al. 1999; Sobczak et al. 2000b). For the strongly correlated data, it is important to note that the power-law component is totally dominant: the power-law flux is $\gtrsim$80% of the total flux when the QPO frequency and disk flux are strongly correlated. This is true for both H1743 and XTE J1550−564. Thus, although it is the disk flux that figures in the tight correlations shown in Figure 8, nevertheless, the bulk of the total flux is supplied by the power-law component.

4.3. The Thermal State and the Inner Disk Radius

In Figure 7, the bolometric disk luminosity is seen to deviate from the simple $T_{\rm in}^4$ dependence for both XTE J1550−564 and H1743. This deviation is largely caused by spectral hardening, which is parameterized by the hardening factor $f = T_{\rm in}/T_{\rm eff}$, where $T_{\rm in}$ and $T_{\rm eff}$ are respectively the color temperature and the effective temperature (Shimura & Takahara 1995; Davis et al. 2005). The hardening factor f increases with luminosity so that

when luminosity is plotted versus $T_{\rm eff}$, one obtains a relation that is much closer to $L \propto T^4$ (Davis et al. 2006; McClintock et al. 2007).

The significance of the constancy of the inner disk radius was noted early on; for example, Tanaka & Lewin (1995) commented that the constancy of this inner radius suggests that it is related to the innermost stable circular orbit (ISCO) predicted by general relativity. This identification of the inner disk radius with the ISCO is the foundation for the measurements of black hole spin that have been obtained recently by two independent methods: fitting the spectrum of the X-ray continuum (Shafee et al. 2006; McClintock et al. 2006; Liu et al. 2008; Gou et al. 2009) and modeling the profile of the Fe–K line (Brenneman & Reynolds 2006; Miller et al. 2008; Reis et al. 2008).

4.4. Impulsive Power-Law Flares

The response of the disk parameters to intense flares has been observed for several black hole binaries (e.g., Sobczak et al. 1999, 2000b) and has been attributed to increased spectral hardening or Compton upscattering of soft disk photons; the actual physical inner-disk radius may remain fairly constant. For a thorough discussion see Sobczak et al. (2000b).

The most remarkable power-law flare observed for a black hole binary occurred early in the outburst cycle of XTE J1550−564. The flare reached a peak intensity of 6.8 Crab (2–10 keV) on 1998 September 19–20 (Sobczak et al. 2000b). Soon after this strong flare, superluminal radio jets ($>2c$) were reported (Hannikainen et al. 2001). A few years later, large-scale ($\sim 20''$) radio and X-ray jets were discovered, which were most likely ejected during the 1998 September event (Corbel et al. 2002; Tomsick et al. 2003; Kaaret et al. 2003). More recently, a similar pair of large-scale, X-ray jets has been observed for H1743 (Corbel et al. 2005). By analogy with the behavior of XTE J1550−564, it is reasonable to suppose that these jets are connected with the impulsive flare events described in Section 3.4.2.

4.5. Radio/X-ray Connections

It is unreasonable to expect a point-by-point correlation between the X-ray and radio data shown in Figure 13 because the higher time resolution ASM light curve (Figure 3(b)) shows strong X-ray variability on a timescale as short as minutes, and the X-ray and radio observations were typically separated by $\gtrsim$hours (compare Tables A2 and A3). For example, for the tripling of the radio intensity that occurred on Day 18.5 (Figure 15; Table A3), the proximate X-ray observation did not commence for over 2 hr (Table A2). Similarly, the radio observation nearest the intense power-law X-ray flare that occurred on Day 46.9 (Table A2) occurred 10.7 hr earlier. Similarly, given the sparseness and asynchronous quality of the X-ray/radio data, it is not possible to make useful comments on the relationship between radio flaring and state transitions (e.g., see Fender et al. 2004).

Despite the limitations of the data, all three of the X-ray quantities shown in Figures 14(b)–(d) do appear to be generally correlated with the radio data. Arguably it is the break in the power-law spectrum at ∼15 keV ($\Gamma_{\rm HI}$–Γ) that best correlates with the radio data.

5. CONCLUSIONS

We have performed a spectral and timing analysis of 170 *RXTE* observations that cover the complete 2003 outburst cycle of H1743−322. The PCA and HEXTE spectra, which were fitted simultaneously, were decomposed into disk-blackbody and power-law components. For about a quarter of the spectra, a much better fit was achieved when a break in the spectral index was included in the power-law component. Likewise, a Gaussian Fe–K emission-line component was included whenever it improved the fit significantly. No thermal emission was detected in 16 spectra, and the disk blackbody component was not used in fitting these spectra. The model gave good fits to all but three of the 170 spectra. Power density spectra were computed and the level of the power continuum was determined for all 170 observations. QPOs in the range 1–15 Hz were detected for 87 of the data sets, and the frequency, intensity, and quality factor Q of the dominant QPO were obtained. All of the products of these spectral and timing analyses are contained in Tables A1 and A2, and most of the results are summarized in Figures 4 and 5, which present a detailed look at the spectral and temporal evolution of the 2003 outburst.

Using the results contained in Tables A1 and A2, we classified the state of the source according to the criteria summarized in Table 1 (McClintock & Remillard 2006; RM06), which are based on the power-law spectral index, the relative strengths of the power-law and disk components, the presence or absence of QPOs, and the strength of the power density continuum. These state classifications, which are a key ingredient of this work, are displayed in Figures 3–5, 8–11, and 13–14, listed in Table A2, and referred to throughout the text.

The X-ray properties of H1743 and XTE J1550−564 are very similar, including the general character of their X-ray light curves, the occasional appearance of impulsive power-law flares (Figure 12), and their long and slow decline in the thermal state (Figures 3 and 4), during which their disk luminosities are approximately $\propto T_{\rm in}^4$ (Figure 7). Additional notable similarities are the nearly identical and tight correlations that exist between the low-luminosity disk flux, the QPO frequency, and the 0.1–1 Hz continuum power. These results, which are displayed in Figures 8–11, illustrate that the transition between the hard and SPL states can be remarkably orderly and stereotypical. As shown in Figure 5, the intermediate H:SPL state is distinguished by its strong QPOs and by its high efficiency for producing Fe line flux.

We present VLA data at six frequencies that extend throughout the entire outburst cycle at 4.860 GHz and 8.460 GHz. The radio source was observed to be active only during the first ≈100 days (Figure 13). Finally, we present optical/NIR data and finding charts (Figures 15 and 16) for the optical counterpart in both outburst and quiescence.

This work was supported in part by NASA grants NNG05GB31G and NNX08AJ55G. M.A.P.T. was supported by NASA LTSA grant NAG-5-10889, and D.S. acknowledges the support of a Smithsonian Astrophysical Observatory Clay fellowship. We thank Jean Swank and her staff for support and for the execution of the *RXTE* observations, David Kaplan for obtaining the 2003 Magellan/MagIC images, Jack Steiner for advice on statistics, and the anonymous referee whose criticisms were quite helpful.

APPENDIX

RESULTS OF X-RAY AND RADIO ANALYSES IN TABULAR FORM

Tables A1 and A2 contain all of the X-ray spectral parameters and fluxes that are displayed in Figures 4 and 5 for the 170

Table A1
Spectral Parameters for H1743−322

Obs. No.	Day[a]	MJD[b]	$T_{\rm in}$ (keV)	$R_{\rm in}^{*}$[c] (km)	Γ[d]	$\Gamma_{\rm HI}$[e]	$E_{\rm break}$ (keV)	Power-law Norm.[f]	$E_{\rm line}$[g] (keV)	FWHM[g] (keV)	Line Flux[g]	χ_{ν}^{2}/dof[h]
(1)	(2)	(3)	(4)	(5)	(6)	(7)	(8)	(9)	(10)	(11)	(12)	(13)
1	7.8	52726.850	1.776 ± 0.073	1.21 ± 0.07	1.24 ± 0.03	1.92 ± 0.03	22.7 ± 0.6	0.09 ± 0.01	···	···	···	1.65/87
2	10.8	52729.809	···	···	1.56 ± 0.01	2.19 ± 0.02	16.6 ± 0.4	0.46 ± 0.01	6.4 ± 0.2	0.5 ± 0.2	0.30 ± 0.08	1.70/86[i]
3	14.8	52733.762	···	···	2.27 ± 0.01	2.89 ± 0.02	17.1 ± 0.4	3.72 ± 0.04	6.5 ± 0.2	0.5 ± 0.2	0.52 ± 0.14	1.08/86
4	16.7	52735.734	1.265 ± 0.021	8.30 ± 0.44	2.23 ± 0.04	3.00 ± 0.02	15.1 ± 0.3	3.52 ± 0.32	···	···	···	0.93/87
5	18.6	52737.580	···	···	2.28 ± 0.01	3.01 ± 0.02	15.7 ± 0.2	6.82 ± 0.07	6.5 ± 0.1	0.5 ± 0.1	1.28 ± 0.19	0.91/86
6	20.7	52739.678	···	···	2.52 ± 0.02	3.18 ± 0.02	16.3 ± 0.3	11.77 ± 0.12	6.4 ± 0.2	0.3 ± 0.2	0.83 ± 0.19	0.82/86
7	22.8	52741.854	1.221 ± 0.015	11.81 ± 0.61	2.64 ± 0.03	3.04 ± 0.02	16.2 ± 0.5	10.79 ± 0.75	···	···	···	0.91/87
8	24.2	52743.240	1.248 ± 0.013	16.77 ± 0.86	2.57 ± 0.04	3.01 ± 0.01	13.7 ± 0.4	13.97 ± 1.43	···	···	···	1.04/87
9	25.2	52744.220	1.191 ± 0.021	12.52 ± 0.92	2.62 ± 0.03	3.13 ± 0.02	15.0 ± 0.4	14.57 ± 1.07	···	···	···	1.15/87
10	27.2	52746.195	1.177 ± 0.017	10.30 ± 0.45	2.39 ± 0.03	3.14 ± 0.03	15.3 ± 0.3	4.15 ± 0.36	···	···	···	1.08/87
11	28.6	52747.633	1.171 ± 0.018	11.26 ± 0.56	2.70 ± 0.02	3.13 ± 0.03	18.1 ± 0.6	10.8 ± 0.60	···	···	···	0.99/87
12	31.3	52750.313	1.583 ± 0.020	10.73 ± 0.53	2.49 ± 0.03	3.02 ± 0.01	14.9 ± 0.3	13.81 ± 1.10	···	···	···	0.89/87
13	31.8	52750.810	1.433 ± 0.014	12.91 ± 0.58	2.59 ± 0.03	2.96 ± 0.01	14.8 ± 0.3	14.63 ± 1.19	···	···	···	0.81/87
14	32.1	52751.089	1.360 ± 0.011	14.37 ± 0.56	2.51 ± 0.04	2.95 ± 0.01	14.1 ± 0.3	9.31 ± 1.02	···	···	···	0.86/87
15	32.3	52751.316	1.452 ± 0.206	16.56 ± 0.99	2.45 ± 0.05	3.21 ± 0.01	13.0 ± 0.3	19.02 ± 2.13	···	···	···	2.81/83[j]
16	32.7	52751.714	1.321 ± 0.012	16.31 ± 0.69	2.69 ± 0.05	2.88 ± 0.01	13.4 ± 0.7	12.92 ± 1.44	···	···	···	0.82/87
17	33.0	52751.987	1.311 ± 0.009	17.30 ± 0.58	2.74 ± 0.04	2.91 ± 0.01	13.9 ± 0.7	12.33 ± 1.37	···	···	···	0.73/87
18	34.0	52752.972	1.503 ± 0.017	12.05 ± 0.59	2.53 ± 0.03	2.97 ± 0.01	14.7 ± 0.3	14.59 ± 1.21	···	···	···	0.72/87
19	34.2	52753.167	1.563 ± 0.023	10.59 ± 0.61	2.49 ± 0.03	2.99 ± 0.01	14.5 ± 0.3	13.72 ± 1.14	···	···	···	0.83/87
20	35.6	52754.575	1.321 ± 0.011	15.65 ± 0.63	2.62 ± 0.04	2.89 ± 0.01	14.1 ± 0.5	11.89 ± 1.23	···	···	···	0.88/87
21	37.0	52755.960	1.247 ± 0.007	27.86 ± 0.81	2.83 ± 0.07	2.95 ± 0.02	12.0 ± 2.2	16.18 ± 2.83	···	···	···	3.38/87
22	37.2	52756.219	1.251 ± 0.008	25.28 ± 0.82	2.89 ± 0.01	2.98 ± 0.03	12.0 ± 4.6	16.79 ± 2.74	···	···	···	1.67/87
23	37.7	52756.714	1.248 ± 0.005	17.60 ± 0.25	2.93 ± 0.02	···	···	11.03 ± 0.62	···	···	···	0.62/90
24	38.8	52757.803	1.183 ± 0.004	23.70 ± 0.18	2.63 ± 0.05	2.32 ± 0.05	18.5 ± 2.3	2.44 ± 0.31	···	···	···	0.85/87
25	40.0	52758.996	1.169 ± 0.002	33.77 ± 0.26	3.36 ± 0.05	···	···	12.16 ± 1.51	···	···	···	1.34/90
26	41.1	52760.081	1.194 ± 0.004	23.48 ± 0.18	2.44 ± 0.03	···	···	1.66 ± 0.12	···	···	···	1.02/90
27	41.6	52760.558	1.187 ± 0.003	24.16 ± 0.19	2.47 ± 0.03	···	···	1.77 ± 0.13	···	···	···	1.22/90
28	41.8	52760.854	1.195 ± 0.003	28.50 ± 0.19	2.51 ± 0.01	···	···	2.62 ± 0.10	···	···	···	1.13/90
29	42.0	52761.039	1.188 ± 0.003	29.85 ± 0.20	2.69 ± 0.03	···	···	2.95 ± 0.25	···	···	···	1.10/90
30	42.6	52761.612	1.188 ± 0.003	29.10 ± 0.21	2.49 ± 0.02	···	···	2.77 ± 0.14	···	···	···	1.00/90
31	43.7	52762.746	1.189 ± 0.003	27.96 ± 0.23	2.46 ± 0.11	···	···	3.87 ± 0.13	···	···	···	0.82/90
32	44.1	52763.095	1.222 ± 0.004	26.21 ± 0.24	2.79 ± 0.02	···	···	10.37 ± 0.47	···	···	···	1.18/90
33	44.6	52763.617	1.275 ± 0.005	21.71 ± 0.29	2.88 ± 0.02	···	···	19.71 ± 0.85	···	···	···	0.86/90
34	45.9	52764.907	1.269 ± 0.005	21.63 ± 0.27	2.90 ± 0.01	···	···	21.18 ± 0.65	···	···	···	1.45/90
35	46.9	52765.867	1.598 ± 0.028	11.88 ± 0.82	2.40 ± 0.03	2.97 ± 0.01	14.5 ± 0.3	21.12 ± 1.69	···	···	···	0.80/87
36	47.6	52766.575	1.052 ± 0.023	17.08 ± 0.97	2.65 ± 0.03	2.98 ± 0.03	15.7 ± 0.7	15.88 ± 1.01	···	···	···	1.20/87
37	48.9	52767.865	0.793 ± 0.051	27.96 ± 5.39	2.57 ± 0.02	3.12 ± 0.02	16.4 ± 0.4	12.07 ± 0.53	6.4 ± 0.4	0.7 ± 0.2	1.53 ± 0.52	0.64/84
38	49.5	52768.547	1.070 ± 0.022	15.16 ± 0.81	2.60 ± 0.02	3.08 ± 0.03	16.2 ± 0.6	11.98 ± 0.75	···	···	···	0.81/87
39	50.7	52769.746	1.039 ± 0.027	14.53 ± 0.89	2.58 ± 0.02	3.12 ± 0.03	17.3 ± 0.6	11.25 ± 0.59	···	···	···	1.12/87
40	51.5	52770.535	1.123 ± 0.018	15.44 ± 0.86	2.61 ± 0.03	2.99 ± 0.02	14.8 ± 0.6	13.82 ± 1.03	···	···	···	1.07/87
41	52.9	52771.868	0.543 ± 0.076	60.20 ± 33.69	2.35 ± 0.02	2.99 ± 0.01	15.8 ± 0.3	7.20 ± 0.27	6.4 ± 0.5	0.7 ± 0.2	1.30 ± 0.42	0.83/84
42	53.7	52772.739	···	···	2.20 ± 0.01	2.97 ± 0.02	16.8 ± 0.2	5.36 ± 0.06	6.5 ± 0.1	0.5 ± 0.2	0.89 ± 0.17	1.29/86
43	54.7	52773.725	···	···	2.21 ± 0.01	2.93 ± 0.01	16.1 ± 0.2	5.37 ± 0.06	6.6 ± 0.1	0.5 ± 0.2	0.89 ± 0.16	1.71/86
44	55.6	52774.582	0.700 ± 0.067	24.70 ± 7.58	2.39 ± 0.01	3.05 ± 0.02	16.9 ± 0.3	7.43 ± 0.27	6.4 ± 0.3	0.6 ± 0.2	1.13 ± 0.29	0.98/84
45	56.6	52775.634	···	···	2.27 ± 0.01	3.00 ± 0.02	17.2 ± 0.3	5.74 ± 0.06	6.4 ± 0.2	0.4 ± 0.2	0.66 ± 0.17	1.26/86
46	57.7	52776.684	···	···	2.07 ± 0.01	2.87 ± 0.02	16.8 ± 0.2	3.00 ± 0.03	6.4 ± 0.3	0.6 ± 0.2	0.64 ± 0.17	1.22/86
47	58.7	52777.667	···	···	2.34 ± 0.01	2.97 ± 0.02	16.9 ± 0.3	6.78 ± 0.07	6.5 ± 0.1	0.2 ± 0.3	0.56 ± 0.16	1.21/86
48	59.5	52778.526	0.700 ± 0.075	26.82 ± 9.38	2.40 ± 0.02	3.00 ± 0.02	16.6 ± 0.4	7.28 ± 0.29	6.4 ± 0.3	0.7 ± 0.2	1.23 ± 0.33	1.06/84
49	60.6	52779.584	0.796 ± 0.061	22.71 ± 5.15	2.47 ± 0.02	3.05 ± 0.02	16.5 ± 0.4	8.59 ± 0.36	6.4 ± 0.4	0.6 ± 0.2	1.11 ± 0.36	0.87/84
50	61.6	52780.598	0.781 ± 0.052	25.10 ± 5.05	2.46 ± 0.02	3.00 ± 0.02	16.3 ± 0.5	8.45 ± 0.40	6.4 ± 0.4	0.7 ± 0.2	1.31 ± 0.40	0.85/84
51	62.6	52781.616	0.725 ± 0.054	29.01 ± 7.17	2.45 ± 0.02	2.98 ± 0.02	16.3 ± 0.4	8.04 ± 0.33	6.4 ± 0.4	0.7 ± 0.2	1.25 ± 0.38	0.81/84
52	63.7	52782.697	1.041 ± 0.024	14.58 ± 0.74	2.49 ± 0.02	3.05 ± 0.03	17.1 ± 0.5	8.43 ± 0.44	···	···	···	1.18/87
53	64.5	52783.510	1.134 ± 0.014	16.65 ± 0.66	2.54 ± 0.03	2.90 ± 0.01	14.6 ± 0.6	10.58 ± 0.85	···	···	···	1.07/87
54	65.6	52784.568	1.234 ± 0.010	22.60 ± 0.93	2.60 ± 0.07	2.77 ± 0.01	12.0 ± 2.3	11.66 ± 1.92	···	···	···	1.23/87
55	66.5	52785.483	1.234 ± 0.009	22.49 ± 0.81	2.62 ± 0.06	2.79 ± 0.01	12.7 ± 1.1	12.98 ± 1.79	···	···	···	1.02/87
56	67.3	52786.350	1.336 ± 0.013	17.12 ± 0.80	2.56 ± 0.04	2.85 ± 0.01	13.9 ± 0.6	16.66 ± 1.67	···	···	···	0.78/87
57	67.8	52786.846	1.229 ± 0.012	21.91 ± 1.10	2.63 ± 0.07	2.77 ± 0.01	12.0 ± 3.2	13.68 ± 2.20	···	···	···	0.86/87
58	68.0	52787.044	1.220 ± 0.006	23.00 ± 0.32	2.76 ± 0.06	···	···	14.69 ± 0.63	···	···	···	1.16/90
59	68.2	52787.237	1.193 ± 0.005	25.19 ± 0.28	2.73 ± 0.02	···	···	9.91 ± 0.50	···	···	···	0.89/90
60	68.5	52787.492	1.217 ± 0.005	23.10 ± 0.28	2.77 ± 0.01	···	···	15.55 ± 0.32	···	···	···	1.85/90
61	69.0	52788.025	1.225 ± 0.007	21.88 ± 0.33	2.72 ± 0.01	···	···	15.90 ± 0.58	···	···	···	0.96/90

Table A1
(Continued)

Obs. No.	Day[a]	MJD[b]	$T_{\rm in}$ (keV)	$R_{\rm in}^{*}$ [c] (km)	Γ[d]	$\Gamma_{\rm HI}$[e]	$E_{\rm break}$ (keV)	Power-law Norm.[f]	$E_{\rm line}$[g] (keV)	FWHM[g] (keV)	Line Flux[g]	χ_ν^2/dof[h]
(1)	(2)	(3)	(4)	(5)	(6)	(7)	(8)	(9)	(10)	(11)	(12)	(13)
62	69.5	52788.506	1.155 ± 0.004	27.22 ± 0.26	2.70 ± 0.01	···	···	7.35 ± 0.25	···	···	···	0.91/90
63	69.9	52788.878	1.161 ± 0.004	30.81 ± 0.27	2.36 ± 0.02	···	···	2.94 ± 0.14	···	···	···	0.89/90
64	70.3	52789.264	1.205 ± 0.005	24.29 ± 0.28	2.76 ± 0.01	···	···	12.66 ± 0.45	···	···	···	1.09/90
65	70.9	52789.930	1.203 ± 0.005	23.95 ± 0.29	2.73 ± 0.02	···	···	11.34 ± 0.50	···	···	···	1.08/90
66	71.1	52790.129	1.191 ± 0.006	24.11 ± 0.39	2.68 ± 0.04	···	···	9.74 ± 1.04	···	···	···	0.78/90
67	71.2	52790.236	1.194 ± 0.005	24.73 ± 0.27	2.73 ± 0.01	···	···	10.36 ± 0.37	···	···	···	1.02/90
68	71.9	52790.916	1.149 ± 0.004	29.99 ± 0.28	2.51 ± 0.02	···	···	4.26 ± 0.22	···	···	···	0.78/90
69	72.6	52791.632	1.167 ± 0.004	26.55 ± 0.27	2.70 ± 0.01	···	···	8.76 ± 0.29	···	···	···	1.09/90
70	73.0	52792.036	1.143 ± 0.004	28.35 ± 0.28	2.63 ± 0.02	···	···	5.42 ± 0.29	···	···	···	0.85/90
71	73.4	52792.390	1.181 ± 0.005	24.72 ± 0.28	2.74 ± 0.01	···	···	10.90 ± 0.34	···	···	···	1.27/90
72	74.0	52793.024	1.134 ± 0.004	28.39 ± 0.28	2.65 ± 0.02	···	···	5.59 ± 0.31	···	···	···	1.22/90
73	74.6	52793.607	1.173 ± 0.005	26.51 ± 0.28	2.71 ± 0.01	···	···	9.35 ± 0.36	···	···	···	1.04/90
74	75.6	52794.559	1.341 ± 0.014	17.36 ± 0.89	2.44 ± 0.05	2.82 ± 0.01	13.0 ± 0.4	13.57 ± 1.62	···	···	···	0.84/87
75	76.4	52795.381	1.134 ± 0.004	28.39 ± 0.29	2.67 ± 0.02	···	···	6.95 ± 0.28	···	···	···	0.98/90
76	77.3	52796.265	1.164 ± 0.005	25.41 ± 0.31	2.73 ± 0.01	···	···	11.57 ± 0.31	···	···	···	1.45/90
77	78.6	52797.583	1.171 ± 0.006	24.45 ± 0.31	2.71 ± 0.01	···	···	11.95 ± 0.33	···	···	···	1.37/90
78	79.5	52798.535	1.339 ± 0.014	16.92 ± 0.84	2.45 ± 0.04	2.80 ± 0.01	13.7 ± 0.5	14.89 ± 1.58	···	···	···	0.81/89
79	80.5	52799.455	1.138 ± 0.004	27.97 ± 0.29	2.66 ± 0.02	···	···	6.60 ± 0.28	···	···	···	1.00/90
80	81.7	52800.732	1.116 ± 0.003	30.82 ± 0.28	2.46 ± 0.01	···	···	3.65 ± 0.09	···	···	···	1.42/90
81	82.9	52801.915	1.145 ± 0.005	26.57 ± 0.29	2.71 ± 0.01	···	···	8.94 ± 0.30	···	···	···	1.41/90
82	84.0	52802.963	1.141 ± 0.005	26.01 ± 0.31	2.69 ± 0.01	···	···	9.39 ± 0.30	···	···	···	1.46/90
83	84.6	52803.568	1.132 ± 0.005	26.02 ± 0.31	2.67 ± 0.01	···	···	8.47 ± 0.26	···	···	···	1.02/90
84	85.6	52804.623	1.134 ± 0.006	24.66 ± 0.35	2.65 ± 0.01	···	···	10.00 ± 0.26	···	···	···	1.02/90
85	86.5	52805.472	1.131 ± 0.006	25.48 ± 0.34	2.68 ± 0.01	···	···	9.57 ± 0.29	···	···	···	1.36/90
86	87.6	52806.627	1.090 ± 0.004	31.43 ± 0.31	2.35 ± 0.01	···	···	2.47 ± 0.10	···	···	···	1.10/90
87	88.6	52807.619	1.102 ± 0.004	31.90 ± 0.29	2.25 ± 0.02	···	···	1.53 ± 0.09	···	···	···	1.01/90
88	89.6	52808.636	1.085 ± 0.003	32.45 ± 0.28	2.29 ± 0.01	···	···	1.67 ± 0.06	···	···	···	1.36/90
89	90.6	52809.620	1.079 ± 0.003	32.74 ± 0.28	2.31 ± 0.02	···	···	1.45 ± 0.06	···	···	···	1.05/90
90	91.5	52810.540	1.069 ± 0.003	33.46 ± 0.25	2.32 ± 0.03	···	···	0.72 ± 0.06	···	···	···	0.98/90
91	92.5	52811.461	1.074 ± 0.003	32.28 ± 0.27	2.19 ± 0.02	···	···	0.93 ± 0.05	···	···	···	1.26/90
92	93.7	52812.667	1.066 ± 0.003	32.65 ± 0.27	2.27 ± 0.02	···	···	1.04 ± 0.05	···	···	···	0.90/90
93	94.8	52813.828	1.066 ± 0.002	33.10 ± 0.24	2.26 ± 0.02	···	···	0.76 ± 0.03	···	···	···	0.92/90
94	95.5	52814.475	1.064 ± 0.003	33.49 ± 0.26	2.19 ± 0.03	···	···	0.57 ± 0.04	···	···	···	0.95/90
95	96.8	52815.836	1.051 ± 0.003	33.49 ± 0.25	2.33 ± 0.05	···	···	0.44 ± 0.06	···	···	···	0.84/90
96	97.6	52816.581	1.047 ± 0.002	33.39 ± 0.24	2.38 ± 0.04	···	···	0.50 ± 0.06	···	···	···	0.94/90
97	98.5	52817.509	1.047 ± 0.002	33.80 ± 0.25	2.31 ± 0.04	···	···	0.49 ± 0.05	···	···	···	0.85/90
98	99.5	52818.548	1.046 ± 0.002	33.83 ± 0.24	2.46 ± 0.05	···	···	0.56 ± 0.08	···	···	···	0.99/90
99	100.3	52819.343	1.039 ± 0.003	34.00 ± 0.27	2.35 ± 0.06	···	···	0.46 ± 0.07	···	···	···	0.73/90
100	101.4	52820.431	1.032 ± 0.003	34.47 ± 0.27	2.62 ± 0.10	···	···	0.55 ± 0.14	···	···	···	0.65/90
101	102.4	52821.416	1.030 ± 0.002	34.16 ± 0.28	3.39 ± 0.17	···	···	2.40 ± 1.04	···	···	···	0.75/90
102	103.5	52822.531	1.031 ± 0.002	33.93 ± 0.25	3.51 ± 0.15	···	···	2.95 ± 1.10	···	···	···	0.78/90
103	104.5	52823.482	1.028 ± 0.002	33.27 ± 0.26	3.57 ± 0.15	···	···	3.21 ± 1.20	···	···	···	1.19/90
104	105.5	52824.453	1.029 ± 0.002	33.22 ± 0.38	3.95 ± 0.16	···	···	6.42 ± 2.55	···	···	···	0.80/90
105	106.4	52825.366	1.024 ± 0.003	33.32 ± 0.44	3.96 ± 0.16	···	···	7.11 ± 2.74	···	···	···	0.97/90
106	107.4	52826.425	1.032 ± 0.002	33.01 ± 0.33	3.77 ± 0.14	···	···	5.29 ± 1.90	···	···	···	0.80/90
107	108.4	52827.411	1.030 ± 0.002	32.75 ± 0.33	3.73 ± 0.16	···	···	4.57 ± 1.78	···	···	···	0.84/90
108	109.4	52828.369	1.021 ± 0.002	33.96 ± 0.23	3.53 ± 0.14	···	···	2.73 ± 0.98	···	···	···	0.97/90
109	110.3	52829.277	1.018 ± 0.002	33.23 ± 0.32	3.82 ± 0.13	···	···	5.44 ± 1.83	···	···	···	1.03/90
110	111.2	52830.186	1.027 ± 0.003	33.13 ± 0.43	3.58 ± 0.24	···	···	3.15 ± 1.88	···	···	···	1.07/90
111	112.5	52831.483	1.016 ± 0.002	33.98 ± 0.30	3.62 ± 0.15	···	···	3.82 ± 1.43	···	···	···	0.74/90
112	115.2	52834.213	1.017 ± 0.002	33.37 ± 0.32	3.77 ± 0.14	···	···	4.95 ± 1.74	···	···	···	0.96/90
113	118.2	52837.201	1.017 ± 0.002	33.55 ± 0.36	3.88 ± 0.18	···	···	4.93 ± 2.17	···	···	···	1.35/90
114	121.6	52840.561	1.010 ± 0.003	34.68 ± 0.26	2.95 ± 0.17	···	···	0.76 ± 0.33	···	···	···	0.99/90
115	124.5	52843.513	1.003 ± 0.003	34.59 ± 0.28	2.56 ± 0.08	···	···	0.49 ± 0.10	···	···	···	1.13/90
116	127.2	52846.166	0.999 ± 0.002	34.58 ± 0.24	3.34 ± 0.15	···	···	1.72 ± 0.65	···	···	···	0.96/90
117	130.9	52849.911	0.988 ± 0.002	34.51 ± 0.29	3.66 ± 0.17	···	···	2.98 ± 1.28	···	···	···	1.06/90
118	131.9	52850.926	0.988 ± 0.003	34.22 ± 0.43	3.85 ± 0.16	···	···	5.49 ± 2.15	···	···	···	1.21/90
119	134.0	52852.991	0.983 ± 0.003	35.32 ± 0.28	3.13 ± 0.20	···	···	1.02 ± 0.51	···	···	···	0.88/90
120	136.5	52855.543	0.979 ± 0.002	34.65 ± 0.35	3.80 ± 0.17	···	···	4.06 ± 1.73	···	···	···	0.92/90
121	143.4	52862.382	0.963 ± 0.003	35.34 ± 0.29	3.11 ± 0.21	···	···	0.95 ± 0.49	···	···	···	0.89/90
122	146.4	52865.407	0.956 ± 0.002	34.38 ± 0.43	3.73 ± 0.18	···	···	3.84 ± 1.67	···	···	···	0.83/90

Table A1
(Continued)

Obs. No.	Day[a]	MJD[b]	T_{in} (keV)	R_{in}^{*}[c] (km)	Γ[d]	Γ_{HI}[e]	E_{break} (keV)	Power-law Norm.[f]	E_{line}[g] (keV)	FWHM[g] (keV)	Line Flux[g]	χ_ν^2/dof[h]
(1)	(2)	(3)	(4)	(5)	(6)	(7)	(8)	(9)	(10)	(11)	(12)	(13)
123	150.4	52869.351	0.952 ± 0.003	34.13 ± 0.38	3.47 ± 0.19	···	···	2.36 ± 1.08	···	···	···	0.70/90
124	156.1	52875.121	0.940 ± 0.003	34.81 ± 0.32	3.30 ± 0.21	···	···	1.35 ± 0.70	···	···	···	0.69/90
125	158.7	52877.700	0.933 ± 0.003	34.66 ± 0.65	3.76 ± 0.24	···	···	3.83 ± 2.22	···	···	···	1.09/90
126	164.3	52883.292	0.922 ± 0.003	34.51 ± 0.31	3.39 ± 0.15	···	···	1.75 ± 0.65	···	···	···	0.74/90
127	167.6	52886.574	0.926 ± 0.004	32.81 ± 0.70	4.26 ± 0.15	···	···	10.22 ± 3.45	···	···	···	3.16/90[k]
128	169.9	52888.932	0.909 ± 0.003	35.37 ± 0.33	3.30 ± 0.15	···	···	1.57 ± 0.57	···	···	···	1.77/90
129	172.4	52891.433	0.910 ± 0.003	35.39 ± 0.36	2.37 ± 0.05	···	···	0.36 ± 0.05	···	···	···	1.02/90
130	175.1	52894.054	0.908 ± 0.004	35.25 ± 0.42	2.23 ± 0.07	···	···	0.25 ± 0.05	···	···	···	1.14/90
131	179.7	52898.724	0.886 ± 0.004	35.06 ± 0.45	2.48 ± 0.09	···	···	0.40 ± 0.09	···	···	···	1.01/90
132	181.9	52900.879	0.879 ± 0.004	36.00 ± 0.42	3.13 ± 0.19	···	···	1.04 ± 0.48	···	···	···	0.96/90
133	185.0	52903.988	0.862 ± 0.004	36.33 ± 0.47	3.11 ± 0.17	···	···	1.20 ± 0.49	···	···	···	0.99/90
134	187.0	52905.958	0.860 ± 0.005	36.56 ± 0.58	2.37 ± 0.12	···	···	0.28 ± 0.09	···	···	···	0.94/90
135	187.1	52906.083	0.861 ± 0.003	35.71 ± 0.43	2.50 ± 0.07	···	···	0.38 ± 0.06	···	···	···	1.06/90
136	189.5	52908.515	0.864 ± 0.003	34.96 ± 0.43	2.31 ± 0.07	···	···	0.23 ± 0.04	···	···	···	1.04/90
137	190.6	52909.571	0.839 ± 0.011	37.44 ± 1.52	2.09 ± 0.06	···	···	0.17 ± 0.03	6.4 ± 2.0	1.5 ± 0.5	0.46 ± 0.39	1.11/87
138	192.5	52911.546	0.828 ± 0.011	38.16 ± 1.60	2.13 ± 0.03	···	···	0.28 ± 0.02	6.4 ± 1.4	1.3 ± 0.4	0.46 ± 0.32	1.06/87
139	193.5	52912.531	0.829 ± 0.009	37.41 ± 1.27	2.09 ± 0.03	···	···	0.33 ± 0.03	6.4 ± 1.8	1.6 ± 0.5	0.51 ± 0.36	1.06/87
140	195.5	52914.504	0.801 ± 0.011	39.22 ± 1.65	2.13 ± 0.07	···	···	0.17 ± 0.03	6.4 ± 1.4	1.4 ± 0.4	0.41 ± 0.28	1.02/87
141	197.4	52916.408	0.784 ± 0.010	39.11 ± 1.58	2.10 ± 0.04	···	···	0.24 ± 0.02	6.4 ± 1.1	1.4 ± 0.3	0.51 ± 0.24	0.92/87
142	198.6	52917.591	0.790 ± 0.011	37.70 ± 1.59	2.11 ± 0.04	···	···	0.23 ± 0.02	6.4 ± 1.2	1.3 ± 0.3	0.42 ± 0.25	1.03/87
143	201.1	52920.148	0.771 ± 0.008	37.94 ± 0.99	2.11 ± 0.10	···	···	0.11 ± 0.03	6.4 ± 1.7	1.7 ± 0.5	0.39 ± 0.24	0.93/87
144	202.5	52921.474	0.744 ± 0.007	39.65 ± 1.29	2.33 ± 0.08	···	···	0.22 ± 0.04	6.4 ± 0.7	1.0 ± 0.3	0.28 ± 0.12	0.88/87
145	205.2	52924.157	0.719 ± 0.008	40.86 ± 1.48	2.18 ± 0.07	···	···	0.14 ± 0.03	6.4 ± 0.8	1.2 ± 0.3	0.30 ± 0.12	0.73/87
146	207.2	52926.198	0.705 ± 0.008	39.67 ± 1.53	2.23 ± 0.06	···	···	0.19 ± 0.03	6.4 ± 1.0	1.3 ± 0.3	0.26 ± 0.12	1.24/87
147	208.1	52927.118	0.684 ± 0.007	41.86 ± 1.43	2.33 ± 0.06	···	···	0.21 ± 0.03	6.4 ± 0.6	1.1 ± 0.3	0.21 ± 0.08	0.98/87
148	209.5	52928.507	0.670 ± 0.008	42.34 ± 1.90	2.30 ± 0.07	···	···	0.22 ± 0.04	6.4 ± 0.7	1.0 ± 0.3	0.22 ± 0.09	0.96/87
149	210.4	52929.351	0.670 ± 0.007	40.89 ± 1.63	2.14 ± 0.05	···	···	0.17 ± 0.02	6.4 ± 0.5	1.1 ± 0.2	0.29 ± 0.08	1.38/87
150	211.0	52929.967	0.668 ± 0.007	40.14 ± 1.61	2.12 ± 0.04	···	···	0.18 ± 0.02	6.4 ± 0.6	1.2 ± 0.2	0.26 ± 0.08	0.87/87
151	212.0	52930.953	0.666 ± 0.010	37.90 ± 2.04	2.22 ± 0.03	···	···	0.38 ± 0.03	6.4 ± 0.5	1.1 ± 0.2	0.36 ± 0.10	0.78/87
152	213.1	52932.110	0.689 ± 0.016	29.08 ± 2.29	2.15 ± 0.03	···	···	0.43 ± 0.03	6.4 ± 0.6	1.3 ± 0.2	0.54 ± 0.14	0.66/87
153	214.3	52933.294	0.637 ± 0.008	39.74 ± 1.94	2.14 ± 0.04	···	···	0.20 ± 0.02	6.4 ± 0.6	1.2 ± 0.2	0.28 ± 0.08	0.94/87
154	215.0	52934.016	0.653 ± 0.014	33.16 ± 2.50	2.18 ± 0.03	···	···	0.37 ± 0.03	6.4 ± 0.5	1.2 ± 0.2	0.39 ± 0.10	0.91/87
155	216.1	52935.071	0.621 ± 0.011	37.70 ± 2.42	2.24 ± 0.04	···	···	0.31 ± 0.03	6.4 ± 0.7	1.2 ± 0.3	0.26 ± 0.09	1.15/87
156	217.0	52936.046	0.618 ± 0.015	33.50 ± 2.91	2.22 ± 0.04	···	···	0.37 ± 0.04	6.4 ± 0.6	1.2 ± 0.3	0.31 ± 0.10	0.99/87
157	218.0	52937.038	0.666 ± 0.022	22.37 ± 2.61	2.10 ± 0.03	···	···	0.34 ± 0.02	6.4 ± 0.6	1.4 ± 0.2	0.43 ± 0.11	1.14/87
158	219.0	52938.016	0.597 ± 0.033	24.69 ± 4.81	2.12 ± 0.04	···	···	0.38 ± 0.03	6.4 ± 0.9	1.4 ± 0.4	0.32 ± 0.13	1.11/87
159	220.1	52939.132	0.410 ± 0.013	73.50 ± 12.49	2.27 ± 0.01	···	···	0.51 ± 0.01	···	···	···	1.25/90
160	223.2	52942.154	0.499 ± 0.062	23.22 ± 11.80	1.96 ± 0.02	···	···	0.20 ± 0.01	6.6 ± 0.1	0.3 ± 0.4	0.08 ± 0.02	0.76/87
161	223.7	52942.700	0.377 ± 0.031	65.09 ± 29.15	1.99 ± 0.02	···	···	0.19 ± 0.01	6.7 ± 0.2	0.7 ± 0.3	0.08 ± 0.03	0.94/87
162	225.2	52944.200	0.443 ± 0.055	27.66 ± 16.31	1.93 ± 0.01	···	···	0.15 ± 0.01	6.6 ± 0.1	0.5 ± 0.2	0.07 ± 0.01	1.07/87
163	226.2	52945.178	0.687 ± 0.074	8.30 ± 2.96	1.76 ± 0.04	···	···	0.08 ± 0.01	6.4 ± 0.6	1.2 ± 0.3	0.19 ± 0.06	0.82/87
164	227.2	52946.171	···	···	1.99 ± 0.01	···	···	0.13 ± 0.01	6.7 ± 0.1	0.3 ± 0.6	0.03 ± 0.01	1.90/89
165	228.1	52947.053	···	···	1.99 ± 0.02	···	···	0.12 ± 0.01	···	···	···	1.15/92
166	229.2	52948.234	···	···	2.02 ± 0.01	···	···	0.11 ± 0.01	6.6 ± 0.1	0.3 ± 0.5	0.04 ± 0.01	1.55/89
167	230.2	52949.195	···	···	2.03 ± 0.01	···	···	0.10 ± 0.01	6.6 ± 0.1	0.3 ± 0.4	0.03 ± 0.01	1.70/89
168	231.5	52950.477	···	···	2.08 ± 0.01	···	···	0.07 ± 0.01	···	···	···	1.07/92
169	232.4	52951.425	···	···	2.12 ± 0.01	···	···	0.09 ± 0.01	6.7 ± 0.1	0.3 ± 0.5	0.04 ± 0.01	0.96/89
170	233.3	52952.276	···	···	2.14 ± 0.02	···	···	0.08 ± 0.01	6.7 ± 0.1	0.3 ± 0.7	0.03 ± 0.01	1.20/89

Notes.

[a] Number of days since discovery on 2003 March 21 = MJD 52719 (Revnivtsev et al. 2003); for calendar dates, see Table A3.

[b] Start time of observation. MJD = JD−2,400,000.5; for calendar dates, see Table A3.

[c] $R_{in}^{*} = R_{in}(\cos\theta)^{1/2}/(D/10\text{kpc})$, where θ is the inclination angle and D is the distance to the source in kpc.

[d] Photon index for energy band 3 keV to E_{break} for broken power-law fits and E_{break} to 200 keV index for simple power-law fits.

[e] Photon index for energy band E_{break} to 200 keV for broken power-law fits.

[f] Photons s^{-1} cm^{-2} keV^{-1} at 1 keV.

[g] Three Gaussian line parameters: central line energy, full width at half-maximum intensity, and Fe–K flux in photons s^{-1} cm^{-2}.

[h] Reduced χ^2; number of degrees of freedom.

[i] Fitted using data from HEXTE Cluster B because data from Cluster A saturated the telemetry.

[j] HEXTE fitting range restricted to $E = 32$–200 keV (includes HEXTE-A channels 17–56).

[k] PCA background appears to be overestimated in standard processing, which probably contributes to poor fit.

Table A2
Unabsorbed Flux Data[a], QPO Data, and State Classifications for H1743−322

Obs. No.	Day[b]	UT 2003 (mmdd)	Obs. Time (s)	Total 2–20 keV (10^{-8} cgs)	Disk 2–20 keV (10^{-8} cgs)	Power Law 2–20 keV (10^{-8} cgs)	2–20 keV Disk/Total	Power Law 20–100 keV (10^{-9} cgs)	QPO ν[c] (Hz)	QPO Amplitude[d] (% rms)	QPO Q[e]	Cont. r[f] (rms)	State[g]
1	7.8	0328	3472	$0.175^{+0.001}_{-0.001}$	$0.022^{+0.001}_{-0.001}$	$0.153^{+0.001}_{-0.001}$	$0.126^{+0.006}_{-0.006}$	$2.623^{+0.022}_{-0.029}$	0.063	3.63 ± 0.45	31.50 ± 11.07	0.242	?
2	10.8	0331	3488	$0.396^{+0.001}_{-0.002}$	...	$0.396^{+0.001}_{-0.001}$	...	$3.396^{+0.030}_{-0.023}$	0.159[h]	13.72 ± 0.58	3.79 ± 0.27	0.262	H[i]
3	14.8	0404	3472	$0.846^{+0.003}_{-0.005}$	...	$0.846^{+0.001}_{-0.001}$	...	$2.060^{+0.026}_{-0.034}$	2.23[j]	12.53 ± 0.23	11.64 ± 0.62	0.206	H:SPL
4	16.7	0406	3488	$1.067^{+0.003}_{-0.004}$	$0.216^{+0.001}_{-0.003}$	$0.851^{+0.002}_{-0.002}$	$0.202^{+0.002}_{-0.003}$	$1.824^{+0.017}_{-0.034}$	3.75[j]	12.32 ± 0.20	11.36 ± 0.35	0.173	H:SPL
5	18.6	0408	3568	$1.518^{+0.003}_{-0.006}$	...	$1.518^{+0.002}_{-0.002}$	...	$3.148^{+0.022}_{-0.026}$	2.08[j]	12.23 ± 0.27	11.56 ± 0.64	0.197	H:SPL
6	20.7	0410	3616	$1.760^{+0.004}_{-0.007}$	...	$1.760^{+0.002}_{-0.003}$	...	$2.500^{+0.027}_{-0.026}$	3.23[h]	12.22 ± 0.18	10.42 ± 0.34	0.177	H:SPL
7	22.8	0412	3024	$1.702^{+0.003}_{-0.006}$	$0.368^{+0.002}_{-0.004}$	$1.334^{+0.002}_{-0.003}$	$0.216^{+0.002}_{-0.003}$	$1.825^{+0.023}_{-0.029}$	7.22	6.10 ± 0.07	6.88 ± 0.13	0.122	SPL
8	24.2	0414	2672	$2.746^{+0.005}_{-0.011}$	$0.825^{+0.004}_{-0.005}$	$1.920^{+0.005}_{-0.005}$	$0.300^{+0.003}_{-0.002}$	$2.732^{+0.027}_{-0.031}$	8.53	4.30 ± 0.06	15.51 ± 0.28	0.112	SPL
9	25.2	0415	3024	$2.222^{+0.004}_{-0.007}$	$0.367^{+0.003}_{-0.004}$	$1.854^{+0.003}_{-0.003}$	$0.165^{+0.002}_{-0.002}$	$2.333^{+0.025}_{-0.028}$	5.63	9.02 ± 0.09	6.78 ± 0.08	0.137	SPL
10	27.2	0417	2880	$1.000^{+0.002}_{-0.004}$	$0.235^{+0.002}_{-0.002}$	$0.766^{+0.002}_{-0.002}$	$0.235^{+0.003}_{-0.002}$	$1.246^{+0.017}_{-0.021}$	4.74[h]	10.78 ± 0.15	8.78 ± 0.16	0.151	H:SPL
11	28.6	0418	3232	$1.491^{+0.003}_{-0.006}$	$0.274^{+0.002}_{-0.002}$	$1.218^{+0.002}_{-0.003}$	$0.184^{+0.002}_{-0.002}$	$1.509^{+0.020}_{-0.034}$	7.07	6.12 ± 0.07	6.49 ± 0.12	0.118	SPL
12	31.3	0421	5888	$3.192^{+0.007}_{-0.013}$	$1.029^{+0.005}_{-0.005}$	$2.163^{+0.005}_{-0.006}$	$0.322^{+0.003}_{-0.002}$	$3.448^{+0.011}_{-0.034}$	13.30	0.83 ± 0.07	5.59 ± 1.06	0.050	SPL
13	31.8	0421	15456	$2.894^{+0.007}_{-0.010}$	$0.940^{+0.005}_{-0.005}$	$1.954^{+0.004}_{-0.006}$	$0.325^{+0.003}_{-0.003}$	$2.934^{+0.009}_{-0.023}$	9.78	1.88 ± 0.03	9.31 ± 0.27	0.101	SPL
14	32.1	0422	6832	$2.322^{+0.005}_{-0.010}$	$0.912^{+0.004}_{-0.004}$	$1.410^{+0.004}_{-0.004}$	$0.393^{+0.003}_{-0.003}$	$2.288^{+0.009}_{-0.027}$	5.24[h]	1.75 ± 0.04	8.95 ± 0.82	0.101	SPL
15	32.3	0422	5376	$4.789^{+0.007}_{-0.016}$	$1.644^{+0.007}_{-0.011}$	$3.145^{+0.006}_{-0.008}$	$0.343^{+0.003}_{-0.003}$	$4.043^{+0.017}_{-0.025}$	9.71	1.31 ± 0.04	12.14 ± 0.91	0.085	SPL[k]
16	32.7	0422	3280	$2.499^{+0.006}_{-0.011}$	$1.024^{+0.004}_{-0.006}$	$1.476^{+0.004}_{-0.004}$	$0.410^{+0.003}_{-0.003}$	$2.090^{+0.026}_{-0.033}$	5.73[l]	4.32 ± 0.07	3.54 ± 0.02	0.104	SPL
17	33.0	0422	3696	$2.416^{+0.005}_{-0.008}$	$1.111^{+0.004}_{-0.005}$	$1.305^{+0.004}_{-0.004}$	$0.460^{+0.003}_{-0.003}$	$1.709^{+0.019}_{-0.033}$	5.97	4.98 ± 0.05	3.03 ± 0.02	0.089	SPL
18	34.0	0423	10752	$3.165^{+0.006}_{-0.013}$	$1.022^{+0.005}_{-0.006}$	$2.143^{+0.004}_{-0.006}$	$0.323^{+0.003}_{-0.003}$	$3.399^{+0.014}_{-0.023}$	9.78[m]	1.11 ± 0.04	10.87 ± 0.85	0.077	SPL
19	34.2	0424	2944	$3.093^{+0.007}_{-0.014}$	$0.946^{+0.005}_{-0.005}$	$2.148^{+0.004}_{-0.004}$	$0.306^{+0.003}_{-0.002}$	$3.471^{+0.027}_{-0.035}$	11.74	0.74 ± 0.11	46.96 ± 9.40	0.048	SPL
20	35.6	0425	3472	$2.457^{+0.005}_{-0.008}$	$0.942^{+0.004}_{-0.004}$	$1.515^{+0.005}_{-0.004}$	$0.383^{+0.003}_{-0.002}$	$2.314^{+0.026}_{-0.034}$	9.90[n]	2.08 ± 0.05	9.71 ± 0.57	0.117	SPL
21	37.0	0426	3664	$3.762^{+0.007}_{-0.014}$	$2.269^{+0.009}_{-0.007}$	$1.493^{+0.006}_{-0.005}$	$0.603^{+0.005}_{-0.003}$	$1.673^{+0.013}_{-0.019}$	7.76[o]	2.62 ± 0.04	2.50 ± 0.12	0.073	SPL
22	37.2	0427	2224	$3.318^{+0.006}_{-0.011}$	$1.897^{+0.006}_{-0.008}$	$1.421^{+0.004}_{-0.005}$	$0.572^{+0.004}_{-0.003}$	$1.582^{+0.021}_{-0.026}$	5.96[p]	3.61 ± 0.08	1.25 ± 0.07	0.069	SPL
23	37.7	0427	3136	$1.789^{+0.003}_{-0.008}$	$0.909^{+0.002}_{-0.004}$	$0.880^{+0.002}_{-0.003}$	$0.508^{+0.003}_{-0.003}$	$0.909^{+0.045}_{-0.041}$	4.96[h]	2.68 ± 0.07	3.97 ± 0.22	0.074	SPL
24	38.8	0428	6976	$1.580^{+0.002}_{-0.006}$	$1.273^{+0.003}_{-0.003}$	$0.307^{+0.002}_{-0.002}$	$0.806^{+0.005}_{-0.003}$	$0.763^{+0.009}_{-0.030}$	...	...	...	0.070	TD
25	40.0	0429	3472	$2.974^{+0.005}_{-0.011}$	$2.440^{+0.007}_{-0.007}$	$0.534^{+0.004}_{-0.004}$	$0.820^{+0.005}_{-0.004}$	$0.216^{+0.008}_{-0.014}$	...	...	...	0.055	TD
26	41.1	0501	3488	$1.591^{+0.003}_{-0.007}$	$1.307^{+0.003}_{-0.004}$	$0.284^{+0.002}_{-0.001}$	$0.821^{+0.006}_{-0.004}$	$0.821^{+0.010}_{-0.053}$	...	...	...	0.063	TD
27	41.6	0501	3696	$1.633^{+0.003}_{-0.006}$	$1.345^{+0.003}_{-0.004}$	$0.288^{+0.002}_{-0.002}$	$0.824^{+0.005}_{-0.004}$	$0.783^{+0.018}_{-0.041}$	...	...	...	0.071	TD
28	41.8	0501	16096	$2.333^{+0.004}_{-0.008}$	$1.934^{+0.004}_{-0.006}$	$0.399^{+0.003}_{-0.004}$	$0.829^{+0.005}_{-0.004}$	$1.000^{+0.072}_{-0.019}$	...	...	...	0.066	TD
29	42.0	0502	4256	$2.400^{+0.004}_{-0.011}$	$2.062^{+0.005}_{-0.005}$	$0.338^{+0.003}_{-0.004}$	$0.859^{+0.006}_{-0.004}$	$0.581^{+0.019}_{-0.039}$	...	...	...	0.060	TD
30	42.6	0502	5184	$2.396^{+0.005}_{-0.010}$	$1.960^{+0.004}_{-0.006}$	$0.436^{+0.002}_{-0.003}$	$0.818^{+0.005}_{-0.004}$	$1.138^{+0.015}_{-0.035}$	...	...	...	0.066	TD
31	43.7	0503	6528	$2.457^{+0.003}_{-0.010}$	$1.816^{+0.004}_{-0.005}$	$0.640^{+0.003}_{-0.004}$	$0.739^{+0.005}_{-0.003}$	$1.777^{+0.012}_{-0.038}$	...	...	...	0.067	TD:SPL
32	44.1	0504	3408	$2.841^{+0.004}_{-0.010}$	$1.822^{+0.005}_{-0.004}$	$1.019^{+0.005}_{-0.004}$	$0.641^{+0.004}_{-0.002}$	$1.419^{+0.019}_{-0.031}$	7.82[q]	2.75 ± 0.05	2.52 ± 0.11	0.059	SPL
33	44.6	0504	2736	$3.225^{+0.005}_{-0.012}$	$1.532^{+0.006}_{-0.005}$	$1.693^{+0.004}_{-0.007}$	$0.475^{+0.004}_{-0.002}$	$1.947^{+0.039}_{-0.038}$	5.43[h]	3.78 ± 0.05	2.47 ± 0.07	0.061	SPL
34	45.9	0505	6752	$3.253^{+0.005}_{-0.013}$	$1.487^{+0.007}_{-0.007}$	$1.766^{+0.004}_{-0.004}$	$0.457^{+0.004}_{-0.003}$	$1.946^{+0.014}_{-0.027}$	5.46[h]	3.79 ± 0.03	2.87 ± 0.05	0.062	SPL
35	46.9	0506	3408	$5.146^{+0.009}_{-0.022}$	$1.317^{+0.008}_{-0.008}$	$3.829^{+0.007}_{-0.010}$	$0.256^{+0.003}_{-0.002}$	$6.923^{+0.028}_{-0.040}$	11.16	1.21 ± 0.05	4.24 ± 0.41	0.047	SPL
36	47.6	0507	2544	$2.303^{+0.004}_{-0.007}$	$0.371^{+0.003}_{-0.006}$	$1.932^{+0.003}_{-0.004}$	$0.161^{+0.002}_{-0.003}$	$2.713^{+0.041}_{-0.069}$	5.62[l]	9.20 ± 0.11	7.21 ± 0.09	0.143	SPL
37	48.9	0508	6784	$1.894^{+0.002}_{-0.006}$	$0.227^{+0.003}_{-0.005}$	$1.666^{+0.002}_{-0.002}$	$0.120^{+0.002}_{-0.003}$	$2.344^{+0.021}_{-0.018}$	4.43[h]	11.42 ± 0.10	9.04 ± 0.19	0.159	H:SPL
38	49.5	0509	2160	$1.895^{+0.003}_{-0.005}$	$0.318^{+0.003}_{-0.004}$	$1.577^{+0.003}_{-0.003}$	$0.168^{+0.002}_{-0.002}$	$2.194^{+0.026}_{-0.029}$	5.39[l]	10.07 ± 0.14	7.59 ± 0.11	0.149	SPL
39	50.7	0510	2432	$1.783^{+0.002}_{-0.007}$	$0.252^{+0.002}_{-0.004}$	$1.530^{+0.002}_{-0.003}$	$0.141^{+0.002}_{-0.002}$	$2.187^{+0.019}_{-0.037}$	4.91[h]	10.78 ± 0.14	10.02 ± 0.21	0.159	H:SPL
40	51.5	0511	3728	$2.207^{+0.003}_{-0.007}$	$0.419^{+0.003}_{-0.004}$	$1.788^{+0.003}_{-0.003}$	$0.190^{+0.002}_{-0.002}$	$2.556^{+0.033}_{-0.043}$	6.16	8.34 ± 0.08	7.25 ± 0.09	0.140	SPL
41	52.9	0512	7680	$1.536^{+0.003}_{-0.008}$	$0.112^{+0.001}_{-0.005}$	$1.424^{+0.002}_{-0.002}$	$0.073^{+0.001}_{-0.003}$	$2.798^{+0.017}_{-0.022}$	2.76[j]	12.01 ± 0.14	8.62 ± 0.27	0.192	H:SPL
42	53.7	0513	6080	$1.374^{+0.003}_{-0.009}$	...	$1.374^{+0.002}_{-0.002}$	...	$3.360^{+0.021}_{-0.022}$	1.84[j]	12.87 ± 0.17	9.20 ± 0.46	0.214	H:SPL
43	54.7	0514	6768	$1.351^{+0.004}_{-0.010}$	...	$1.351^{+0.002}_{-0.002}$	...	$3.274^{+0.020}_{-0.021}$	1.91[j]	12.71 ± 0.17	9.55 ± 0.48	0.212	H:SPL
44	55.6	0515	6656	$1.465^{+0.002}_{-0.005}$	$0.088^{+0.001}_{-0.004}$	$1.377^{+0.002}_{-0.002}$	$0.060^{+0.001}_{-0.003}$	$2.572^{+0.015}_{-0.025}$	3.16[j]	12.51 ± 0.14	6.58 ± 0.14	0.194	H:SPL
45	56.6	0516	6704	$1.304^{+0.003}_{-0.006}$	...	$1.304^{+0.002}_{-0.002}$	...	$2.935^{+0.018}_{-0.021}$	2.15[j]	13.07 ± 0.17	9.77 ± 0.44	0.212	H:SPL
46	57.7	0517	6592	$0.969^{+0.002}_{-0.003}$	...	$0.969^{+0.001}_{-0.002}$	...	$2.936^{+0.019}_{-0.014}$	1.72[j]	13.56 ± 0.18	7.48 ± 0.33	0.227	H
47	58.7	0518	6576	$1.367^{+0.003}_{-0.008}$	...	$1.367^{+0.003}_{-0.002}$	...	$2.874^{+0.015}_{-0.021}$	2.51[j]	12.91 ± 0.16	10.46 ± 0.44	0.207	H:SPL
48	59.5	0519	6544	$1.431^{+0.002}_{-0.006}$	$0.104^{+0.001}_{-0.004}$	$1.327^{+0.003}_{-0.002}$	$0.073^{+0.001}_{-0.003}$	$2.518^{+0.012}_{-0.014}$	3.24[j]	12.94 ± 0.14	8.76 ± 0.24	0.192	H:SPL
49	60.6	0520	4848	$1.547^{+0.003}_{-0.006}$	$0.153^{+0.001}_{-0.003}$	$1.394^{+0.002}_{-0.002}$	$0.099^{+0.001}_{-0.002}$	$2.339^{+0.018}_{-0.023}$	3.82[j]	12.58 ± 0.15	11.24 ± 0.33	0.187	H:SPL

Table A2
(Continued)

Obs. No.	Day[b]	UT 2003 (mmdd)	Obs. Time (s)	Total 2–20 keV (10^{-8} cgs)	Disk 2–20 keV (10^{-8} cgs)	Power Law 2–20 keV (10^{-8} cgs)	2–20 keV Disk/Total	Power Law 20–100 keV (10^{-9} cgs)	QPO ν[c] (Hz)	QPO Amplitude[d] (% rms)	QPO Q[e]	Cont. r[f] (rms)	State[g]
50	61.6	0521	3376	$1.562^{+0.002}_{-0.006}$	$0.168^{+0.001}_{-0.004}$	$1.394^{+0.002}_{-0.003}$	$0.108^{+0.001}_{-0.003}$	$2.445^{+0.028}_{-0.027}$	3.83[j]	12.49 ± 0.18	11.26 ± 0.33	0.184	H:SPL
51	62.6	0522	6816	$1.497^{+0.002}_{-0.006}$	$0.149^{+0.002}_{-0.004}$	$1.348^{+0.002}_{-0.002}$	$0.100^{+0.002}_{-0.003}$	$2.431^{+0.016}_{-0.024}$	3.64[j]	12.88 ± 0.13	9.33 ± 0.24	0.191	H:SPL
52	63.7	0523	3232	$1.582^{+0.001}_{-0.005}$	$0.256^{+0.002}_{-0.003}$	$1.325^{+0.002}_{-0.002}$	$0.162^{+0.002}_{-0.002}$	$2.214^{+0.021}_{-0.027}$	4.70[j]	11.50 ± 0.15	11.19 ± 0.27	0.173	TD:SPL
53	64.5	0524	6512	$2.041^{+0.004}_{-0.008}$	$0.511^{+0.003}_{-0.005}$	$1.530^{+0.002}_{-0.003}$	$0.250^{+0.002}_{-0.003}$	$2.552^{+0.016}_{-0.025}$	7.08	6.37 ± 0.05	6.10 ± 0.11	0.129	SPL
54	65.6	0525	6688	$2.951^{+0.004}_{-0.011}$	$1.420^{+0.006}_{-0.004}$	$1.531^{+0.004}_{-0.004}$	$0.481^{+0.004}_{-0.002}$	$2.619^{+0.014}_{-0.025}$	5.72	5.92 ± 0.04	2.07 ± 0.02	0.078	SPL
55	66.5	0526	6720	$3.059^{+0.005}_{-0.010}$	$1.406^{+0.005}_{-0.007}$	$1.653^{+0.004}_{-0.005}$	$0.460^{+0.003}_{-0.003}$	$2.737^{+0.016}_{-0.033}$	5.66[r]	6.07 ± 0.03	1.83 ± 0.02	0.083	SPL
56	67.3	0527	6448	$3.522^{+0.007}_{-0.012}$	$1.190^{+0.006}_{-0.004}$	$2.333^{+0.005}_{-0.006}$	$0.338^{+0.003}_{-0.002}$	$3.935^{+0.014}_{-0.041}$	9.42	2.06 ± 0.04	11.46 ± 0.42	0.067	SPL
57	67.8	0527	2224	$3.023^{+0.005}_{-0.013}$	$1.309^{+0.006}_{-0.007}$	$1.714^{+0.004}_{-0.005}$	$0.433^{+0.004}_{-0.003}$	$2.852^{+0.029}_{-0.044}$	5.48[h]	6.01 ± 0.07	1.77 ± 0.05	0.089	SPL
58	68.0	0528	1504	$2.903^{+0.004}_{-0.013}$	$1.392^{+0.004}_{-0.006}$	$1.511^{+0.004}_{-0.005}$	$0.480^{+0.004}_{-0.003}$	$2.243^{+0.027}_{-0.054}$	5.54	4.83 ± 0.08	3.30 ± 0.12	0.067	SPL
59	68.2	0528	1456	$2.566^{+0.003}_{-0.011}$	$1.499^{+0.005}_{-0.005}$	$1.067^{+0.004}_{-0.005}$	$0.584^{+0.004}_{-0.003}$	$1.688^{+0.037}_{-0.042}$	4.78[s]	2.90 ± 0.06	6.64 ± 0.28	0.055	SPL
60	68.5	0528	22496	$2.963^{+0.004}_{-0.009}$	$1.388^{+0.005}_{-0.006}$	$1.575^{+0.004}_{-0.003}$	$0.468^{+0.003}_{-0.003}$	$2.289^{+0.009}_{-0.020}$	5.68[t]	5.33 ± 0.02	2.48 ± 0.02	0.068	SPL
61	69.0	0529	1728	$3.024^{+0.004}_{-0.012}$	$1.285^{+0.005}_{-0.005}$	$1.739^{+0.003}_{-0.005}$	$0.425^{+0.003}_{-0.002}$	$2.808^{+0.040}_{-0.047}$	5.74	5.67 ± 0.07	2.21 ± 0.05	0.078	SPL
62	69.5	0529	7104	$2.324^{+0.003}_{-0.008}$	$1.495^{+0.005}_{-0.004}$	$0.829^{+0.002}_{-0.004}$	$0.643^{+0.004}_{-0.003}$	$1.397^{+0.011}_{-0.024}$	8.74[u]	2.71 ± 0.04	3.78 ± 0.13	0.056	SPL
63	69.9	0529	2192	$2.539^{+0.003}_{-0.010}$	$1.964^{+0.006}_{-0.006}$	$0.574^{+0.003}_{-0.004}$	$0.774^{+0.005}_{-0.003}$	$1.957^{+0.022}_{-0.108}$	...	...	...	0.044	TD
64	70.3	0530	3488	$2.765^{+0.004}_{-0.011}$	$1.463^{+0.006}_{-0.006}$	$1.302^{+0.004}_{-0.004}$	$0.529^{+0.004}_{-0.003}$	$1.933^{+0.024}_{-0.027}$	5.22[v]	3.93 ± 0.05	4.42 ± 0.11	0.057	SPL
65	70.9	0530	2112	$2.632^{+0.005}_{-0.012}$	$1.411^{+0.005}_{-0.005}$	$1.221^{+0.004}_{-0.004}$	$0.536^{+0.004}_{-0.003}$	$1.931^{+0.040}_{-0.040}$	5.36[h]	4.32 ± 0.06	3.33 ± 0.11	0.057	SPL
66	71.1	0531	3056	$2.495^{+0.004}_{-0.010}$	$1.362^{+0.004}_{-0.005}$	$1.133^{+0.004}_{-0.004}$	$0.546^{+0.004}_{-0.003}$	$1.991^{+0.019}_{-0.032}$	5.52[h]	4.53 ± 0.06	2.71 ± 0.07	0.064	SPL
67	71.2	0531	3984	$2.566^{+0.005}_{-0.011}$	$1.450^{+0.004}_{-0.005}$	$1.116^{+0.004}_{-0.004}$	$0.565^{+0.004}_{-0.003}$	$1.764^{+0.019}_{-0.032}$	5.03[v]	3.52 ± 0.05	4.30 ± 0.11	0.055	SPL
68	71.9	0531	2192	$2.418^{+0.003}_{-0.009}$	$1.769^{+0.004}_{-0.005}$	$0.649^{+0.003}_{-0.003}$	$0.732^{+0.004}_{-0.003}$	$1.626^{+0.032}_{-0.054}$	7.24	1.63 ± 0.14	2.34 ± 0.64	0.047	SPL
69	72.6	0601	5792	$2.484^{+0.004}_{-0.010}$	$1.496^{+0.005}_{-0.006}$	$0.988^{+0.003}_{-0.004}$	$0.602^{+0.004}_{-0.003}$	$1.664^{+0.019}_{-0.041}$	4.91[v]	3.18 ± 0.04	4.86 ± 0.15	0.061	SPL
70	73.0	0602	1936	$2.223^{+0.003}_{-0.010}$	$1.541^{+0.004}_{-0.006}$	$0.682^{+0.003}_{-0.004}$	$0.693^{+0.005}_{-0.004}$	$1.330^{+0.034}_{-0.041}$	7.15	2.72 ± 0.09	2.31 ± 0.21	0.047	SPL
71	73.4	0602	6752	$2.530^{+0.004}_{-0.011}$	$1.374^{+0.004}_{-0.005}$	$1.156^{+0.004}_{-0.004}$	$0.543^{+0.004}_{-0.003}$	$1.790^{+0.013}_{-0.029}$	5.22[h]	4.08 ± 0.04	3.87 ± 0.06	0.056	SPL
72	74.0	0603	1856	$2.168^{+0.003}_{-0.011}$	$1.486^{+0.004}_{-0.005}$	$0.682^{+0.003}_{-0.002}$	$0.685^{+0.005}_{-0.003}$	$1.275^{+0.029}_{-0.044}$	5.22	2.72 ± 0.09	2.78 ± 0.24	0.046	SPL
73	74.6	0603	3136	$2.567^{+0.003}_{-0.010}$	$1.529^{+0.007}_{-0.005}$	$1.038^{+0.003}_{-0.004}$	$0.596^{+0.005}_{-0.003}$	$1.713^{+0.022}_{-0.038}$	4.83[v]	3.69 ± 0.06	4.93 ± 0.15	0.052	SPL
74	75.6	0604	7280	$3.544^{+0.005}_{-0.015}$	$1.245^{+0.006}_{-0.006}$	$2.299^{+0.004}_{-0.005}$	$0.351^{+0.003}_{-0.002}$	$4.415^{+0.017}_{-0.035}$	10.28[w]	1.28 ± 0.05	3.32 ± 0.34	0.030	SPL
75	76.4	0605	3712	$2.308^{+0.004}_{-0.009}$	$1.486^{+0.005}_{-0.007}$	$0.821^{+0.004}_{-0.003}$	$0.644^{+0.005}_{-0.004}$	$1.474^{+0.023}_{-0.039}$	8.15[w]	2.79 ± 0.07	2.63 ± 0.16	0.050	SPL
76	77.3	0606	7024	$2.599^{+0.004}_{-0.010}$	$1.353^{+0.004}_{-0.005}$	$1.246^{+0.004}_{-0.004}$	$0.521^{+0.004}_{-0.003}$	$1.970^{+0.012}_{-0.021}$	5.42[h]	4.89 ± 0.04	2.77 ± 0.04	0.060	SPL
77	78.6	0607	7120	$2.617^{+0.005}_{-0.010}$	$1.290^{+0.004}_{-0.005}$	$1.327^{+0.003}_{-0.005}$	$0.493^{+0.003}_{-0.003}$	$2.189^{+0.022}_{-0.035}$	5.58[l]	5.32 ± 0.03	2.55 ± 0.02	0.066	SPL
78	79.5	0609	3296	$3.663^{+0.005}_{-0.015}$	$1.174^{+0.006}_{-0.006}$	$2.488^{+0.006}_{-0.006}$	$0.321^{+0.003}_{-0.002}$	$4.913^{+0.025}_{-0.042}$	9.58	1.22 ± 0.09	5.70 ± 0.99	0.029	SPL
79	80.5	0609	2976	$2.260^{+0.003}_{-0.008}$	$1.468^{+0.003}_{-0.005}$	$0.792^{+0.003}_{-0.004}$	$0.650^{+0.004}_{-0.003}$	$1.452^{+0.019}_{-0.044}$	4.60[v]	2.96 ± 0.05	4.26 ± 0.16	0.048	SPL
80	81.7	0610	11568	$2.223^{+0.004}_{-0.007}$	$1.619^{+0.003}_{-0.005}$	$0.604^{+0.003}_{-0.002}$	$0.728^{+0.004}_{-0.004}$	$1.676^{+0.010}_{-0.035}$	8.60[w]	1.47 ± 0.05	2.77 ± 0.27	0.035	SPL
81	82.9	0611	4832	$2.358^{+0.004}_{-0.009}$	$1.365^{+0.003}_{-0.006}$	$0.993^{+0.003}_{-0.003}$	$0.579^{+0.003}_{-0.004}$	$1.638^{+0.013}_{-0.028}$	4.92[h]	4.07 ± 0.04	4.87 ± 0.10	0.055	SPL
82	84.0	0612	4544	$2.361^{+0.003}_{-0.009}$	$1.286^{+0.004}_{-0.005}$	$1.076^{+0.004}_{-0.003}$	$0.545^{+0.004}_{-0.003}$	$1.851^{+0.016}_{-0.029}$	5.29[h]	4.59 ± 0.05	3.78 ± 0.08	0.057	SPL
83	84.6	0613	6304	$2.239^{+0.003}_{-0.008}$	$1.238^{+0.003}_{-0.006}$	$1.001^{+0.003}_{-0.004}$	$0.553^{+0.003}_{-0.003}$	$1.796^{+0.014}_{-0.028}$	5.26[h]	4.00 ± 0.04	4.53 ± 0.08	0.058	SPL
84	85.6	0614	6768	$2.341^{+0.002}_{-0.007}$	$1.122^{+0.004}_{-0.004}$	$1.219^{+0.003}_{-0.004}$	$0.479^{+0.003}_{-0.002}$	$2.281^{+0.017}_{-0.029}$	5.62[l]	5.54 ± 0.04	1.81 ± 0.02	0.069	SPL
85	86.5	0615	4992	$2.295^{+0.004}_{-0.008}$	$1.182^{+0.003}_{-0.005}$	$1.113^{+0.003}_{-0.005}$	$0.515^{+0.003}_{-0.003}$	$1.956^{+0.021}_{-0.036}$	5.53[l]	5.38 ± 0.04	2.55 ± 0.04	0.063	SPL
86	87.6	0616	3312	$1.990^{+0.003}_{-0.008}$	$1.499^{+0.004}_{-0.004}$	$0.491^{+0.002}_{-0.003}$	$0.753^{+0.005}_{-0.003}$	$1.707^{+0.017}_{-0.042}$	...	...	...	0.032	TD
87	88.6	0617	2416	$1.991^{+0.004}_{-0.009}$	$1.630^{+0.004}_{-0.005}$	$0.361^{+0.002}_{-0.002}$	$0.819^{+0.006}_{-0.004}$	$1.536^{+0.048}_{-0.081}$	...	...	...	0.033	TD
88	89.6	0618	5824	$1.929^{+0.003}_{-0.006}$	$1.562^{+0.004}_{-0.004}$	$0.368^{+0.002}_{-0.002}$	$0.810^{+0.005}_{-0.003}$	$1.443^{+0.076}_{-0.042}$	...	...	...	0.032	TD
89	90.6	0619	5184	$1.855^{+0.003}_{-0.008}$	$1.547^{+0.004}_{-0.004}$	$0.308^{+0.002}_{-0.002}$	$0.834^{+0.006}_{-0.003}$	$1.163^{+0.015}_{-0.037}$	...	...	...	0.033	TD
90	91.5	0620	5728	$1.693^{+0.002}_{-0.007}$	$1.542^{+0.003}_{-0.003}$	$0.151^{+0.001}_{-0.003}$	$0.911^{+0.006}_{-0.003}$	$0.556^{+0.010}_{-0.050}$	...	...	...	0.033	TD
91	92.5	0621	4192	$1.713^{+0.002}_{-0.008}$	$1.469^{+0.003}_{-0.003}$	$0.244^{+0.002}_{-0.002}$	$0.858^{+0.006}_{-0.003}$	$1.169^{+0.018}_{-0.042}$	...	...	...	0.035	TD
92	93.7	0622	4832	$1.685^{+0.003}_{-0.007}$	$1.448^{+0.003}_{-0.004}$	$0.237^{+0.001}_{-0.002}$	$0.859^{+0.005}_{-0.004}$	$0.969^{+0.011}_{-0.040}$	...	...	...	0.038	TD
93	94.8	0623	13488	$1.664^{+0.003}_{-0.007}$	$1.488^{+0.003}_{-0.004}$	$0.176^{+0.001}_{-0.002}$	$0.894^{+0.006}_{-0.004}$	$0.735^{+0.030}_{-0.029}$	14.74	0.87 ± 0.10	8.38 ± 2.48	0.030	TD:SPL
94	95.5	0624	3904	$1.659^{+0.002}_{-0.007}$	$1.509^{+0.004}_{-0.004}$	$0.149^{+0.001}_{-0.002}$	$0.910^{+0.006}_{-0.004}$	$0.717^{+0.016}_{-0.052}$	...	...	...	0.027	TD
95	96.8	0625	3264	$1.510^{+0.003}_{-0.004}$	$1.419^{+0.004}_{-0.002}$	$0.090^{+0.001}_{-0.001}$	$0.940^{+0.005}_{-0.003}$	$0.328^{+0.012}_{-0.081}$	...	...	...	0.030	TD
96	97.6	0626	4816	$1.479^{+0.003}_{-0.005}$	$1.384^{+0.003}_{-0.003}$	$0.094^{+0.001}_{-0.001}$	$0.936^{+0.005}_{-0.004}$	$0.309^{+0.013}_{-0.031}$	...	...	...	0.030	TD
97	98.5	0627	5696	$1.523^{+0.003}_{-0.005}$	$1.418^{+0.004}_{-0.002}$	$0.104^{+0.001}_{-0.001}$	$0.931^{+0.006}_{-0.003}$	$0.393^{+0.013}_{-0.030}$	...	...	...	0.029	TD
98	99.5	0628	4624	$1.507^{+0.002}_{-0.006}$	$1.414^{+0.004}_{-0.003}$	$0.093^{+0.001}_{-0.001}$	$0.938^{+0.006}_{-0.003}$	$0.257^{+0.012}_{-0.036}$	...	...	...	0.028	TD

Table A2
(Continued)

Obs. No.	Day[b]	UT 2003 (mmdd)	Obs. Time (s)	Total 2–20 keV (10^{-8} cgs)	Disk 2–20 keV (10^{-8} cgs)	Power Law 2–20 keV (10^{-8} cgs)	2–20 keV Disk/Total	Power Law 20–100 keV (10^{-9} cgs)	QPO ν[c] (Hz)	QPO Amplitude[d] (% rms)	QPO Q[e]	Cont. r[f] (rms)	State[g]
99	100.3	0629	2688	$1.472^{+0.003}_{-0.005}$	$1.381^{+0.003}_{-0.004}$	$0.091^{+0.001}_{-0.001}$	$0.938^{+0.005}_{-0.005}$	$0.318^{+0.016}_{-0.048}$	...	...	...	0.029	TD
100	101.4	0630	2384	$1.442^{+0.003}_{-0.006}$	$1.372^{+0.004}_{-0.003}$	$0.070^{+0.001}_{-0.002}$	$0.951^{+0.007}_{-0.004}$	$0.140^{+0.022}_{-0.038}$	...	...	...	0.029	TD
101	102.4	0701	2304	$1.436^{+0.002}_{-0.009}$	$1.334^{+0.003}_{-0.003}$	$0.101^{+0.002}_{-0.002}$	$0.929^{+0.008}_{-0.003}$	$0.038^{+0.002}_{-0.006}$	...	...	...	0.028	TD
102	103.5	0702	4384	$1.429^{+0.002}_{-0.008}$	$1.323^{+0.002}_{-0.004}$	$0.107^{+0.001}_{-0.002}$	$0.926^{+0.007}_{-0.004}$	$0.031^{+0.002}_{-0.006}$	...	...	...	0.025	TD
103	104.5	0703	4736	$1.361^{+0.002}_{-0.009}$	$1.254^{+0.002}_{-0.003}$	$0.107^{+0.001}_{-0.002}$	$0.921^{+0.008}_{-0.004}$	$0.027^{+0.001}_{-0.004}$	...	...	...	0.024	TD
104	105.5	0704	3328	$1.391^{+0.001}_{-0.007}$	$1.256^{+0.003}_{-0.003}$	$0.135^{+0.002}_{-0.003}$	$0.903^{+0.007}_{-0.003}$	$0.015^{+0.001}_{-0.001}$	...	...	...	0.027	TD
105	106.4	0705	2192	$1.381^{+0.002}_{-0.008}$	$1.233^{+0.003}_{-0.003}$	$0.148^{+0.002}_{-0.002}$	$0.893^{+0.007}_{-0.003}$	$0.016^{+0.001}_{-0.003}$	...	...	...	0.031	TD
106	107.4	0706	3360	$1.396^{+0.002}_{-0.007}$	$1.258^{+0.002}_{-0.003}$	$0.138^{+0.002}_{-0.002}$	$0.901^{+0.006}_{-0.003}$	$0.022^{+0.001}_{-0.003}$	...	...	...	0.026	TD
107	108.4	0707	3264	$1.352^{+0.002}_{-0.009}$	$1.227^{+0.003}_{-0.004}$	$0.125^{+0.002}_{-0.002}$	$0.908^{+0.008}_{-0.004}$	$0.022^{+0.001}_{-0.003}$	...	...	...	0.028	TD
108	109.4	0708	6672	$1.358^{+0.001}_{-0.008}$	$1.262^{+0.002}_{-0.003}$	$0.096^{+0.001}_{-0.002}$	$0.929^{+0.007}_{-0.003}$	$0.027^{+0.001}_{-0.004}$	...	...	...	0.026	TD
109	110.3	0709	4944	$1.324^{+0.001}_{-0.006}$	$1.190^{+0.003}_{-0.003}$	$0.134^{+0.002}_{-0.002}$	$0.899^{+0.006}_{-0.003}$	$0.019^{+0.001}_{-0.003}$	...	...	...	0.025	TD
110	111.2	0710	928	$1.341^{+0.001}_{-0.008}$	$1.237^{+0.003}_{-0.004}$	$0.104^{+0.002}_{-0.002}$	$0.922^{+0.008}_{-0.004}$	$0.026^{+0.001}_{-0.007}$	...	...	...	0.027	TD
111	112.5	0711	3376	$1.352^{+0.001}_{-0.009}$	$1.232^{+0.003}_{-0.004}$	$0.120^{+0.001}_{-0.003}$	$0.911^{+0.008}_{-0.004}$	$0.027^{+0.001}_{-0.005}$	...	...	...	0.025	TD
112	115.2	0714	4400	$1.324^{+0.001}_{-0.009}$	$1.194^{+0.003}_{-0.003}$	$0.129^{+0.002}_{-0.002}$	$0.902^{+0.008}_{-0.003}$	$0.021^{+0.001}_{-0.003}$	...	...	...	0.023	TD
113	118.2	0717	3488	$1.320^{+0.002}_{-0.008}$	$1.207^{+0.003}_{-0.002}$	$0.113^{+0.001}_{-0.002}$	$0.914^{+0.008}_{-0.003}$	$0.014^{+0.001}_{-0.003}$	...	...	...	0.024	TD
114	121.6	0720	2144	$1.305^{+0.001}_{-0.009}$	$1.246^{+0.003}_{-0.003}$	$0.059^{+0.001}_{-0.002}$	$0.955^{+0.009}_{-0.003}$	$0.058^{+0.003}_{-0.012}$	...	...	...	0.027	TD
115	124.5	0723	3184	$1.265^{+0.002}_{-0.005}$	$1.196^{+0.003}_{-0.003}$	$0.069^{+0.001}_{-0.001}$	$0.945^{+0.006}_{-0.004}$	$0.156^{+0.006}_{-0.022}$	...	...	...	0.026	TD
116	127.2	0726	4912	$1.249^{+0.001}_{-0.008}$	$1.172^{+0.003}_{-0.003}$	$0.078^{+0.001}_{-0.002}$	$0.938^{+0.008}_{-0.003}$	$0.033^{+0.002}_{-0.005}$	...	...	...	0.024	TD
117	130.9	0729	4688	$1.192^{+0.001}_{-0.007}$	$1.103^{+0.002}_{-0.003}$	$0.089^{+0.001}_{-0.002}$	$0.925^{+0.007}_{-0.003}$	$0.019^{+0.001}_{-0.004}$	...	...	...	0.022	TD
118	131.9	0730	2080	$1.215^{+0.001}_{-0.008}$	$1.085^{+0.003}_{-0.002}$	$0.130^{+0.002}_{-0.002}$	$0.893^{+0.008}_{-0.002}$	$0.018^{+0.001}_{-0.004}$	...	...	...	0.026	TD
119	134.0	0801	1760	$1.187^{+0.001}_{-0.008}$	$1.126^{+0.003}_{-0.002}$	$0.061^{+0.001}_{-0.002}$	$0.949^{+0.009}_{-0.002}$	$0.041^{+0.003}_{-0.012}$	...	...	...	0.027	TD
120	136.5	0804	3696	$1.164^{+0.001}_{-0.009}$	$1.061^{+0.003}_{-0.002}$	$0.102^{+0.001}_{-0.002}$	$0.912^{+0.010}_{-0.002}$	$0.016^{+0.001}_{-0.013}$	...	...	...	0.022	TD
121	143.4	0811	1744	$1.073^{+0.002}_{-0.010}$	$1.015^{+0.002}_{-0.003}$	$0.059^{+0.001}_{-0.002}$	$0.946^{+0.011}_{-0.005}$	$0.041^{+0.002}_{-0.009}$	...	...	...	0.029	TD
122	146.4	0814	1952	$1.030^{+0.001}_{-0.007}$	$0.925^{+0.002}_{-0.002}$	$0.105^{+0.002}_{-0.002}$	$0.898^{+0.008}_{-0.003}$	$0.019^{+0.001}_{-0.003}$	...	...	...	0.031	TD
123	150.4	0818	1456	$0.982^{+0.001}_{-0.009}$	$0.892^{+0.002}_{-0.002}$	$0.090^{+0.001}_{-0.002}$	$0.908^{+0.010}_{-0.003}$	$0.029^{+0.001}_{-0.006}$	...	...	...	0.032	TD
124	156.1	0824	1648	$0.934^{+0.001}_{-0.009}$	$0.869^{+0.001}_{-0.002}$	$0.064^{+0.001}_{-0.002}$	$0.930^{+0.010}_{-0.003}$	$0.030^{+0.002}_{-0.008}$	...	...	...	0.028	TD
125	158.7	0826	672	$0.930^{+0.001}_{-0.010}$	$0.829^{+0.002}_{-0.003}$	$0.101^{+0.001}_{-0.002}$	$0.891^{+0.012}_{-0.004}$	$0.017^{+0.003}_{-0.018}$	...	...	...	0.028	TD
126	164.3	0901	3024	$0.847^{+0.001}_{-0.007}$	$0.773^{+0.002}_{-0.002}$	$0.074^{+0.001}_{-0.001}$	$0.913^{+0.010}_{-0.003}$	$0.028^{+0.002}_{-0.007}$	...	...	...	0.029	TD
127	167.6	0904	1920	$0.865^{+0.001}_{-0.008}$	$0.715^{+0.001}_{-0.002}$	$0.150^{+0.002}_{-0.001}$	$0.827^{+0.009}_{-0.003}$	$0.008^{+0.001}_{-0.001}$	...	...	...	0.030	TD[y]
128	169.9	0906	2304	$0.829^{+0.001}_{-0.006}$	$0.754^{+0.002}_{-0.002}$	$0.075^{+0.001}_{-0.001}$	$0.910^{+0.009}_{-0.004}$	$0.035^{+0.002}_{-0.006}$	...	...	...	0.023	TD
129	172.4	0909	2800	$0.828^{+0.001}_{-0.004}$	$0.759^{+0.001}_{-0.002}$	$0.069^{+0.001}_{-0.001}$	$0.917^{+0.006}_{-0.004}$	$0.231^{+0.017}_{-0.022}$	...	...	...	0.025	TD
130	175.1	0912	1072	$0.806^{+0.001}_{-0.005}$	$0.745^{+0.002}_{-0.002}$	$0.061^{+0.001}_{-0.001}$	$0.924^{+0.008}_{-0.004}$	$0.271^{+0.023}_{-0.028}$	...	...	...	0.028	TD
131	179.7	0916	960	$0.712^{+0.001}_{-0.005}$	$0.648^{+0.002}_{-0.002}$	$0.064^{+0.001}_{-0.001}$	$0.910^{+0.009}_{-0.004}$	$0.171^{+0.016}_{-0.013}$	...	...	...	0.032	TD
132	181.9	0918	928	$0.717^{+0.001}_{-0.008}$	$0.655^{+0.002}_{-0.002}$	$0.062^{+0.001}_{-0.001}$	$0.914^{+0.013}_{-0.004}$	$0.042^{+0.005}_{-0.013}$	...	...	...	0.033	TD
133	185.0	0921	752	$0.676^{+0.001}_{-0.009}$	$0.601^{+0.001}_{-0.002}$	$0.074^{+0.001}_{-0.001}$	$0.889^{+0.013}_{-0.004}$	$0.052^{+0.005}_{-0.013}$	...	...	...	0.033	TD
134	187.0	0923	512	$0.655^{+0.001}_{-0.005}$	$0.602^{+0.001}_{-0.002}$	$0.054^{+0.001}_{-0.001}$	$0.919^{+0.009}_{-0.004}$	$0.180^{+0.019}_{-0.038}$	...	...	...	0.036	TD
135	187.1	0924	2240	$0.636^{+0.001}_{-0.003}$	$0.578^{+0.002}_{-0.001}$	$0.059^{+0.001}_{-0.001}$	$0.909^{+0.007}_{-0.003}$	$0.151^{+0.010}_{-0.013}$	...	...	...	0.030	TD
136	189.5	0926	2352	$0.613^{+0.001}_{-0.003}$	$0.564^{+0.002}_{-0.001}$	$0.049^{+0.002}_{-0.001}$	$0.920^{+0.008}_{-0.003}$	$0.184^{+0.013}_{-0.044}$	...	...	...	0.024	TD
137	190.6	0927	2928	$0.606^{+0.001}_{-0.003}$	$0.553^{+0.001}_{-0.001}$	$0.053^{+0.001}_{-0.001}$	$0.913^{+0.006}_{-0.003}$	$0.312^{+0.013}_{-0.019}$	...	...	...	0.028	TD
138	192.5	0929	3456	$0.617^{+0.001}_{-0.002}$	$0.535^{+0.001}_{-0.002}$	$0.082^{+0.001}_{-0.001}$	$0.867^{+0.004}_{-0.005}$	$0.441^{+0.020}_{-0.012}$	...	...	...	0.026	TD
139	193.5	0930	3408	$0.621^{+0.001}_{-0.003}$	$0.518^{+0.001}_{-0.002}$	$0.103^{+0.001}_{-0.001}$	$0.834^{+0.006}_{-0.005}$	$0.605^{+0.011}_{-0.025}$	...	...	...	0.022	TD
140	195.5	1002	2352	$0.522^{+0.001}_{-0.003}$	$0.472^{+0.001}_{-0.001}$	$0.050^{+0.001}_{-0.001}$	$0.904^{+0.007}_{-0.004}$	$0.268^{+0.016}_{-0.007}$	...	...	...	0.025	TD
141	197.4	1004	3328	$0.491^{+0.001}_{-0.002}$	$0.418^{+0.001}_{-0.001}$	$0.074^{+0.001}_{-0.001}$	$0.851^{+0.006}_{-0.004}$	$0.424^{+0.017}_{-0.017}$	...	...	...	0.026	TD
142	198.6	1005	3360	$0.474^{+0.001}_{-0.002}$	$0.405^{+0.001}_{-0.001}$	$0.069^{+0.001}_{-0.001}$	$0.854^{+0.006}_{-0.004}$	$0.391^{+0.020}_{-0.013}$	...	...	...	0.031	TD
143	201.1	1008	2448	$0.392^{+0.001}_{-0.002}$	$0.358^{+0.001}_{-0.001}$	$0.033^{+0.001}_{-0.001}$	$0.913^{+0.007}_{-0.005}$	$0.187^{+0.013}_{-0.018}$	...	...	...	0.031	TD
144	202.5	1009	2192	$0.366^{+0.001}_{-0.002}$	$0.321^{+0.001}_{-0.001}$	$0.045^{+0.001}_{-0.001}$	$0.877^{+0.008}_{-0.005}$	$0.164^{+0.016}_{-0.009}$	...	...	...	0.035	TD
145	205.2	1012	2624	$0.319^{+0.001}_{-0.002}$	$0.281^{+0.001}_{-0.001}$	$0.037^{+0.001}_{-0.001}$	$0.881^{+0.009}_{-0.006}$	$0.183^{+0.012}_{-0.013}$	...	...	...	0.037	TD
146	207.2	1014	3392	$0.283^{+0.001}_{-0.001}$	$0.237^{+0.001}_{-0.001}$	$0.046^{+0.001}_{-0.001}$	$0.837^{+0.007}_{-0.006}$	$0.206^{+0.014}_{-0.007}$	...	...	...	0.028	TD
147	208.1	1015	3328	$0.265^{+0.001}_{-0.001}$	$0.222^{+0.001}_{-0.001}$	$0.043^{+0.001}_{-0.001}$	$0.838^{+0.007}_{-0.007}$	$0.156^{+0.014}_{-0.007}$	...	...	...	0.033	TD
148	209.5	1016	1792	$0.249^{+0.001}_{-0.002}$	$0.201^{+0.001}_{-0.001}$	$0.048^{+0.001}_{-0.001}$	$0.807^{+0.011}_{-0.007}$	$0.183^{+0.016}_{-0.011}$	...	...	...	0.045	TD

Table A2
(Continued)

Obs. No.	Day[b]	UT 2003 (mmdd)	Obs. Time (s)	Total 2–20 keV (10^{-8} cgs)	Disk 2–20 keV (10^{-8} cgs)	Power Law 2–20 keV (10^{-8} cgs)	2–20 keV Disk/Total	Power Law 20–100 keV (10^{-9} cgs)	QPO ν[c] (Hz)	QPO Amplitude[d] (% rms)	QPO Q[e]	Cont. r[f] (rms)	State[g]
149	210.4	1017	3392	$0.236^{+0.001}_{-0.001}$	$0.188^{+0.001}_{-0.001}$	$0.049^{+0.001}_{-0.001}$	$0.797^{+0.008}_{-0.008}$	$0.258^{+0.015}_{-0.009}$	...	...	...	0.038	TD
150	211.0	1017	3456	$0.231^{+0.001}_{-0.001}$	$0.178^{+0.001}_{-0.001}$	$0.053^{+0.001}_{-0.001}$	$0.771^{+0.008}_{-0.008}$	$0.295^{+0.013}_{-0.011}$	...	...	...	0.037	TD
151	212.0	1018	3424	$0.250^{+0.001}_{-0.001}$	$0.156^{+0.001}_{-0.001}$	$0.094^{+0.001}_{-0.001}$	$0.624^{+0.007}_{-0.006}$	$0.427^{+0.018}_{-0.014}$	...	...	...	0.070	H:SPL
152	213.1	1020	3248	$0.233^{+0.001}_{-0.001}$	$0.112^{+0.001}_{-0.001}$	$0.121^{+0.001}_{-0.001}$	$0.481^{+0.006}_{-0.006}$	$0.629^{+0.022}_{-0.014}$	7.87	3.55 ± 0.21	11.92 ± 1.63	0.082	H:SPL
153	214.3	1021	3376	$0.189^{+0.001}_{-0.001}$	$0.132^{+0.001}_{-0.001}$	$0.057^{+0.001}_{-0.001}$	$0.698^{+0.009}_{-0.009}$	$0.304^{+0.013}_{-0.013}$	...	...	...	0.050	H:SPL
154	215.0	1022	3376	$0.205^{+0.001}_{-0.001}$	$0.106^{+0.001}_{-0.001}$	$0.099^{+0.001}_{-0.001}$	$0.517^{+0.007}_{-0.007}$	$0.483^{+0.017}_{-0.010}$	7.65	4.05 ± 0.35	4.73 ± 0.88	0.078	H:SPL
155	216.1	1023	2816	$0.176^{+0.001}_{-0.001}$	$0.102^{+0.001}_{-0.001}$	$0.074^{+0.001}_{-0.001}$	$0.580^{+0.009}_{-0.009}$	$0.323^{+0.015}_{-0.015}$	5.97	3.42 ± 0.46	6.86 ± 2.06	0.073	H:SPL
156	217.0	1024	2224	$0.170^{+0.001}_{-0.001}$	$0.078^{+0.001}_{-0.001}$	$0.092^{+0.001}_{-0.001}$	$0.459^{+0.009}_{-0.009}$	$0.416^{+0.016}_{-0.015}$	8.03	3.55 ± 0.46	8.16 ± 2.17	0.084	H:SPL
157	218.0	1025	3392	$0.159^{+0.001}_{-0.001}$	$0.054^{+0.001}_{-0.001}$	$0.105^{+0.001}_{-0.001}$	$0.340^{+0.008}_{-0.008}$	$0.600^{+0.018}_{-0.013}$	7.01	5.14 ± 0.22	10.16 ± 1.03	0.111	H:SPL
158	219.0	1026	2048	$0.147^{+0.001}_{-0.001}$	$0.034^{+0.001}_{-0.001}$	$0.113^{+0.001}_{-0.001}$	$0.231^{+0.008}_{-0.008}$	$0.622^{+0.018}_{-0.025}$	5.91	7.59 ± 0.35	4.35 ± 0.48	0.138	H:SPL
159	220.1	1027	1984	$0.140^{+0.001}_{-0.001}$	$0.024^{+0.001}_{-0.001}$	$0.116^{+0.001}_{-0.001}$	$0.171^{+0.008}_{-0.008}$	$0.475^{+0.016}_{-0.023}$	5.85	7.18 ± 0.31	6.03 ± 0.62	0.132	H:SPL
160	223.2	1030	1936	$0.089^{+0.001}_{-0.001}$	$0.010^{+0.001}_{-0.001}$	$0.079^{+0.001}_{-0.001}$	$0.112^{+0.013}_{-0.012}$	$0.601^{+0.013}_{-0.025}$	3.07	8.26 ± 0.41	2.82 ± 0.34	0.170	H
161	223.7	1030	1552	$0.081^{+0.001}_{-0.002}$	$0.010^{+0.001}_{-0.001}$	$0.071^{+0.001}_{-0.001}$	$0.123^{+0.016}_{-0.014}$	$0.059^{+0.009}_{-0.026}$	2.81	6.91 ± 0.49	6.24 ± 1.12	0.177	H
162	225.2	1101	9872	$0.069^{+0.001}_{-0.001}$	$0.006^{+0.001}_{-0.001}$	$0.063^{+0.001}_{-0.001}$	$0.087^{+0.016}_{-0.016}$	$0.505^{+0.006}_{-0.008}$	2.48	7.58 ± 0.30	2.85 ± 0.27	0.172	H
163	226.2	1102	1664	$0.055^{+0.001}_{-0.001}$	$0.009^{+0.001}_{-0.001}$	$0.047^{+0.001}_{-0.001}$	$0.164^{+0.022}_{-0.021}$	$0.517^{+0.023}_{-0.024}$	...	...	...	0.165	H
164	227.2	1103	10342	$0.049^{+0.001}_{-0.001}$	...	$0.049^{+0.001}_{-0.001}$	...	$0.348^{+0.003}_{-0.006}$	...	...	...	0.155	H
165	228.1	1104	1040	$0.045^{+0.001}_{-0.001}$	...	$0.045^{+0.001}_{-0.001}$	...	$0.321^{+0.019}_{-0.021}$	...	...	...	0.151	H
166	229.2	1105	5072	$0.039^{+0.001}_{-0.001}$	...	$0.039^{+0.001}_{-0.001}$	...	$0.263^{+0.013}_{-0.016}$	...	...	...	0.139	H
167	230.2	1106	13696	$0.035^{+0.001}_{-0.001}$	...	$0.035^{+0.001}_{-0.001}$	...	$0.230^{+0.003}_{-0.004}$	...	...	...	0.129	H
168	231.5	1107	2816	$0.022^{+0.001}_{-0.001}$	...	$0.022^{+0.001}_{-0.001}$	...	$0.133^{+0.019}_{-0.020}$	...	...	...	0.131	H
169	232.4	1108	4128	$0.027^{+0.001}_{-0.001}$	...	$0.027^{+0.001}_{-0.001}$	...	$0.147^{+0.017}_{-0.015}$	...	...	...	0.140	H:SPL
170	233.3	1109	2016	$0.023^{+0.001}_{-0.001}$	...	$0.023^{+0.001}_{-0.001}$	...	$0.121^{+0.005}_{-0.006}$	...	...	...	0.155	H:SPL

Notes.

[a] Fluxes are in units of erg cm^{-2} s^{-1}.

[b] Number of days since discovery on 2003 March 21 = MJD 52719 (Revnivtsev et al. 2003).

[c] Centroid frequency of the primary QPO peak. The uncertainty (1σ) is $\lesssim$1% for observations 1–85, and 2% thereafter. Exceptions are observations 1 (3%), 12 (2%), 22 (2%), 68 (8%), 70 (3%), 72 (2%), 74 (2%), 75 (2%), 80 (3%), 154 (3%), and 160 (3%).

[d] The QPO amplitude is the fractional rms fluctuation, calculated as the square root of the integrated power in the QPO feature and expressed as a fraction of the mean count rate. Errors are 1σ, with a lower limit of 0.1% for systematic uncertainty in the continuum model, except for especially narrow QPOs ($Q > 10$).

[e] Q = (QPO frequency)/FWHM.

[f] Total rms power (r) integrated over 0.1–10 Hz in the PDS (2–30 keV). The uncertainty (1σ) is 1% (observations 1–85), 2% (86–93), 4% (94–102), 6% (103–118), 10% (119–150), 5% (151–168), and 10 % (169–170).

[g] See Table 1 and Section 2.4 for definitions of states. We note that some Galactic ridge emission in the PCA field of view or inaccuracies in the PCA background model may affect the state classifications for the faintest observations considered in this study.

[h] Harmonic present at 2ν.

[i] Fitted using data from HEXTE Cluster B because data from Cluster A saturated the telemetry.

[j] Pair of harmonics present at 0.5ν and 2ν.

[k] HEXTE fitting range restricted to $E = 32$–200 keV (includes HEXTE-A channels 17–56).

[l] Weak harmonic present at 2ν.

[m] Additional weak QPO at 3.9 Hz.

[n] Broad harmonic possibly present at 0.5ν.

[o] Additional QPO at 4.54 Hz.

[p] Additional narrow QPO at 5.14 Hz.

[q] Additional weak QPO at 4.3 Hz.

[r] Weak and broad harmonic at frequency 2ν.

[s] Additional QPO at 9.0 Hz.

[t] Weak and broad harmonic possibly present at 2ν.

[u] Additional QPO at 4.6 Hz.

[v] Strong harmonic present at 2ν.

[w] Harmonic present at 0.5ν.

[x] PCA background appears to be overestimated in standard processing (see footnote "k" in Table A2).

observations. The tables jointly also relate the Day Number (used in Figures 1–5 and Figures 13 and 14) to the UT date and MJD, and they assign an index number to each observation. For each observation, Table A1 also provides the following additional information that is not presented in the figures: the break energy $E_{\rm break}$, the central energy and FWHM of the Fe line,

Table A3
VLA Radio Flux Densities for H1743−322: $\nu \leqslant 8.640$ GHz

UT 2003 (mmdd)	MJD[a]	Day[b]	VLA[c]	1.425 GHz S_ν(mJy)	MJD	Day	4.860 GHz S_ν(mJy)	MJD	Day	8.460 GHz S_ν(mJy)
0330	···	···	D	···	52728.6016	9.6	3.39 ± 0.15	52728.5938	9.6	4.57 ± 0.12
0401	52730.5586	11.6	D	8.19 ± 1.53	52730.5547	11.6	5.78 ± 0.18	52730.5469	11.6	6.45 ± 0.12
0403	···	···	D	···	52732.5195	13.5	15.31 ± 0.20	52732.5469	13.6	16.99 ± 0.12
0404	···	···	D	···	52733.5195	14.5	20.08 ± 0.24	52733.5156	14.5	18.68 ± 0.31
0404	···	···	D	···	···	···	···	52733.5469	14.6	21.81 ± 0.13
0406	···	···	D	···	52735.4062	16.4	20.27 ± 0.26	52735.4219	16.4	19.62 ± 0.16
0406	···	···	D	···	52735.4375	16.4	20.47 ± 0.18	52735.4414	16.4	19.58 ± 0.13
0406	···	···	D	···	52735.4688	16.5	20.23 ± 0.22	52735.4648	16.5	19.43 ± 0.16
0408	···	···	D	···	52737.4844	18.5	96.07 ± 0.20	52737.4961	18.5	68.04 ± 0.16
0409	52738.4453	19.4	D	27.03 ± 1.54	52738.4570	19.5	23.10 ± 0.17	52738.4609	19.5	20.29 ± 0.08
0410	52739.4609	20.5	D	14.94 ± 1.53	52739.4766	20.5	21.37 ± 0.18	52739.4570	20.5	21.10 ± 0.13
0410	···	···	D	···	···	···	···	52739.4961	20.5	20.65 ± 0.08
0410	···	···	D	···	···	···	···	52739.5391	20.5	20.28 ± 0.11
0411	52740.5508	21.6	D	63.34 ± 1.74	52740.5547	21.6	24.95 ± 0.20	52740.5469	21.6	16.07 ± 0.12
0412	52741.5430	22.5	D	32.86 ± 1.49	52741.5625	22.6	12.78 ± 0.21	52741.5625	22.6	7.71 ± 0.12
0413	52742.4961	23.5	D	8.10 ± 1.23	52742.5195	23.5	4.40 ± 0.22	52742.5195	23.5	3.87 ± 0.13
0416	···	···	D	···	52745.4375	26.4	41.44 ± 0.24	52745.4336	26.4	37.15 ± 0.13
0420	···	···	D	···	52749.6055	30.6	16.48 ± 0.38	52749.5977	30.6	12.46 ± 0.20
0421	···	···	D	···	52750.5977	31.6	23.10 ± 0.51	52750.5977	31.6	20.94 ± 0.31
0423	···	···	D	···	52752.5352	33.5	12.20 ± 0.26	52752.5352	33.5	11.48 ± 0.20
0426	52755.5352	36.5	D	9.73 ± 1.21	52755.5312	36.5	7.54 ± 0.17	52755.4961	36.5	5.58 ± 0.12
0429	52758.4062	39.4	D	7.48 ± 1.27	52758.4219	39.4	8.45 ± 0.16	52758.4141	39.4	6.64 ± 0.10
0506	···	···	D	···	52765.4375	46.4	13.78 ± 0.21	52765.4219	46.4	11.12 ± 0.13
0508	···	···	D	···	52767.5195	48.5	25.62 ± 0.19	52767.5195	48.5	23.02 ± 0.12
0509	···	···	D	···	52768.5039	49.5	34.59 ± 0.24	52768.4922	49.5	30.14 ± 0.16
0510	···	···	D	···	52769.5156	50.5	28.04 ± 0.19	52769.5078	50.5	23.80 ± 0.14
0514	···	···	A	···	···	···	···	52773.3633	54.4	35.76 ± 0.23
0520	···	···	A	···	52779.4141	60.4	14.15 ± 0.31	52779.4414	60.4	11.77 ± 0.16
0520	···	···	A	···	52779.4141	60.4	14.01 ± 0.37	52779.4414	60.4	12.21 ± 0.30
0527	···	···	A	···	52786.3477	67.3	21.49 ± 0.12	52786.0000	67.0	15.57 ± 0.30
0527	···	···	A	···	···	···	···	52786.0000	67.0	15.87 ± 0.32
0527	···	···	A	···	52786.3477	67.3	22.49 ± 0.41	52786.3555	67.4	15.81 ± 0.27
0527	···	···	A	···	···	···	···	52786.3555	67.4	16.06 ± 0.12
0527	···	···	A	···	···	···	···	52786.4844	67.5	16.90 ± 0.38
0527	···	···	A	···	···	···	···	52786.4844	67.5	16.15 ± 0.16
0529	···	···	A	···	···	···	···	52788.3750	69.4	5.59 ± 0.05
0604	···	···	A	···	···	···	···	52794.4023	75.4	4.34 ± 0.04
0609	···	···	A	···	···	···	···	52799.2539	80.3	0.81 ± 0.06
0610	52800.2344	81.2	A	1.43 ± 0.12	52800.2383	81.2	0.94 ± 0.09	52800.2539	81.3	0.42 ± 0.04
0611	···	···	A	···	···	···	···	52801.2969	82.3	0.34 ± 0.04
0619	52809.2070	90.2	A	2.37 ± 0.13	52809.2148	90.2	1.72 ± 0.09	52809.2227	90.2	1.42 ± 0.06
0627	···	···	A	···	···	···	···	52817.2383	98.2	2.29 ± 0.09
0628	···	···	A	···	···	···	···	52818.2383	99.2	3.16 ± 0.07
0709	···	···	A	···	52829.3477	110.3	1.28 ± 0.12	52829.3398	110.3	0.45 ± 0.05
0713	52833.2148	114.2	A	1.17 ± 0.14	52833.2188	114.2	0.46 ± 0.10	52833.2148	114.2	0.28 ± 0.06
0716	52836.3320	117.3	A	0.97 ± 0.17	···	···	···	52836.3359	117.3	< 0.18sup*d*
0722	···	···	A	···	52842.2930	123.3	< 0.65[d]	52842.2930	123.3	< 0.22[d]
0728	52848.2422	129.2	A	< 0.55	···	···	···	···	···	···
0729	52849.1953	130.2	A	< 0.66	···	···	···	···	···	···
0731	52851.3203	132.3	A	< 0.84	···	···	···	···	···	···
0803	52852.3203	133.3	A	< 0.71	···	···	···	···	···	···
0806	52857.1055	138.1	A	< 0.37	···	···	···	···	···	···
0812	52863.0508	144.1	A	< 0.61	···	···	···	52863.0742	144.1	< 0.03[d]
0817	52868.1250	149.1	A	< 0.37	···	···	···	52868.1406	149.1	< 0.30[d]
0819	52870.0742	151.1	A	< 0.21	···	···	···	52870.0938	151.1	< 0.12[d]
0819	···	···	A	···	···	···	···	···	···	···
0822	52873.1211	154.1	A	< 0.40	···	···	···	···	···	···
0825	52877.0000	158.0	A	< 0.99	52877.0195	158.0	< 0.34[d]	···	···	···
0903	···	···	A	···	52885.1133	166.1	< 0.13[d]	···	···	···
0906	52888.1367	169.1	A	< 0.68	52888.1250	169.1	< 0.31[d]	52888.1133	169.1	< 0.22*d*
0913	···	···	BnA	···	52895.1562	176.2	< 0.35[d]	···	···	···

Table A3
(Continued)

UT 2003 (mmdd)	MJD[a]	Day[b]	VLA[c]	1.425 GHz S_ν(mJy)	MJD	Day	4.860 GHz S_ν(mJy)	MJD	Day	8.460 GHz S_ν(mJy)
0914	...	...	BnA	...	52896.1367	177.1	< 0.30[d]	...	...	...
0916	52898.1719	179.2	BnA	< 0.48	52898.1602	179.2	< 0.22[d]	...	...	...
0920	...	...	BnA	...	52903.0312	184.0	< 0.18[d]	...	...	...
0925	...	...	BnA	...	52907.1680	188.2	< 0.37[d]	...	...	...
0927	...	...	BnA	...	52909.1250	190.1	< 0.34[d]	52909.1055	190.1	< 0.24[d]
1002	...	...	BnA	...	52915.0234	196.0	< 0.18[d]	52915.0078	196.0	< 0.23[d]
1012	...	...	B	...	52924.9336	205.9	< 0.30[d]	52924.9180	205.9	< 0.31[d]
1020	...	...	B	...	52932.9727	214.0	< 0.36[d]	52932.9609	214.0	< 0.10[d]
1027	...	...	B	...	52940.0195	221.0	0.21 ± 0.06	52939.9961	221.0	0.14 ± 0.04
1029	...	...	B	...	52941.9570	223.0	< 0.38[d]	52941.9453	222.9	< 0.38[d]
1104	52948.0391	229.0	B	< 1.08	52948.0234	229.0	0.14 ± 0.06	52948.0039	229.0	0.22 ± 0.05
1106	...	...	B	...	52949.9531	231.0	0.18 ± 0.04	52949.9414	230.9	< 0.42[d]

Notes.
[a] Modified Julian Day = JD−2,400,000.5.
[b] Number of days since discovery on 2003 March 21 = MJD 52719 (Revnivtsev et al. 2003).
[c] Configuration of the VLA antennas.
[d] Upper limits correspond to the flux density measured at the nominal position of the center of the beam plus three times the rms noise.

Table A4
VLA Radio Flux Densities for H1743−322: $\nu \geqslant 14.940$ GHz

UT 2003 (mmdd)	MJD[a]	Day[b]	14.940 GHz S_ν(mJy)	MJD	Day	22.460 GHz S_ν(mJy)	MJD	Day	43.340 GHz S_ν(mJy)
0401	52730.5430	11.5	6.81 ± 0.51	...	...	...	...	...	...
0403	52732.5391	13.5	19.20 ± 0.33	52732.5352	13.5	21.32 ± 0.23	52732.5234	13.5	21.54 ± 0.87
0404	52733.5430	14.5	26.57 ± 0.40	52733.5391	14.5	26.36 ± 0.26	52733.5273	14.5	27.55 ± 1.01
0406	52735.4570	16.5	20.15 ± 0.45	52735.4531	16.5	22.69 ± 0.46	52735.4453	16.4	16.46 ± 1.26
0408	52737.5000	18.5	42.62 ± 0.44	52737.5078	18.5	51.01 ± 0.25	52737.4961	18.5	41.11 ± 0.73
0408	52737.5156	18.5	55.21 ± 0.32	...	...	...	...	...	...
0409	52738.4805	19.5	19.58 ± 0.31	52738.4766	19.5	21.13 ± 0.17	52738.4766	19.5	19.29 ± 0.46
0404	...	...	...	...	...	...	52738.4727	19.5	19.37 ± 0.62
0409	...	...	...	...	...	...	52738.4883	19.5	19.44 ± 0.64
0410	52739.5000	20.5	21.49 ± 0.32	52739.4922	20.5	24.03 ± 0.23	52739.4961	20.5	23.89 ± 0.51
0410	...	...	...	...	...	...	52739.4844	20.5	25.96 ± 0.74
0410	...	...	...	...	...	...	52739.5078	20.5	20.71 ± 0.70
0411	52740.5664	21.6	9.27 ± 0.43	52740.5625	21.5	6.53 ± 0.39	52740.5586	21.6	< 4.52[c]
0412	52741.5586	22.6	5.99 ± 0.43	52741.5547	22.6	4.62 ± 0.33	52741.5508	22.6	< 4.92[c]
0413	52742.5156	23.5	2.52 ± 0.36	52742.5078	23.5	2.47 ± 0.26	52742.5039	23.5	< 4.57[c]
0423	52752.5430	33.5	9.46 ± 0.60	...	...	...	...	...	...
0426	52755.5039	36.5	3.70 ± 0.28	...	...	...	...	...	...

Notes.
[a] Truncated Modified Julian Day = MJD 52000.
[b] Number of days since discovery on 2003 March 21 = MJD 52719 (Revnivtsev et al. 2003).
[c] Upper limits correspond to the flux density measured at the nominal position of the center of the beam plus three times the rms noise.

and the reduced χ^2 and number of degrees of freedom. Likewise, Table A2 contains two quantities that are not displayed in the figures: the exposure time for each observation and the ratio of the disk flux to the total flux (2–20 keV).

All of the radio flux density data plotted in Figures 13 and 14 versus Day Number are contained in Tables A3 and A4, respectively. These tables also give the correspondence between Day Number and the UT date and MJD. Table A5 gives 25 values of the radio spectral index that were determined during the first 115 days of the outburst cycle (see Figure 13(d)).

Note added in proof. For the first ∼5 weeks of pointed observations reported herein, i.e., through Observation Number 28 on Day 41.8, *RXTE* was pointed 0.°32 from H1743. Very recently, with the proofs nearly completed, we discovered this fact while preparing a second paper that makes use of these same data. Consequently, our results for these early observations have not been corrected to the full transmission of the PCA and HEXTE collimators (FWHM = 1°). Thus, the true fluxes and count rates for the first 28 of the 170 total observations is a factor of ∼1.47 larger than we report, which modestly affects a number of our results throughout the paper.

Table A5
Radio Spectral Index

UT 2003 (mmdd)	MJD[a]	Day[b]	Spectral Index α[c]
0330	52728.598	9.6	0.54 ± 0.09
0401	52730.551	11.6	0.20 ± 0.07
0404	52733.518	14.5	-0.13 ± 0.04
0406	52735.414	16.4	-0.06 ± 0.03
0406	52735.439	16.4	-0.08 ± 0.02
0406	52735.467	16.5	-0.07 ± 0.02
0408	52737.490	18.5	-0.62 ± 0.01
0409	52738.459	19.5	-0.23 ± 0.02
0411	52740.551	21.6	-0.79 ± 0.02
0412	52741.563	22.6	-0.91 ± 0.04
0413	52742.520	23.5	-0.23 ± 0.11
0416	52745.436	26.4	-0.20 ± 0.01
0420	52749.602	30.6	-0.50 ± 0.05
0421	52750.598	31.6	-0.18 ± 0.05
0423	52752.535	33.5	-0.11 ± 0.05
0429	52758.418	39.4	-0.43 ± 0.04
0506	52765.430	46.4	-0.39 ± 0.03
0508	52767.520	48.5	-0.19 ± 0.02
0509	52768.498	49.5	-0.25 ± 0.02
0510	52769.512	50.5	-0.30 ± 0.02
0527	52786.352	67.3	-0.64 ± 0.05
0610	52800.246	81.2	-1.45 ± 0.24
0619	52809.219	90.2	-0.35 ± 0.12
0709	52829.344	110.3	-1.89 ± 0.26
0713	52833.217	114.2	-0.90 ± 0.55

Notes.
[a] Modified Julian Day = JD−2,400,000.5.
[b] Number of days since discovery on 2003 March 21 = MJD 52719 (Revnivtsev et al. 2003).
[c] Radio spectral index α ($S_\nu \propto \nu^\alpha$), which is based on the 4.860 GHz and 8.460 GHz data.

REFERENCES

Abe, Y., Fukazawa, Y., Kubota, A., Kasama, D., & Makishima, K. 2005, PASJ, 57, 629
Abramowicz, M. A., & Kluzniak, W. 2001, A&A, 374, L19
Akaike, H. 1974, IEEE Trans. Autom. Control, 19, 716
Arnaud, K. A. 1996, in ASP Conf. Ser. 101, Astronomical Data Analysis Software and Systems V, ed. G. H. Jacoby & J. Barnes (San Francisco, CA: ASP), 17
Baba, D., Nagata, T., Iwata, I., Kato, T., & Yamaoka, H. 2003, IAU Circ. 8112, 2
Balucinska-Church, M., & McCammon, D. 1992, ApJ, 400, 699
Belloni, T., Homan, J., Casella, P., van der Klis, M., Nespoli, E., Lewin, W. H. G., Miller, J. M., & Méndez, M. 2005, A&A, 440, 207
Brenneman, L. W., & Reynolds, C. S. 2006, ApJ, 652, 1028
Capitanio, F., et al. 2005, ApJ, 622, 503
Capitanio, F., et al. 2006, ApJ, 643, 376
Cooke, B. A., Levine, A. M., Lang, F. L., Primini, F. A., & Lewin, W. H. G. 1984, ApJ, 285, 258
Corbel, S., Fender, R. P., Tzioumis, A. K., Tomsick, J. A., Orosz, J. A., Miller, J. M., Wijnands, R., & Kaaret, P. 2002, Science, 298, 196
Corbel, S., Kaaret, P., Fender, R. P., Tzioumis, A. K., Tomsick, J. A., & Orosz, J. A. 2005, ApJ, 632, 504
Davis, S. W., Blaes, O. M., Hubeny, I., & Turner, N. J. 2005, ApJ, 621, 372
Davis, S. W., Done, C., & Blaes, O. M. 2006, ApJ, 647, 525
Doxsey, R., et al. 1977, IAU Circ., 3113, 2
Ebisawa, K., et al. 1994, PASJ, 46, 375
Fender, R. P., Belloni, T. M., & Gallo, E. 2004, MNRAS, 355, 1105
Gierliński, M., & Done, C. 2004, MNRAS, 347, 885
Gou, L., Mc Clintock, J. E., Liu, J., Narayan, R., Steiner, J. F., Remillard, R. A., Orosz, J. A., & Davis, S. W. 2009, ApJ, submitted (arXiv:0901.0920v1)
Gursky, H., et al. 1978, ApJ, 223, 973
Hannikainen, D., Campbell-Wilson, D., Hunstead, R., McIntyre, V., Lovell, J., Reynolds, J., Tzioumis, T., & Wu, K. 2001, Ap&SSS, 276, 45
Homan, J., Miller, J. M., Wijnands, R., van der Klis, M., Belloni, T., Steeghs, D., & Lewin, W. H. G. 2005, ApJ, 623, 383
Jahoda, K., Markwardt, C. B., Radeva, Y., Rots, A. H., Stark, M. J., Swank, J. H., Strohmayer, T. E., & Zhang, W. 2006, ApJS, 163, 401
Joinet, A., Jourdain, E., Malzac, J., Roques, J. P., Schönfelder, V., Ubertini, P., & Capitanio, F. 2005, ApJ, 629, 1008
Kaaret, P., Corbel, S., Tomsick, J. A., Fender, R., Miller, J. M., Orosz, J. A., Tzioumis, A. K., & Wijnands, R. 2003, ApJ, 582, 945
Kalemci, E., Tomsick, J. A., Rothschild, R. E., Pottschmidt, K., Corbel, S., & Kaaret, P. 2006, ApJ, 639, 340
Kaluzienski, L. J., & Holt, S. S. 1977, IAU Circ., 3099, 3
Kubota, A., & Makishima, K. 2004, ApJ, 601, 428
Kubota, A., Makishima, K., & Ebisawa, K. 2001, ApJ, 560, L147
Liu, J., McClintock, J. E., Narayan, R., Davis, S. W., & Orosz, J. A. 2008, ApJ, 679, L37
Lutovinov, A., Revnivtsev, M., Molkov, S., & Sunyaev, R. 2005, A&A, 430, 997
Makishima, K., Maejima, Y., Mitsuda, K., Bradt, H. V., Remillard, R. A., Tuohy, I. R., Hoshi, R., & Nakagawa, M. 1986, ApJ, 308, 635
Markwardt, C. B., & Swank, J. H. 2003a, ATel, 133
Markwardt, C. B., & Swank, J. H. 2003b, ATel, 136
Markwardt, C. B., Swank, J. H., & Taam, R. E. 1999, ApJ, 513, L37
Martini, P., Persson, S. E., Murphy, D. C., Birk, C., Shectman, S. A., Gunnels, S. M., & Koch, E. 2004, Proc. SPIE, 5492, 1653
McClintock, J. E., Narayan, R., & Shafee, R. 2007, in Black Holes, ed. M. Livio & A. Koekemoer (Cambridge: Cambridge Univ. Press) in press (arXiv:0707.4492v1)
McClintock, J. E., & Remillard, R. A. 2006, in Compact Stellar X-ray Sources, ed. W. Lewin & M. van der Klis (Cambridge: Cambridge Univ. Press), 157
McClintock, J. E., Shafee, R., Narayan, R., Remillard, R. A., Davis, S. W., & Li, L.-X. 2006, ApJ, 652, 518
Miller, J. M., et al. 2006, ApJ, 646, 394
Miller, J. M., et al. 2008, ApJ, 679, 113
Mitsuda, K., et al. 1984, PASJ, 36, 741
Muno, M. P., Morgan, E. H., & Remillard, R. A. 1999, ApJ, 527, 321
Narayan, R., & McClintock, J. E. 2005, ApJ, 623, 1017
Orosz, J. A., et al. 2002, ApJ, 568, 2002
Orosz, J. A., et al. 2007, Nature, 449, 872
Park, S. Q., et al. 2004, ApJ, 610, 378
Parmar, A. N., Kuulkers, E., Oosterbroek, P., Barr, P., Much, R., Orr, A., Williams, O. R., & Winkler, C. 2003, A&A, 411, L421
Persson, S. E., Murphy, D. C., Krzeminski, W., Roth, M., & Rieke, M. J. 1998, AJ, 116, 2475
Predehl, P., & Schmitt, J. H. M. M. 1995, A&A, 293, 889
Reis, R. C., Fabian, A. C., Ross, R. R., Miniutti, G., Miller, J. M., & Reynolds, C. 2008, MNRAS, 387, 1489
Remillard, R. A., & McClintock, J. E. 2006, ARA&A, 44, 49, RM06
Remillard, R. A., McClintock, J. E., Orosz, J. A., & Levine, A. M. 2006, ApJ, 637, 1002
Remillard, R. A., Muno, M. P., McClintock, J. E., & Orosz, J. A. 2002a, ApJ, 580, 1030
Remillard, R. A., Sobczak, G. J., Muno, M. P., & McClintock, J. E. 2002b, ApJ, 564, 962
Revnivtsev, M., Chernyakova, M., Westergaard, N. J., Shoenfelder, V., Gehrels, N., & Winkler, C. 2003, ATel, 132
Revnivtsev, M. G., Trudolyubov, S. P., & Borozdin, K. N. 2000, MNRAS, 312, 151
Rothschild, R. E., et al. 1998, ApJ, 496, 538
Rupen, M. P., Mioduszewski, A. J., & Dhawan, V. 2003a, ATel, 137
Rupen, M. P., Mioduszewski, A. J., & Dhawan, V. 2003b, ATel, 139
Schlegel, D. J., Finkbeiner, D. P., & Davis, M. 1998, ApJ, 500, 525
Shafee, R., McClintock, J. E., Narayan, R., Davis, S. W., Li, L.-X., & Remillard, R. A. 2006, ApJ, 636, L113
Shakura, N. I., & Sunyaev, R. A. 1973, A&A, 24, 337
Shimura, T., & Takahara, F. 1995, ApJ, 445, 780
Silverman, J. M., & Filippenko, A. V. 2008, ApJ, 678, L17
Skrutskie, et al. 2006, AJ, 131, 1163
Sobczak, G. J., McClintock, J. E., Remillard, R. A., & Bailyn, C. D. 1999, ApJ, 520, 776
Sobczak, G. J., McClintock, J. E., Remillard, R. A., Cui, W., Levine, A. M., & Morgan, E. H. 2000a, ApJ, 531, 537
Sobczak, G. J., McClintock, J. E., Remillard, R. A., Cui, W., Levine, A. M., Morgan, E. H., Orosz, J. A., & Bailyn, C. D. 2000b, ApJ, 544, 993
Steeghs, D., Miller, J. M., Kaplan, D., & Rupen, M. 2003a, ATel, 141
Steeghs, D., Miller, J. M., Kaplan, D., & Rupen, M. 2003b, ATel, 146

Stetson, P. B. 1987, PASP, 99, 191
Tanaka, Y., & Lewin, W. H. G. 1995, in X-ray Binaries, ed. W. Lewin, J. van Paradijs, & E. van den Heuvel (Cambridge: Cambridge Univ. Press), 126
Titarchuk, L., & Fiorito, R. 2004, ApJ, 612, 988
Titarchuk, L., & Shaposhnikov, N. 2005, ApJ, 626, 298
Tomsick, J. A., Corbel, S., Fender, R., Miller, J. M., Orosz, J. A., Tzioumis, T., Wijnands, R., & Kaaret, P. 2003, ApJ, 582, 933
Tomsick, J. A., Corbel, S., Goldwurm, A., & Kaaret, P. 2005, ApJ, 630, 413
van Paradijs, J., & McClintock, J. E. 1994, A&A, 290, 133
Vignarca, F., Migliari, S., Belloni, T., Psaltis, D., & van der Klis, M. 2003, A&A, 397, 729
Wagoner, R. V. 1999, Phys. Rep., 311, 259
White, N. E., & Marshall, F. E. 1984, ApJ, 281, 354
Wilms, J., Nowak, M. A., Pottschmidt, K., Pooley, G. G., & Fritz, S. 2006, A&A, 447, 245
Yan, M., Sadeghpour, H. R., & Dalgarno, A. 1998, ApJ, 496, 1044